BILINGUAL
PUBLISHING CO.
Pioneer of Global Academics Since 1984

Journal of Atmospheric Science Research

Volume 4 • Issue 3 • July 2021 ISSN 2630-5119(Online)

BILINGUAL
PUBLISHING CO.
Pioneer of Global Academics Since 1984

Editor-in-Chief

Dr. José Francisco Oliveira Júnior

Initiative for Climate Action Transparency/Universidade Federal de Alagoas, Brazil

Editorial Board Members

Lei Zhong, China
Xiaodong Tang, China
Qiang Zhang, China
Chenghai Wang, China
Amr Ahmed Thabet, Egypt
Shek Md. Atiqure Rahman, Bangladesh
Svetlana Vasilivna Budnik, Ukraine
Xun Liu, China
Rengui Jiang, China
Fan Ping, China
Lucille Joanna Borlaza, Philippines
Xuezhi Tan, China
Hirdan Katarina de Medeiros Costa, Brazil
Chuanfeng Zhao, China
Suleiman Alsweiss, United States
Aditi Singh, India
Boris Denisovich Belan, Russian Federation
Perihan Kurt-Karakus, Turkey
Hongqian Chu, China
Isidro A. Pérez, Spain
Mahboubeh Molavi-Arabshahi, Iran
Tolga Elbir, Turkey
Junyan Zhang, United States
Thi Hien To, Vietnam
Jian Peng, United Kingdom
Zhen Li, United Kingdom
Anjani Kumar, India
Bedir Bedir Yousif, Egypt
Hassan Hashemi, Iran
Mengqian Lu, Hong Kong
Lichuan Wu, Sweden
Raj Kamal Singh, United States
Zhiyong Ding, China
Elijah Olusayo Olurotimi, South Africa
Naveen Shahi, South Africa
Netrananda Sahu, India
Luca Aluigi, Italy
Daniel Andrade Schuch, Brazil
Vladislav Vladimirovich Demyanov, Russian Federation
Kazi Sabiruddin, India
Nicolay Nikolayevich Zavalishin, Russian Federation
Alexander Ruzmaikin, United States
Peng Si, China
Zhaowu Yu, Denmark
Manish Kumar Joshi, United Kingdom
Aisulu Tursunova, Kazakhstan
Enio Bueno Pereira, Brazil
Samia Tabassum, Bangladesh
Donglian Sun, United States
Zhengqiang Li, China
Haider Abbas Khwaja, United States
Haikun Zhao, China
Wen Zhou, Hong Kong
Suman Paul, India
Anning Huang, China
ShenMing Fu, China
David Onojiede Edokpa, Nigeria
Haibo Hu, China
Era Upadhyay, India
Sergey Oktyabrinovich Gladkov, Russian Federation
Ghani Rahman, Pakistan
El-Sayed Mohamed Abdel-Hamid Robaa, Egypt
Andac Akdemir, Turkey
Jingsong Li, China
Priya Murugasen, India
Nathaniel Emeka Urama, Nigeria
Barbara Małgorzata Sensuła, Poland
Service Opare, Canada
Che Abd Rahim Bin Mohamed, Malaysia Maheswaran
Rathinasamy, India
Jianhui Bai,China
Osvaldo Luiz Leal De Moraes, Brazil
Ranis Nail Ibragimov, United States
Masoud Masoudi, Iran
Pallav Purohit, Austria
B. Yashwansingh Surnam, Mauritius
Lucas Lavo Antonio Jimo Miguel, Mozambique
Nastaran Parsafard, Iran
Sarvan Kumar, India
Abderrahim Lakhouit, Canada
B.T. Venkatesh Murthy, India
Olusegun Folarin Jonah, United States
Amos Apraku, South Africa
Foad Brakhasi, Iran
Chian-Yi Liu, Taiwan, China
Mohammad Moghimi Ardekani, South Africa
Yuzhu Wang, China
Zixian Jia, France
Md. Mosarraf Hossain, India
Prabodha Kumar Pradhan, India
Tianxing Wang, China
Bhaskar Rao Venkata Dodla, India
Lingling Xie, China
Katta Vijaya Kumar, India
Xizheng Ke, China
Habibah Lateh, Malaysia
Meng Gao, China
Bo Hu, China
Akhilesh Kumar Yadav, India
Archana Rai, India
Pardeep Pall, Norway
Upaka Sanjeewa Rathnayake, Sri Lanka
Somenath Dutta, India
Kuang Yu Chang, United States
Sen Chiao, United States
Mohamed El-Amine Slimani, Algeria
Sheikh Nawaz Ali, India

Volume 4 Issue 3 • July 2021 • ISSN 2630-5119 (Online)

Journal of Atmospheric Science Research

Editor-in-Chief

Dr. José Francisco Oliveira Júnior

BILINGUAL
PUBLISHING CO.
Pioneer of Global Academics Since 1984

BILINGUAL
PUBLISHING CO.
Pioneer of Global Academics Since 1984

Volume 4 | Issue 3 | July 2021 | Page1-62

Journal of Atmospheric Science Research

Contents

Editorial

Articles

BILINGUAL PUBLISHING CO.
Pioneer of Global Academics Since 1984

Journal of Atmospheric Science Research
https://ojs.bilpublishing.com/index.php/jasr

ARTICLE

Objective Synoptic Weather Classification on Air Pollution during Winter Seasons in Hangzhou

Jiaqi Zhao[1,2] **Chenggang Wang**[1*]

1. Nanjing University of Information Science and Technology/Key Laboratory for Aerosol-Cloud-Precipitation, China Meteorological Administration, Nanjing, 210044, China
2. Songyuan Meteorological Bureau, Songyuan, 138005, China

ARTICLE INFO

Article history
Received: 19 May 2021
Accepted: 11 June 2021
Published Online: 30 July 2021

Keywords:
$PM_{2.5}$
PCT
Objective weather classification

ABSTRACT

Using the 2015-2018 Hangzhou city $PM_{2.5}$, PM_{10}, SO_2, CO, NO_2 and O_3 mass concentration data, ERA5 reanalysis data and ground observation data, through the PCT classification method, the objective analysis of the winter air pollution weather situation in Hangzhou was obtained. The results showed that the winter air quality concentration in Hangzhou continued to be high from 2015 to 2018, and the air pollution was the most significant. Through objective classification, it is concluded that the main weather conditions affecting the region in winter are divided into 6 types, namely high pressure control, high pressure bottom control equalizing field, L-shaped high pressure control, high pressure front control equalizing field, low pressure control, low pressure front control Equalizing field. Among them, when high pressure control, high pressure bottom control equalizing field, L high pressure control, low pressure control are affected by local sources, the impact of external sources has a greater impact on the air quality in Hangzhou, and air pollution is prone to occur; before low pressure When the pressure equalization field is controlled by the Ministry and the pressure equalization field is controlled by the high pressure front, the local wind and precipitation in Hangzhou are relatively high, which is not conducive to the accumulation of air pollutants. The probability of occurrence of air pollution is small, and air pollution is not easy to occur.

1. Introduction

The formation of air pollution is closely related to meteorological conditions. Different meteorological conditions play a key role in the dilution and diffusion of air pollutants, dry and wet precipitation and secondary conversion. Previous studies have shown that the factors affecting air pollution are not only the emission source, but also the weather situation [1-3]. Urban air pollution is caused by cross-regional advection of air pollutants, horizontal and vertical mixing in the mixed layer, anthropogenic emissions, dry and wet deposition, and photochemical reactions. The external factors affecting air pollution are caused by changes in weather conditions. Changes in weather conditions [4-7]. Predecessors have done a lot of research on the impact of changes in meteorological conditions on air pollution. For example, Wu Dui et al. [8] pointed out that the adverse effects of meteorological conditions have aggravated the

---

*Corresponding Author:
Chenggang Wang,
Nanjing University of Information Science and Technology/Key Laboratory for Aerosol-Cloud-Precipitation, China Meteorological Administration, Nanjing, 210044, China;
Email: sky641055@163.com*

DOI: https://doi.org/10.30564/jasr.v4i3.3256

accumulation of atmospheric pollutants in the mixed layer and increased the probability of urban smog. Zhang Renhe et al. [9] caused most of my country's continuous According to the meteorological conditions of haze weather, unfavorable meteorological factors are the main factors leading to the occurrence of severe haze events. Therefore, categorizing the types of atmospheric circulation can better analyze the relationship between air pollution and atmospheric circulation, and play an important role in the prediction of air pollution. At present, there are two types of objective classification research. One is the source. In the last century, through subjective empirical analysis, different weather classifications were obtained. For example, Meng Yanjun et al. [10] used empirical weather classification to conclude that when Beijing is controlled by low-pressure ground weather conditions, it is easy to cause air pollution; Zhou Ningfang et al. [11] Through forecasting experience and synoptic principles, we classified the atmospheric circulation that affects China in winter, and concluded that three weather conditions are most likely to cause haze in China; Zhang Guolian et al. [12] obtained the impact of winter on Shanghai by empirical classification. There are 11 types of weather conditions, 4 of which are most likely to cause PM_{10} pollution. Through empirical analysis, Dai Zhujun et al. [13] found that ground cold fronts and pressure equalization fields are one of the main factors that cause severe haze in autumn and winter in Jiangsu Province. However, in practical applications, it is found that subjective weather classification depends on personal experience and understanding of professional knowledge, which is prone to deviation and difficult to verify, and gradually withdraws from mainstream research. The other is a weather classification method based on mathematical statistics. It uses meteorological data as cluster analysis as the theoretical basis, with sufficient mathematical basis and relatively small error. Among them, Ngan et al. [14] used a two-level cluster analysis method to classify the weather situation and wind field in eastern Texas, USA, and obtained the characteristics of ozone under the weather classification; Zhang et al. [15] analyzed by PCA Nine weather systems that affect Beijing summer air quality in 2008 were identified; Hsu et al. [16] used a two-stage clustering method to classify weather types using surface winds and found that Taiwan is likely to cause $PM_{2.5}$ under the conditions of high-pressure circulation in the mainland. The occurrence of pollution. Xu Jianming et al. [17] used PCT weather classification to find that cold fronts and H weak atmospheric pressure are beneficial to the transmission of pollutants in Shanghai and are likely to cause urban pollution. Zhang Ying et al. [18] used the PCT classification method to obtain the fractal characteristics of air pollution weather affecting North China in the winter half of the year. Therefore, objective classification of weather conditions can reduce empirical errors. It is the development future of future weather situation classification.

Hangzhou is located at the southern foot of the Yangtze River Delta, one of the major cities in the region. Since the National Air Pollution Prevention and Control Action Plan was promulgated in 2013, the atmospheric environment has improved significantly, but winter air pollution incidents continue to occur frequently, and air pollution control still needs to be persistent. Therefore, this article will use the objective classification method to classify the different weather situation types that affect Hangzhou in winter based on the analysis of the air pollution in Hangzhou in the winter from 2015 to 2018. The occurrence characteristics of air pollution provide a reference for the air pollution prevention and control measures formulated by the Hangzhou Municipal Government.

2. Data and Methods

2.1 Data Sheet

(1) ERA5 (The fifth generation ECMWF reanalysis for the global climate and weather) provided by the European Centre for Medium-Range Weather Forecasts (ECMWF) with a 1h global atmospheric reanalysis grid point Data, the time range is from January 1, 2015 to December 31, 2018, the horizontal resolution is 0.25°×0.25°, and variables such as sea level pressure (SLP) and 10m wind field (U and V) are extracted as the research Object, used for classification of objective weather situation. The boundary layer height (PBLH) is extracted to replace the mixed layer height in the calculation of atmospheric environmental capacity. (2) The hourly average $PM_{2.5}$, PM_{10}, CO, O_3, SO_2, NO_2 mass concentration data provided by the National Air Quality Monitoring Network (beijingair.sinaapp.com) at 17 state-controlled ambient air automatic monitoring points in Hangzhou, time range From January 1, 2015 to December 31, 2018, it was used to evaluate the environmental quality of $PM_{2.5}$, PM_{10}, CO, O_3, SO_2, and NO_2 in Hangzhou. (3) The hourly ground meteorological observation data (simultaneous period) provided by Hangzhou Meteorological Bureau including Hangzhou, Lin'an, Fuyang, Tonglu, Jiande and Chun'an, 6 national meteorological observation stations, including: Air pressure, horizontal wind direction, wind speed, temperature, precipitation, and relative humidity are used to analyze and calculate the characteristics of Hangzhou's atmospheric environmental capacity under the objective weather situation classification.

DOI: https://doi.org/10.30564/jasr.v4i3.3256

2.2 PCT Objective Classification Method

There are two commonly used weather situation classification methods [19-20], subjective classification and objective classification respectively. Compared with the objective weather situation classification, the subjective classification depends on experience, and the limitations are particularly prominent. Therefore, the objective weather situation classification has gradually developed. This paper chooses the method based on obliquely rotated principal analysis in T mode (PCT method) [21]. This method rotates the principal component analysis element of the T mode, and finally obtains the spatial distribution of the physical quantity field when the absolute value of the principal component element is the largest. Through this method, the original flow field is more accurately reflected without too much change due to the adjustment of the parting object, and the obtained space field is also relatively stable. This article adopts the weather software developed by the European COSTTION733 project, and the classification software Cost733-1.2 is downloaded from the project's official website (http://cost733.geo.uni-aixgsburg.de) [22]. Extract the daily mean sea level pressure field (SLP) from January, February and December 2015-2018 from the ERA5 data as the typed physical quantity field, and multivariate the daily mean 10m horizontal wind field (U and V) during this period Oblique rotation decomposition is to expand multiple physical quantities in time and space, and then obtain a more objective and accurate atmospheric circulation pattern.

3. Results and Discussion

3.1 Comparative Analysis of the Annual and Winter Mass Concentrations of Major Air Pollutants in Hangzhou

According to the second-level limit of daily average mass concentration of six air pollutants including $PM_{2.5}$, PM_{10}, SO_2, CO, NO_2 and O_3 [23], the basic characteristics of air quality in Hangzhou are analyzed, and the results show that Hangzhou's CO and SO_2 During 2015-2018, the number of days exceeding the standard was 0, which did not cause air pollution. During this period, the number of days of O_3 exceeding the standard of air pollution was only 3 days, which had little impact on air pollution in Hangzhou, so this article will not discuss it. Comprehensive analysis shows that the main air pollutants affecting Hangzhou are NO_2, $PM_{2.5}$, and PM_{10}. Among them, $PM_{2.5}$ and PM_{10} affect human life and health, and are also the focus of society and air pollution academia. NO_2 is an important pollution of photochemical smog. One of the things has attracted more and more attention.

Figure 1 shows the annual and winter changes of the three air pollutants, NO_2, PM_{10}, and $PM_{2.5}$, which mainly affect air pollution in Hangzhou. It can be seen from the figure that, except for NO_2, the average mass concentration of $PM_{2.5}$ and PM_{10} shows a decreasing trend year by year, and the mass concentration of NO_2 has a rising trend. The days of air pollution caused by the daily average mass concentrations of NO_2, PM_{10} and $PM_{2.5}$ exceeding national standards [24] were 167, 154, and 294 days, respectively. Among them, the number of days when pollution occurred in winter was 78, 101, and 179 days, and that occurred in winter. The number of air pollution days accounted for 47%, 66% and 61% of the annual pollution days, indicating that the winter has the most significant impact on the air quality of Hangzhou. In particular, the number of days of heavy pollution (31 days) in which the average daily mass concentration of $PM_{2.5}$ in Hangzhou in winter exceeds the national standard [25] accounts for 94% of the number of days (33 days) of heavy pollution in the year, which further illustrates the cause of air pollution in Hangzhou. The most important pollutant is $PM_{2.5}$.

3.2 Type Analysis of Objective Weather Situation

In order to more accurately analyze the characteristics of atmospheric environmental capacity in different weather conditions that affect Hangzhou in winter, this study uses ERA5 to reanalyze data and adopts the PCT classification method. December) 20~45°N, 90°~130°E area (this area covers the main weather circulation processes affecting Hangzhou in the short term) sea level pressure (SLP) field, 10m horizontal wind field (U and V) Carry out cluster analysis, which are defined as high-pressure control weather situation (hereinafter referred to as H-type), high-pressure bottom control weather situation (HB-type), L-type high-pressure control weather situation (HL-type), and high-pressure front control averaging field weather situation (HF type), low pressure control weather situation (L type), low pressure front control pressure equalization field weather situation (LF type). Details are as follows:

(1) H type (appearing frequency is 22%)

This type of central Hangzhou area is located in the central area of cold high pressure, and is mostly controlled by the sinking airflow. The dominant wind direction is northwest-northern wind, its frequency is 57%, and the average daily wind speed is 2.0 m/s. This type appeared in a total of 82 days in the classification, of which the days of NO_2, $PM_{2.5}$ and PM_{10} air pollution were 23 days, 33 days and 54 days respectively, and the daily average mass

DOI: https://doi.org/10.30564/jasr.v4i3.3256

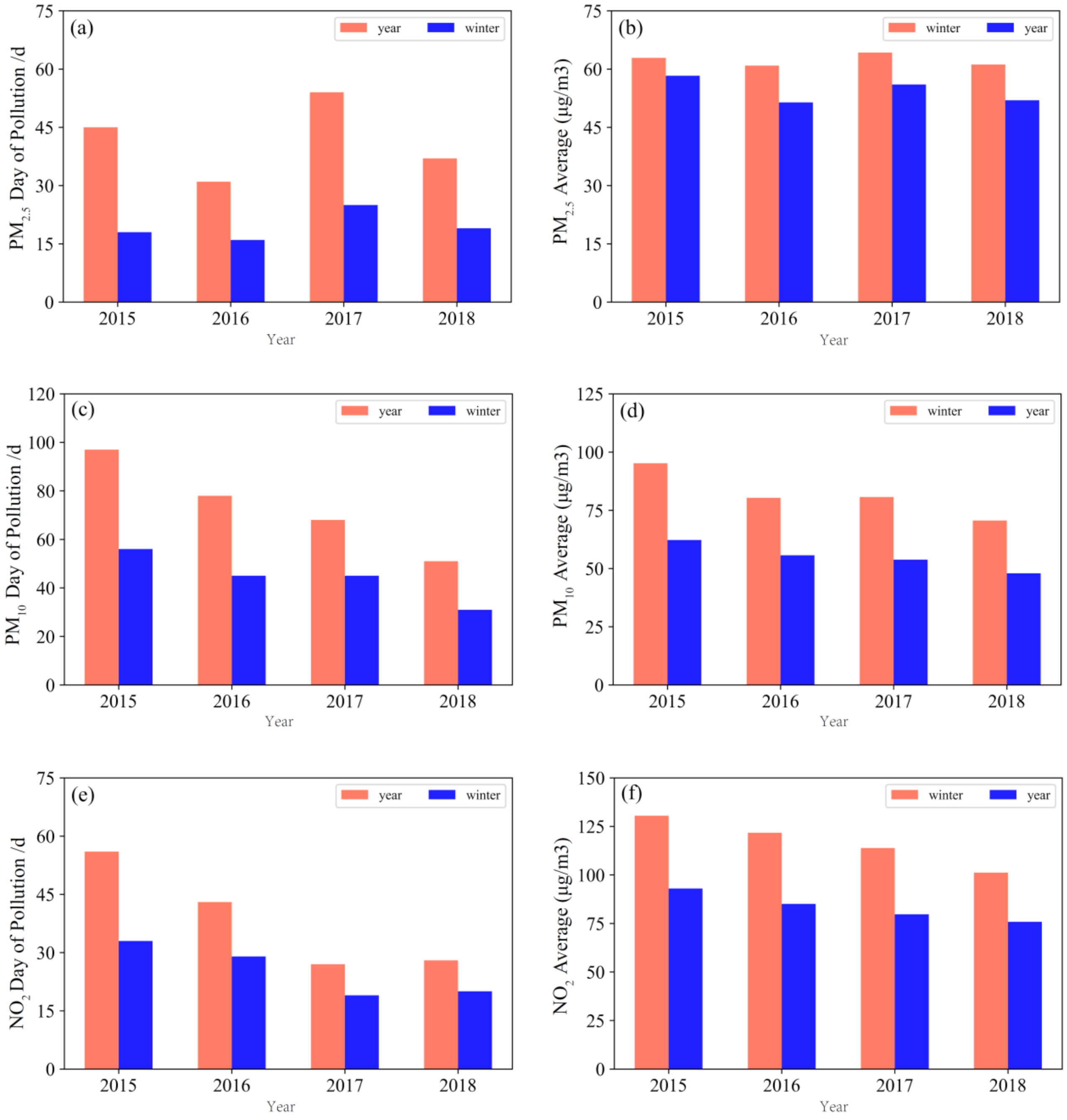

Figure 1. Comparison of the number of pollution days and corresponding mass concentrations caused by the three major air pollutants in Hangzhou from 2015 to 2018 (a. pollution days caused by NO_2; b. average mass concentration of NO_2; c. pollution caused by $PM_{2.5}$ Number of days; d. $PM_{2.5}$ average mass concentration; e. Number of days of pollution caused by PM_{10}; f. PM_{10} average mass concentration)

concentrations were 70 μg/m^3 and 134 μg/m^3 and 93 μg/m^3.

(2) HB type (appearing frequency is 11%)

This type of central Hangzhou area is at the edge of the lower part of the cold high pressure, and the main body of the high pressure center is near the north of the Huai River. Controlled by weak easterly winds and at the southern edge of the warm high pressure, the dominant wind direction is southwest-southern wind with a frequency of 41% and an average daily wind speed of 2.0 m/s. This type appeared in a total of 41 days in the classification, among which the days of NO_2, $PM_{2.5}$ and PM_{10} air pollution were 11 days, 11 days and 23 days respectively, and the daily average mass concentrations were 66 μg/m^3 and 126 μg/m^3 and 85 μg/m^3.

DOI: https://doi.org/10.30564/jasr.v4i3.3256

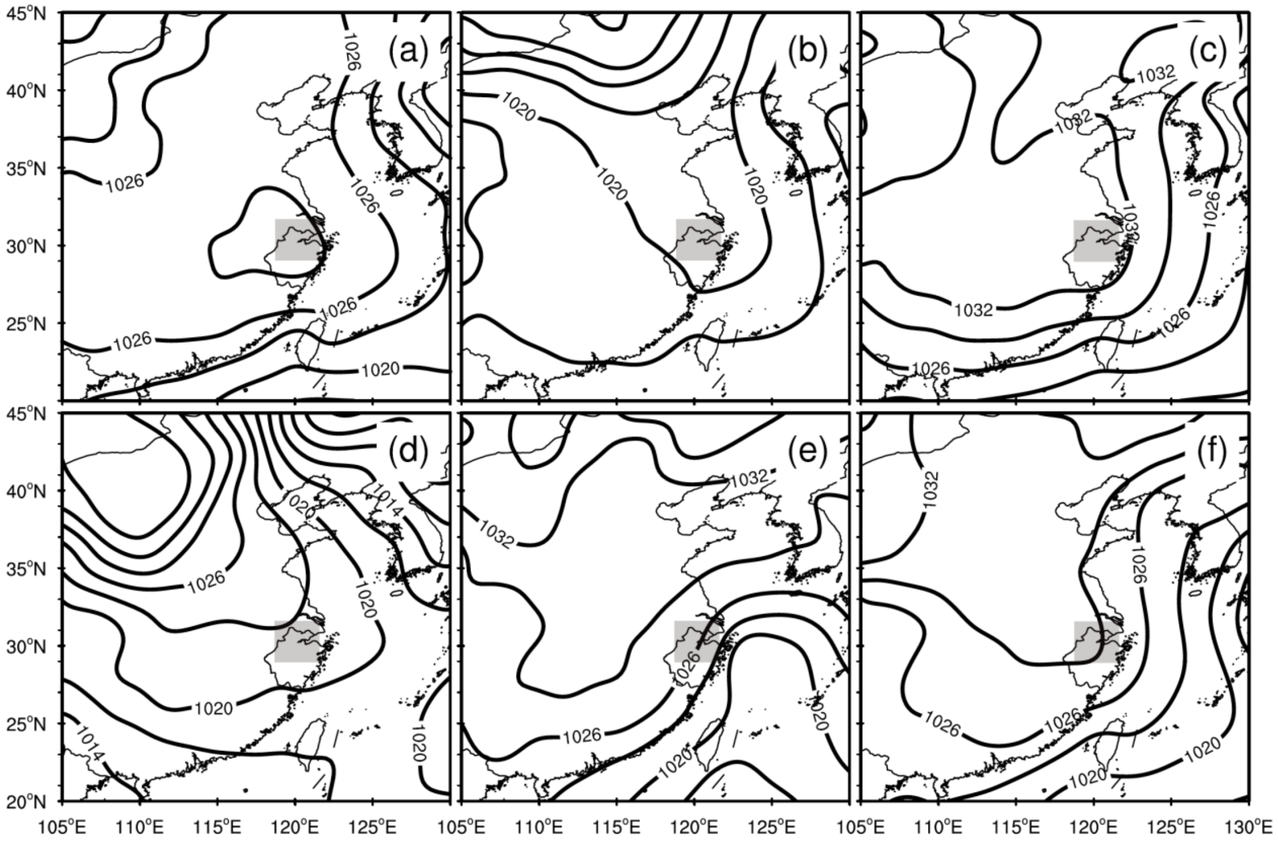

Figure 2. Classification of 6 objective weather patterns of sea level pressure and 10m wind field in winter from 2015 to 2018(a). High pressure control(b). High pressure bottom control(c). L-type high pressure control(d). High pressure front control(e). Low pressure control(f). Low pressure front control

(3) HL type (appearing frequency is 15%)

In this type, the city of Hangzhou is located in the front area of the cold high pressure, which is mostly similar to the L shape. The main body of the high pressure center extends from the northwest-Hetao to the middle and lower reaches of the Yangtze River. The dominant wind direction is northeast-northern wind, with a frequency of 43%, and an average daily wind speed of 2.1 m/s. This type appeared in a total of 53 days in the classification, among which the number of days with NO_2, $PM_{2.5}$ and PM_{10} air pollution were 15 days, 16 days and 21 days respectively, and the daily average mass concentrations were 58 μg/m^3 and 120 μg/m^3 and 84 μg/m^3.

(4) HF type (appearing frequency is 24%)

This type of middle-Hangzhou city is located close to the front area of the cold high pressure. The high pressure center is mostly located in the key areas of the cold wave from Mongolia to Inner Mongolia. The dominant wind direction is northwest-northern wind, with a frequency of 69% and an average daily wind speed of 2.4 m/s. This type appeared in 86 days in the classification, among which the number of days with NO_2, $PM_{2.5}$ and PM_{10} air pollution were 7 days, 10 days and 31 days, and its daily average mass concentration was 55 μg/m^3, 96 μg/m^3 and 67 μg/m^3.

(5) L type (occurrence frequency is 8%)

This type of middle Hangzhou city is located in a low-pressure control area, and the affected systems are mostly transit low-pressure troughs, inverted troughs, and stationary fronts. The dominant wind direction is northwest-northeast wind with a frequency of 54% and an average daily wind speed of 1.8 m/s. This type appeared in 28 days in the classification, among which the number of days with NO_2, $PM_{2.5}$ and PM_{10} air pollution were 18 days, 19 days and 25 days, and its daily average mass concentration was 88 μg/m^3, 174 μg/m^3 and 118 μg/m^3.

(6) LF type (appearing frequency is 20%)

In this type, Hangzhou is located at the front edge of the low-pressure center; cold advection passes through the high altitude, bringing in the cold air mass in North China, and is affected by the weakly cold air "back flowing" from the East China Sea. The highest frequency of occurrence is northwest-northern wind. , The frequency of occurrence is 72%, and the average daily wind speed is 2.4 m/s. This

DOI: https://doi.org/10.30564/jasr.v4i3.3256

type appeared in a total of 71 days in the classification, of which the days of NO_2, $PM_{2.5}$ and PM_{10} air pollution were 4 days, 12 days and 25 days, and the daily average mass concentrations were 54 μg/m^3, 93 μg/m^3 and 69 μg/m^3.

Analyzing 6 types of weather situation, we can see that the weather situation that mainly affects Hangzhou in the winter of 2015-2018 is the high-pressure front control equalizing field, which is also consistent with the work of the predecessors [26-27].

3.3 Discussion on the Impact of Meteorological Elements on Air Pollution under the Objective Weather Classification in Hangzhou in Winter

Changes in weather conditions such as wind speed, temperature, precipitation and humidity are the main factors that determine the formation of air pollution. Table 1 shows the statistical analysis and comparison of meteorological elements and the average mass concentration of $PM_{2.5}$, PM_{10} and NO_2 under different weather conditions. From the table, it can be seen that the lowest average temperature in Hangzhou during the winter of 2015-2018 under LF type control was 4.4°C, and the winter during the four years The lowest temperature also appears under the control of LF type, which is -5°C. Under other weather types, the winter temperature in Hangzhou is relatively high, at 6-10°C; the average daily wind speed is the second highest, 2.3 m/s, The average mass concentrations of $PM_{2.5}$, PM_{10}, and NO_2 are the lowest, 69 μg/m^3, 93 μg/m^3, 54 μg/m^3, respectively, indicating that Hangzhou is affected by cold low pressure in winter, and the surface wind speed is relatively high, which is beneficial to air pollution. The vertical and horizontal diffusion of air pollutants, coupled with the influence of cold air, negative changes in temperature, and more precipitation, have obvious moisture removal effects of air pollutants, so the pollutant concentration is the lowest. Under HF type control, due to the impact of weak cold air moving eastward and southward, the average daily wind speed in Hangzhou is the highest at 2.4 m/s. The cold wind gradient is large, which is conducive to the wet removal of pollutants. Therefore, $PM_{2.5}$, PM_{10} The mass concentration of NO_2 and NO_2 pollutants is also relatively low, followed by 67 μg/m^3, 96 μg/m^3, 55 μg/m^3; while in H-type and LF-type control, the average daily wind speed is relatively small, and the atmosphere The vertical and horizontal diffusion capacity of pollutants is weak, the local relative humidity gradually decreases, and the temperature gradually rises under the influence of solar radiation. The overall mixing layer is relatively stable, which is conducive to the accumulation of atmospheric pollutants. Therefore, the mass concentration of air pollutants is relatively High; the HL type control is similar to the H and LF type control, but due to the high precipitation process in Hangzhou under this type, the humidity is relatively high, and the mixed layer is prone to temperature inversion. In addition, the humidity is high, and the pollutant particles will absorb moisture and increase. Air pollution is generated; while Hangzhou is under the control of L-shaped weather situation, because its daily average wind power is the smallest, 1.8 m/s, the horizontal diffusion ability is the worst, and under the L-shaped control, there is a lot of precipitation and the solar radiation is weak. The mixed layer does not develop vigorously. The lower mixed layer is conducive to the accumulation of atmospheric pollutants and is not conducive to diffusion, so air pollution is most likely to form. Among them, the average mass concentration of $PM_{2.5}$, PM_{10} and NO_2 is the highest, respectively 118 μg/m^3, 174 μg/m^3, 88 μg/m^3, all exceed the national air quality level II standard. Therefore, changes in meteorological conditions under different weather conditions restrict the occurrence, development and extinction of air pollution in Hangzhou.

Table 1. Statistical analysis of meteorological elements and average mass concentrations of $PM_{2.5}$, PM_{10} and NO_2 under different weather conditions

	H Type	HB Type	HL Type	HF Type	L Type	LF Type
Average Temperature (°C)	6.2	9.4	8.9	6.9	8.7	4.4
Average relative humidity (%)	63	61	78	72	71	73
Average precipitation (mm)	2.7	2.4	8.1	5.9	7.3	6.9
Average precipitation (m/s)	2.0	2.0	2.1	2.4	1.8	2.3

3.4 Discuss the Analysis of Air Pollution Characteristics under the Objective Weather Classification in Winter of Hangzhou

3.4.1 Statistical Analysis of $PM_{2.5}$, PM_{10} and NO_2 Air Pollution under Objective Weather Classification in Hangzhou in Winter

Cluster analysis is performed on the sea level pressure (SLP) field and the 10m horizontal wind field (U and V) in the main weather circulation process in Hangzhou, and Table 2 is defined as $PM_{2.5}$ and PM_{10} under six

Table 2. Frequency of $PM_{2.5}$, PM_{10}, and NO_2 air pollution days and clean days under the 6 weather types

Pollutants	Pollution level	H Type	HB Type	HL Type	HF Type	L Type	LF Type
$PM_{2.5}$	Heavy pollution	8%	17%-	17%	3%	18%	4%
	Moderately polluted	15%	7%	6%	5%	32%	11%
	Light pollution	43%	39%	17%	28%	40%	20%
	Clean day	34%	37%	60%	64%	10%	65%
PM_{10}	Heavy pollution	0	0	0	0	0	0
	Moderately polluted	0	0	8%	0	4%	0
	Light pollution	40%	27%	23%	12%	64%	17%
	Clean day	60%	73%	69%	88%	32%	83%
NO_2	Light pollution	28%	27%	28%	8%	64%	6%
	Clean day	72%	73%	72%	92%	36%	94%

weather types. Figure 3 shows the frequency and average mass concentration distribution of $PM_{2.5}$, PM_{10} and NO_2 polluted days under different weather conditions.

As shown in Table 2 and Figure 3, the three main pollutants ($PM_{2.5,}$ PM_{10}, and NO_2) that affect air pollution in Hangzhou are roughly the same according to the frequency of air pollution days, and the cumulative frequency of $PM_{2.5}$ air pollution days is in order. From high to low, they are L, H, HB, HL, HF, and LF; the cumulative frequency of PM_{10} air pollution days is L, H, HL, HB, LF, and HF from high to low; and NO_2 air The cumulative frequency of pollution days from high to low is L, H, HL, HB, HF and LF respectively. Through comparison, it can be seen that the three pollutants $PM_{2.5}$, PM_{10} and NO_2 that affect Hangzhou's winter air pollution correspond to L-type weather types with the highest frequency of air pollution occurrences, with frequencies of 89%, 68%, and 64%, respectively. The average mass concentrations of $PM_{2.5}$, PM_{10} and NO_2 are 118 $\mu g/m^3$, 174 $\mu g/m^3$ and 88 $\mu g/m^3$, which all exceed the national secondary standards [29], indicating that Hangzhou is in L Type H is the most prone to air pollution; the second is H type. The daily frequency of $PM_{2.5}$, PM_{10} and NO_2 air pollution is 66%, 40% and 28%, and the average mass concentration is 93 $\mu g/m^3$, 134 $\mu g/m^3$ and 70 $\mu g/m^3$, of which the daily average mass concentrations of PM_{10} and NO_2 are lower than the national secondary standards [28]. The weather types with the lowest occurrence frequency of air pollution are HF and LF. The daily frequency of $PM_{2.5,}$ PM_{10} and NO_2 air pollution is 36%, 12%, 8% and 25%, 17%, 6%, and the average The mass concentrations in order are 67 $\mu g/m^3$, 96 $\mu g/m^3$, 55 $\mu g/m^3$, 69 $\mu g/m^3$, 93 $\mu g/m^3$, 54 $\mu g/m^3$, which affect Hangzhou City under different weather conditions. Except for the two pollutants of air pollution (PM_{10} and NO_2), the average mass concentration exceeds the national second-level standard under the L-type, and the corresponding average mass concentration under the other five weather conditions does not exceed the national second-level air quality For $PM_{2.5}$, it shows that the average mass concentration of Hangzhou in winter under the control of the four weather conditions of L, H, HB and HL exceeds the national air quality level II standard. Statistics of the daily occurrence frequency and average mass concentration distribution of air pollution corresponding to the six weather types show that the occurrence frequency of air pollution days in Hangzhou during L, HB, H, and HL type control in winter is significantly higher than that of HF and LF type control. Especially $PM_{2.5}$ is the most obvious.

According to statistics on the frequency of clean days under different weather conditions, it can be seen that in addition to the opposite conclusions from the above, it can be found that the most frequent weather conditions for $PM_{2.5}$, PM_{10} and NO_2 cleaning days in Hangzhou from 2015 to 2018 are HF and LF types , Under the control of HF and LF, the frequency of $PM_{2.5}$ cleaning days is 64% and 65%; the frequency of PM_{10} cleaning days is 88% and 83%; the frequency of NO_2 cleaning days is 92%, 94% And in 2015-2018, the frequency of $PM_{2.5,}$ PM_{10}, and NO_2 in the above two types of weather conditions, the frequency of clean days exceeded more than 60% of the total number of days in the corresponding weather types. It shows that Hangzhou is not prone to air pollution in winter under the control of HF and LF, and when Hangzhou is under the control of the other four different weather conditions (L, H, HB and HL), in addition to

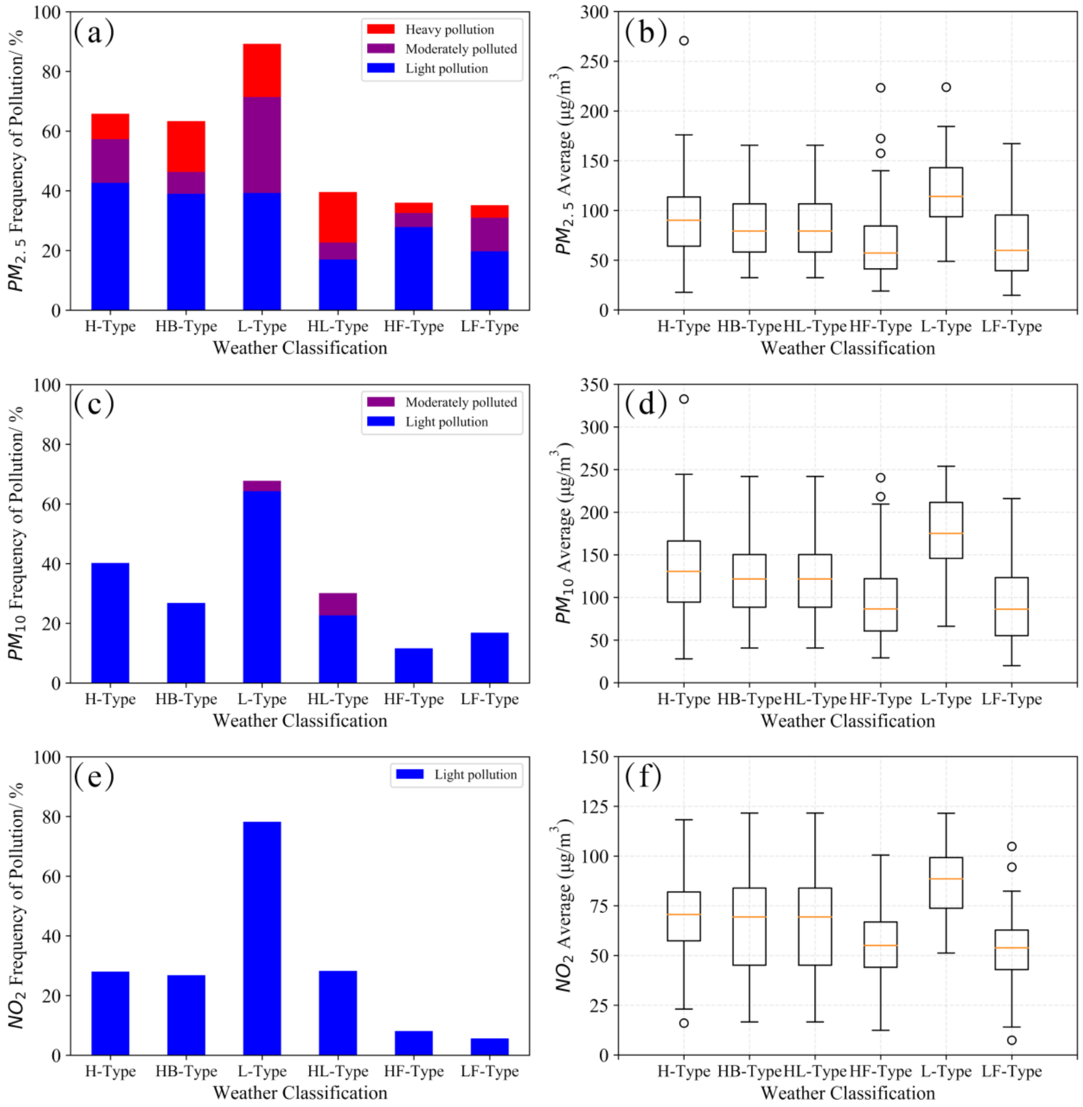

Figure 3. The occurrence frequency and average mass concentration distribution of air pollution days corresponding to different weather types (a. $PM_{2.5}$ air pollution day occurrence frequency; b. $PM_{2.5}$ average mass concentration distribution; c. PM_{10} air pollution day occurrence frequency; d. PM_{10} average mass concentration distribution; e. NO_2 air pollution day frequency; f. NO_2 average mass concentration distribution)

$PM_{2.5}$, PM_{10} and NO_2 The frequency of corresponding clean days exceeded 60%, which further shows that $PM_{2.5}$ is the main pollutant causing air pollution in Hangzhou, followed by PM_{10} and NO_2.

3.4.2 Discussion on the Potential of Air Pollution under Different Weather Types in Hangzhou in Winter

In order to explore the potential trend of air pollution caused by the three air pollutants of $PM_{2.5}$, PM_{10} and NO_2 under different weather types in winter of Hangzhou, based on the short-term no change in the air pollutant emission control in Hangzhou, this paper calculates Corresponding to the 6 weather conditions under objective weather classification, the daily mass concentration of $PM_{2.5}$, PM_{10}, and NO_2 is subtracted from the average mass concentration of the previous day to analyze and remove the factors of anthropogenic emissions, only pollution caused by changes in weather conditions Potential occurs.

It can be seen from Figure 4 that when the air pollutant difference is positive, it means that the air pollution caused by this pollutant is gradually increasing, while a negative value means that the air pollution caused by this pollutant is gradually reducing. The potential laws of air pollution in the 6 different weather types are basically the same. Among them, the air pollution is most likely to increase under the control of HB and L types, and the difference between

DOI: https://doi.org/10.30564/jasr.v4i3.3256

the daily average mass concentrations of $PM_{2.5}$, PM_{10} and NO_2 and the previous day. All positive values are 2.8 μg/m³, 1.3 μg/m³, 4.5 μg/m³, 1.3 μg/m³, 1.3 μg/m³, 1.4 μg/m³; while LF and HF type control. The difference between the daily average mass concentration of $PM_{2.5}$ and PM_{10} and the previous day are negative values, in order -0.1 μg/m³, -0.8 μg/m³, -0.1 μg/m³, -0.6 μg/m³. Although the difference of NO_2 is positive, it is the minimum; combined with the above conclusions, it can be seen that when Hangzhou is controlled by HB, L, HL and H in winter, it is beneficial to the increase of air pollutant concentration, and air pollution occurs. The potential of, belongs to the type that is prone to polluting weather; while under the control of LF and HF, it is not conducive to the increase of the mass concentration of air pollutants and the maintenance of pollution, and it belongs to the type of weather that is not prone to pollution.

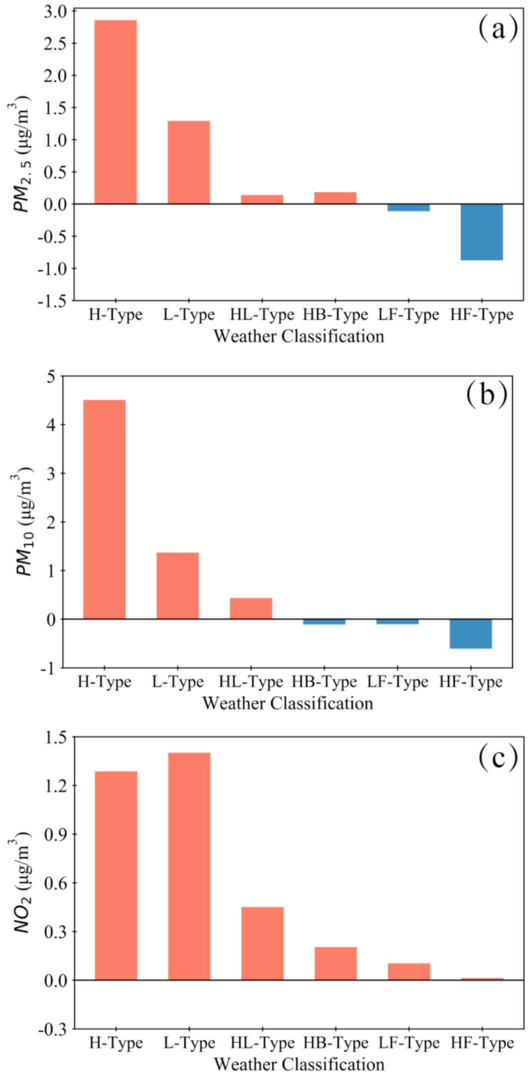

Figure 4. The difference between the daily air pollutant mass concentration and the previous day under different weather types (a.$PM_{2.5}$, b.PM_{10}, c.NO_2)

3.5 Analysis of Potential Sources of $PM_{2.5}$ Air Pollution under the Objective Weather Classification in Winter of Hangzhou

3.5.1 Cluster Analysis of Air Pollution Trajectories under Different Weather Conditions

Since air pollution is not only affected by local pollution sources, but also by the inter-regional transportation of pollutants in surrounding areas, there are obvious differences in pollution source areas under different weather conditions. In order to further explore the potential differences in air pollution in Hangzhou under different weather conditions, it can be seen from the above that $PM_{2.5}$ is the most important air pollutant that affects air pollution in Hangzhou in winter. Therefore, in order to further explain the source analysis of air pollution in Hangzhou under different weather conditions, this section focuses on the process of $PM_{2.5}$ air pollution instead. Using TrajStat software developed by HYSPLIT to do a backward 48-hour cluster analysis of different weather types in Hangzhou in winter, see Figure 5.

The gray in the figure is the trajectory route under all weather classifications, and the black line is the maximum 3 trajectory routes obtained by cluster analysis under each weather classification. The main air masses that affect Hangzhou under H-type control come from Inner Mongolia. Passing through Beijing-Tianjin-Hebei, Anhui, Jiangsu and other places, accounting for 47%; while under the control of HB, HL, HF and LF, the main air masses affecting Hangzhou are from places passing through Hunan, Jiangxi, and southwestern Zhejiang, accounting for They are 49%, 41%, 41%, and 40% respectively; while the main air mass in the L-shape is the circling through Shanghai to the eastern Zhejiang region, which affects Hangzhou, accounting for 40%.

3.5.2 Analysis of Potential Sources and Contribution Ratios of $PM_{2.5}$ Pollution under Different Weather Conditions

Through the clustering of air mass trajectories, the main air mass paths that affect Hangzhou under different weather conditions are obtained. In order to further find out the pollution sources and pollution contributions that affect Hangzhou, TrajStat software is used, and the potential source contribution factor method (WPSCF) and pollutants are used. The mass concentration weighted trajectory analysis method (WCWT) is used for analysis, as shown in Figures 6 and 7.

Among them, WPSCF analysis defines that the probability of occurrence is greater than or equal to 0.5 as

DOI: https://doi.org/10.30564/jasr.v4i3.3256

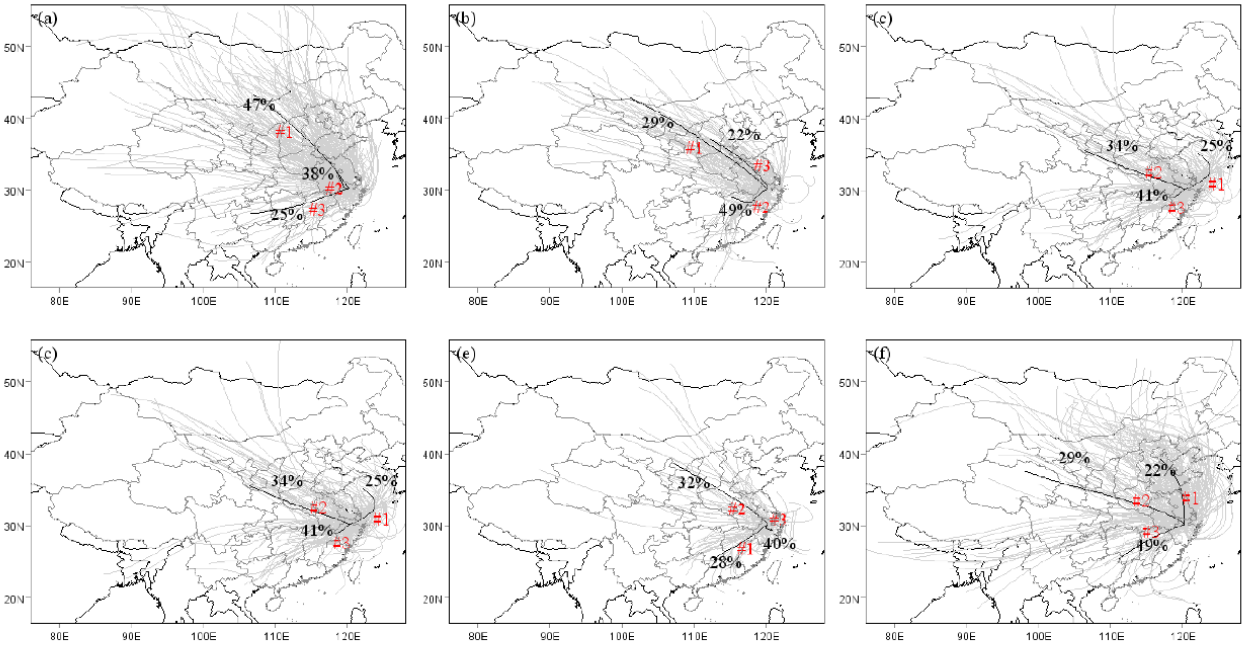

Figure 5. Cluster analysis of $PM_{2.5}$ backward trajectory under different weather types (a.H type, b.HB type, c. HL type, d.HF type, e.L type, f.LF type)

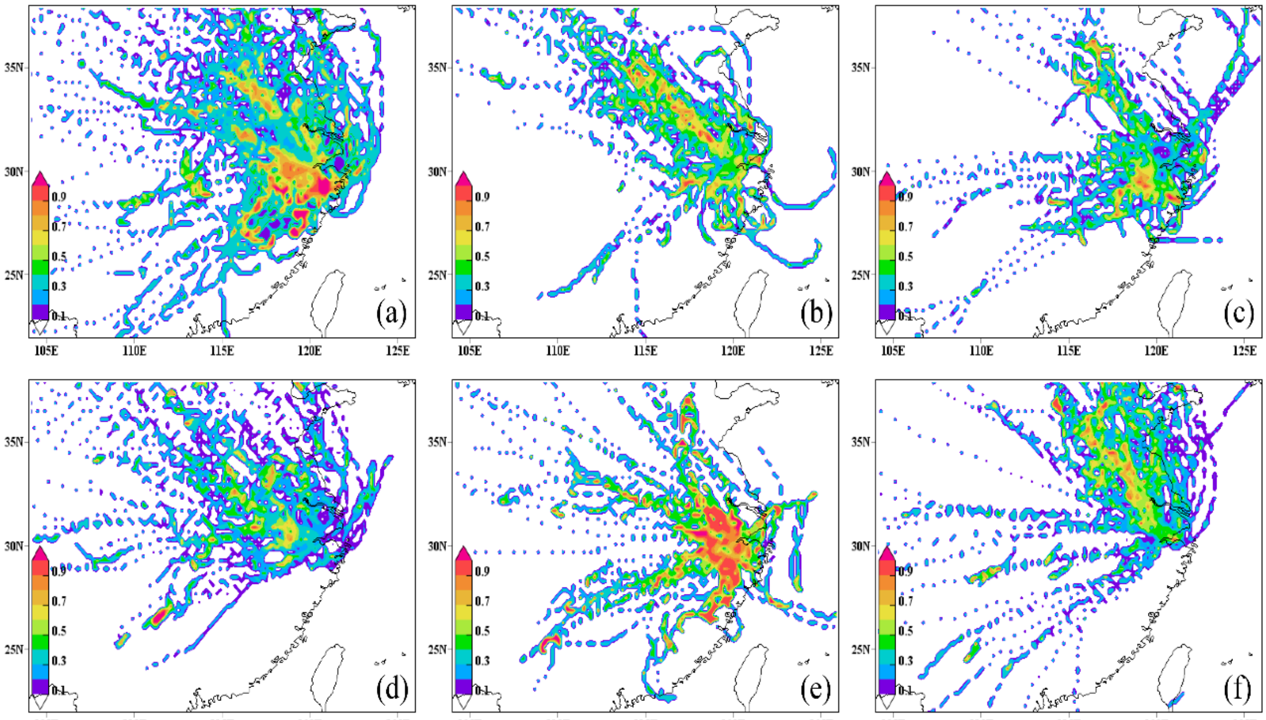

Figure 6. WPSCF analysis of $PM_{2.5}$ pollution under different weather types (a.H type, b.HB type, c. HL type, d.HF type, e.L type, f.LF type, unit: %)

the potential air pollution source affecting the area, and greater than or equal to 0.9 is the main air pollution source affecting the area. From the figure, it can be seen that the main pollution source in Hangzhou is in addition to the local area under H-type control. In Shaoxing, Jinhua, Quzhou and other places, the probability of occurrence exceeds 0.9, the contribution rate of $PM_{2.5}$ air pollution is 100 $\mu g/m^3$, while the impact of Anhui and Jiangsu also exceeds 0.7, and the contribution rate of $PM_{2.5}$ air pollution is 90 $\mu g/m^3$; under HB type control, the main pollution

DOI: https://doi.org/10.30564/jasr.v4i3.3256

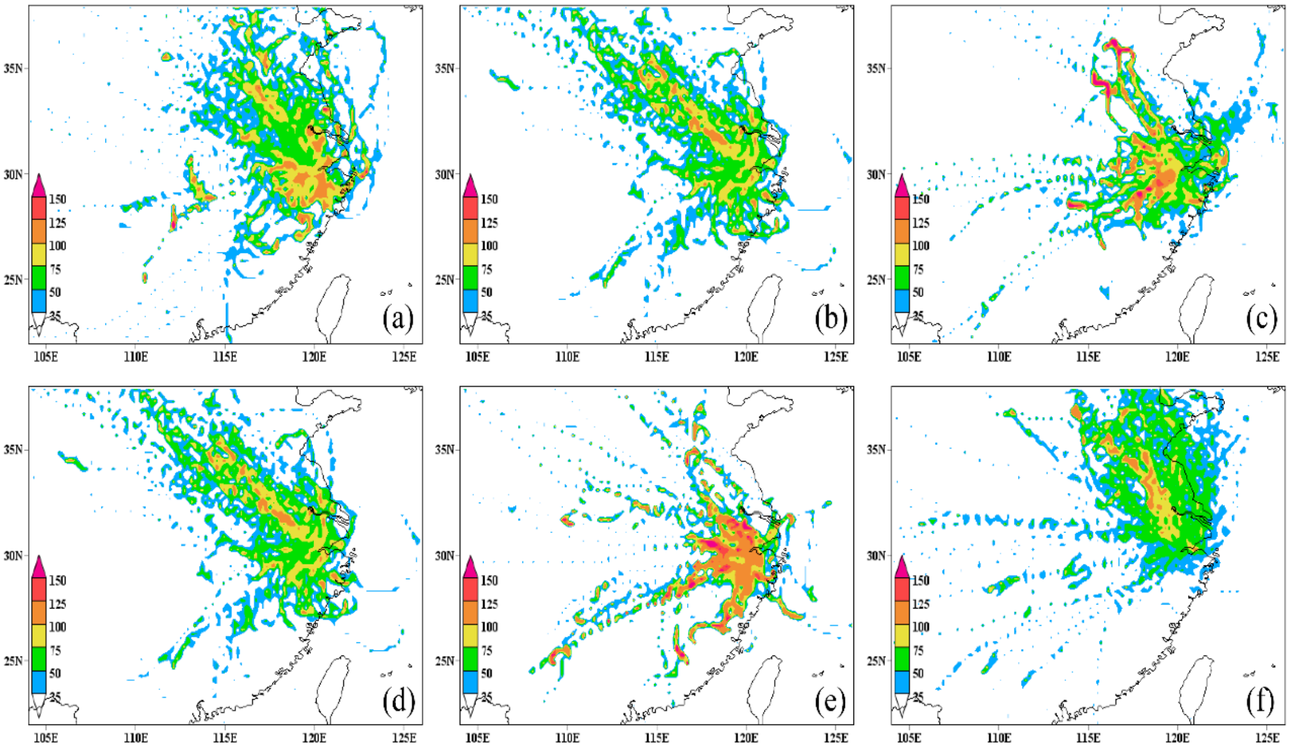

Figure 7. WCWT analysis of $PM_{2.5}$ pollution under different weather types (a.H type, b.HB type, c. HL type, d.HF type, e.L type, f.LF type, unit: μg/m^3)

sources are southern Jiangsu and central and western regions of Zhejiang, with the probability of occurrence exceeding 0.9, followed by the local and western regions of Zhejiang, with the probability of occurrence exceeding 0.7, and $PM_{2.5}$ contributes to air pollution The air pollution rate is 110 and 90 μg/m^3 respectively; under the control of HL type, the main pollution sources are the western Zhejiang region and the local region, followed by the southern Jiangsu region, with the probability of occurrence being 0.8, 0.6 and 0.5. $PM_{2.5}$ contributes to air pollution. The processes are 140, 100, and 90 μg/m^3 respectively; under L-shaped control, the main sources are in addition to local areas, as well as central and western Zhejiang, Shanghai, southern Jiangsu, and southern Anhui. The probability of occurrence all exceeds 0.9, $PM_{2.5}$ pollution contribution degree exceeds 120 μg/m^3. Under HF control, the main source of pollution is southern Anhui, followed by the local area, with the occurrence probability exceeding 0.6 and 0.5. The contribution of $PM_{2.5}$ air pollution is 95, respectively. 75 μg/m^3; under LF type control, the main pollution sources are southern Jiangsu and local areas, with the probability of occurrence being 0.6 and 0.5, respectively. The contribution of $PM_{2.5}$ air pollution exceeds 95 and 75 μg/m^3. To sum up, Hangzhou is not only affected by local pollution sources, but also by the central and western regions of Zhejiang, southern Jiangsu and other places. Among them, the types of weather prone to pollution (H, HB, HL and L) are not only affected by local sources. In addition to the impact of the source, the impact of external sources has a greater impact on the $PM_{2.5}$ air quality in Hangzhou, especially in the L-shaped weather situation, it is necessary to increase the joint prevention and control of air pollution in the Yangtze River Delta to solve the $PM_{2.5}$ air pollution problem. However, under the weather classification (HF and LF) that are not prone to air pollution, the impact of local pollution sources is relatively small, and the impact of external sources is relatively large. However, under the influence of these two weather conditions, the wind is relatively large and there is a lot of precipitation. It is not conducive to the accumulation of atmospheric pollutants, and the atmospheric diffusion capacity is strong, so the probability of $PM_{2.5}$ air pollution is relatively small.

4. Conclusions

The PCT classification method was used to objectively analyze the winter weather situation in Hangzhou from 2015 to 2018, and the probability and quality of the air pollution potential source areas of the main air pollutants ($PM_{2.5}$, PM_{10} and NO_2) affecting Hangzhou in winter Concentration analysis, the main conclusions are as follows:

(1) According to the PCT classification method, there are 6 main weather conditions affecting Hangzhou in winter, namely HB, H, HL, L, LF and HF.

(2) Under different weather classifications, the air pollution weather patterns in Hangzhou in winter due to the influence of $PM_{2.5}$, PM_{10} and NO_2 three atmospheric pollutants are basically the same, and the weather classification with the highest frequency of air pollution days is L-type. The weather types with the lowest frequency are HF and LF. Statistics of the daily occurrence frequency and average mass concentration distribution of air pollution corresponding to the six weather types show that the daily occurrence frequency of air pollution in Hangzhou in winter under the control of L, HB, H and HL is significantly higher than that of the control under HF and LF. In particular, $PM_{2.5}$ pollution is the most obvious.

(3) According to the potential change trend of air pollution caused by the main air pollutants ($PM_{2.5}$, PM_{10} and NO_2) in different weather conditions in Hangzhou in winter, it can be seen that when Hangzhou is under the control of HB, L, HL and H Conducive to the increase of air pollutant mass concentration, it belongs to the type of polluted weather prone; while under the control of LF and HF, it is not conducive to the increase of air pollutant mass concentration and the maintenance of pollution, which belongs to the type of polluted weather that is not prone to occur.

(4) Under the six different weather classifications, Hangzhou is not only affected by local pollution sources, but also by the central and western regions of Zhejiang, southern Jiangsu and other places. Among the weather classifications that are prone to pollution (H, HB), HL and L type), in addition to local sources, the impact of external sources has a greater impact on the air quality of $PM_{2.5}$ in Hangzhou, especially in the L-shaped weather situation, the joint prevention and control of air pollution in the Yangtze River Delta region should be increased. In order to solve the problem of $PM_{2.5}$ air pollution, and under the weather classification (HF, LF type) that is not prone to air pollution, the impact of local pollution sources is relatively small, and the impact of external sources is greater, but under the control of HF and LF types , Hangzhou's local wind is relatively high and there is a lot of precipitation, which is not conducive to the accumulation of atmospheric pollutants. The atmospheric diffusion capacity is relatively strong, and the probability of $PM_{2.5}$ pollution is relatively small.

Acknowledgments

This work was supported by the National Natural Science Foundation of China (41975011), National key Research and Development Projects(2016YFA0602003), It also partially supported by Fuyang Government Funded Project of Hangzhou (ZJHCCGFY-0808001). We thanks for the meteorological data provided by the Hangzhou Meteorological Bureau.

References

[1] Ding A, Wang T, Xue L, et al. Transport of north China air pollution by mid-latitude cyclones: case study of aircraft measurements in summer 2007[J]. Geophys Res,2009,114, D08304.

[2] Ding A, Huang X, Fu C. Air pollution and weather interaction in East Asia[J]. In Oxford Reaserch Encyclopedias: Environmental Science,2017,1, 1-26.

[3] Otero N, Sillmann J, Schnell J, et al. Synoptic and meteorological drivers of extreme ozone concentrations over Europe. Environmental Research Letters, 2016, 11(2), 024005. https://doi.org/10.1088/1748-9326/11/2/024005.

[4] Gao Y, Liu X, Zhao C, et al. Emission controls versus meteorological conditions in determining aerosol concentrations in Beijing during the 2008 Olympic Games. Atmos. Chem. Phys. 2011,11, 12437-12451.

[5] Qu W, Arimoto R, Zhang X, et al. Spatial distribution and interannual variation of surface PM10 concentrations over eighty-six Chinese cities[J]. Atmos Chem Phys,2010, 10:5641-5662.

[6] Pleijel H, Grundström M, Karlsson G, et al. A method to assess the inter-annual weather-dependent variability in air pollution concentration and deposition based on weather typing[J]. Atmospheric Environment, 2016,126:200-210.

[7] Zhang Y, Ding A, Mao H, et al. Impact of synoptic weather patterns and inter-decadal climate variability on air quality in the North China Plain during 1980-2013[J].Atmospheric Environment,2016,124:119-128.

[8] Wu Dui, Liao Guolian, Deng Xuejiao, et al. Transport condition of surface layer under haze weather over the pearl river delta[J].Journal of Applied Meteorological Science, 2008,19(1):1-9.

[9] Zhang R H, Li Q, Zhang R N. Meteorological conditions for the persistent severe fog and haze event over eastern China in January 2013[J].Science China: Earth Sciences,2014,57(1):26-35.

[10] Meng Yanjun, Cheng Conglan. Impact of suface synoptic situations on air pollution in Beijing area [J]. Meteorology,2002,28(4):42-47.

[11] Zhou Ningfang, Li Feng, Rao Xiaoqin, et al. Study on haze weather in China during winter-time of 2006[J]. Meteorology,2008,34(6) :81-88.

[12] Zhang Guolian, Zhen Xinrong, Tan Jianguo, et al.

DOI: https://doi.org/10.30564/jasr.v4i3.3256

The analysis of the relationship between the air quality in shanghai and surface pressure and meteorological factos [J].Journal of Tropical Meteorology,2010,26(1) :124-128.

[13] Dai Zhujun, Liu Duanyang, Wang Hongbin, et al. The classification study of the heavy haze during autumn and winter of Jiangsu[J].Acta Meteorologica Sinica,2016,74(1) :133-148.

[14] Ngan F, Byun D. Classification of weather patterns and associated trajectories of high-ozone episodes in the Houston-Galveston-Brazoria area during the 2005/06 TexAQS-II[J]. Appl Meteorol Climatol,2011,50:485-499.

[15] Zhang J, Zhu T, Zhang Q H, et al. The impact of circulation patterns on regional transport pathways and air quality over Beijing and its surrounding[J]. Atmospheric Chemistry& Physics&Discussions,2012,11(12):33465-33509.

[16] Hsu C, Cheng F. Synoptic Weather Patterns and Associated Air Pollution in Taiwan[J]. Aerosol and Air Quality Research,2019,19:1139-115.

[17] Xu J M, Chang L Y, Ma J H, et al. Objective synoptic weather classification on $PM_{2.5}$ pollution during autumn and winter seasons in Shanghai[J]. Acta Scientiae Circumstantiae,2016, 36(12) :4303-4314.

[18] Zhang Y, Wang S G, Jia X W, et al. Study on an objective synoptic typing method for air pollution weather in North China during winter half year[J]. Acta Scientiae Circumstantiae,2018, 38(10):3826-3833.

[19] Compagnucci R, Richman M. Can principal component analysis provide atmospheric circulation or teleconnection patterns[J]. International Journal of Climatology, 2008, 28: 703-726.

[20] Hsu C, Cheng F. Synoptic Weather Patterns and Associated Air Pollution in Taiwan[J]. Aerosol and Air Quality Research,2019,19: 1139-115.

[21] Huth R, Beck C, Philipp A, Demuzere M, Ustrnul Z, Cahynová M, et al. Classifications of atmospheric circulation patterns[J].Annals of the New York Academy of Sciences, 2008,1146(1), 105-152.

[22] Objective Analysis on Large-scale Circulation Type and Its Links to Precipitation over China[J].Advances in Earth Science,2018,33(4):396-403.(in Chinese)

[23] Yang Xu, Zhang Xiaoling, Kang Yanzhen, et al. Circulation weather type classification for air pollution over the Beijing-Tianjin-Hebei region during winter[J].China Environmental Science, 2017,37(9):3021-3209.

[24] Gao Y, Liu X, Zhao C, Zhang M. Emission controls versus meteorological conditions in determining aerosol concentrations in Beijing during the 2008 Olympic Games [J]. Atmos. Chem. Phys.,2011,11:12437-12451.

[25] Zhang Y, Ding A, Mao H, Nie W, Zhou D, Liu L, et al. Impact of synoptic weather patterns and inter-decadal climate variability on air quality in the North China Plain during 1980-2013[J].Atmospheric Environment,2016,124:119-128.

[26] Zhang Q, Streets D G, He K, et al. NOx emission trends for China, 1995-2004: The view from the ground and the view from space[J]. Journal of Geophysical Research:Atmospheres, 2007, 112(LF2).

[27] Ashrafi K, Shafie M, Kamalan H. Estimating temporal and seasonal variation of ventilation coefficients[J]. International Journal of Environmental Research, 2010,3(4):637-644.

[28] Lei Y, Zhang Q, He K, et al. Primary anthropogenic aerosol emission trends for China,1990-2005[J]. Atmospheric Chemistry Physics, 2011,11(3): 931-954

[29] Ambient air quality standards[S].China: GB 3095-2012

BILINGUAL PUBLISHING CO.
Pioneer of Global Academics Since 1984

Journal of Atmospheric Science Research
https://ojs.bilpublishing.com/index.php/jasr

ARTICLE

Effect of Varying Aerosol Concentrations and Relative Humidity on Visibility and Particle Size Distribution in Urban Atmosphere

Ummulkhair Abdulkarim[1*] **Bello Tijjani**[2]

1. Department of Physics, Sa'adatu Rimi College of Education Kano, P. M. B. 3218, Kano State, Nigeria
2. Department of Physics, Bayero University Kano, P.M.B. 3011, Kano State, Nigeria

ARTICLE INFO

Article history
Received: 4 July 2021
Accepted: 28 July 2021
Published Online: 12 August 2021

Keywords:
Aerosol concentration
Humidification factor
Hygroscopic growth
Particle size distribution
Visibility enhancement

ABSTRACT

Atmospheric aerosol concentrations have been found to change constantly due to the influence of source, winds and human activities over short time periods. This has proved to be a constraint to the study of varied aerosol concentrations in urban atmosphere alongside changing relative humidity and how it affects visibility and aerosol particle size distribution. In this research simulation was carried out using Optical Properties of Aerosols and Clouds (OPAC 4.0) average concentration setup for relative humidity (RH) 0-99% at visible wavelength 0.4-0.8 μm to vary the concentrations of three aerosol components: WASO (Water-soluble), INSO (Insoluble) and SOOT. The Angstrom exponents (α), the curvatures (α_2) and atmospheric turbidities (β) were obtained from the regression analysis of Kaufman's first and second order polynomial equations for visibility. The research determined the mean exponent of the aerosol size growth curve (μ) from the effective hygroscopic growth (g_{eff}) and the humidification factors (γ) from visibility enhancement f (RH, λ). The mean exponent of aerosol size distributions (υ) was determined from μ and γ. The results showed that with varied WASO, INSO and SOOT concentrations respectively at different RH, aerosol particle size distributions showed bimodal characteristics with dominance of fine mode particles. Hazy atmospheric conditions prevailed with increasing turbidity.

1. Introduction

The farthest distance at which any object can be seen with unaided human eyes is termed atmospheric visibility [1]. With rapid development and industrialization, poor and degrading visibility has become one of the most worrisome urban atmospheric environmental problems [2-6]. This is due to the increase in energy consumption that has led to more frequent air pollution all over the world [7-10]. Bad visibility is caused by the scattering and absorption of visible light by gaseous pollutants and fine suspended particles known as aerosols in the atmosphere. Because of their differences in chemical and physical components, aerosol particles have the ability to absorb more water compared to their dry state as atmospheric moisture increases. This changes their optical properties as they increase in size [11]. Aerosols within urban atmosphere can be composed of water-soluble aerosols from industrial emissions, insoluble and soot from biomass and bio-fuel emissions respectively [3]. Emissions from human activities such as vehicular emissions are the major source of pollution and aerosols. Biomass burning and dust

---

**Corresponding Author:*
Ummulkhair Abdulkarim,
Department of Physics, Sa'adatu Rimi College of Education Kano, P. M. B. 3218, Kano State, Nigeria;
Email: gjummu.physicist@yahoo.com

DOI: https://doi.org/10.30564/jasr.v4i3.3430

transported from dry desert areas surrounding an urban atmosphere [4] and nearby regions can also contribute to aerosol characteristics which alter their optical properties [3]. Often, aerosols undergo coagulation and become mixed internally and component-wise, [10] even the presence of water soluble aerosols wrapped around insoluble aerosol cores can encourage hygroscopic properties [11-14].

Investigations have been carried out by many studies using laboratory generated aerosols to understand how water soluble and insoluble aerosols respond to atmospheric moisture. These experimental methods investigated the effects of relative humidity on the ability of aerosols to scatter visible light and how these scattering effects are applicable to an urban atmosphere [12-18]. Aerosols are very diverse and constantly changing in their form, shape, size and concentrations globally, this makes them difficult to study. Their constant changing nature also causes gaps in their coverage through time and space and these cause biases in data when collecting ground and satellite data. Most studies just focus on short time periods and although long-term investigations of aerosol optical properties are important, they are rarely reported in literature [19]. Because of unavoidable gaps and biases in data, the data collected with satellite, in-situ and ground-based instruments could not be sufficient for a direct local assessment of the long-term aerosol effect in urban atmosphere [20]. Furthermore, more data and detailed studies on how aerosol mixing and varied concentration can affect aerosol hygroscopic growth is needed [21], because present available data does not allow for the varying of atmospheric aerosol concentrations, the use of model methods and simulations is imperative.

In this research, aerosol concentrations of water-soluble (WASO), Insoluble (INSO) and SOOT were varied through external mixing to analyze the effect of relative humidity (RH) and varying aerosol concentrations on visibility and particle size distribution in urban atmosphere. From the extinction coefficients extracted, visibilities and visibility enhancement factors were determined and effective hygroscopic growth were also determined using aerosol particle radii.

2. Theoretical Framework

Visibility calculations are carried out based on the Koschmieder formula using extracted extinction coefficients for particular relative humidity at corresponding visible spectral wavelength [12].

$$V_{Vis}(\lambda) = \frac{3.912}{\sigma_{ext}(\lambda)} \tag{1}$$

But extinction coefficient is defined in terms of wavelength using the inverse power law as [22];

$$\sigma_{ext}(\lambda) = \beta\lambda^{-\alpha} \tag{2}$$

$$V_{Vis}(\lambda) = \frac{3.912}{\beta}\lambda^{\alpha} \tag{3}$$

Such that [23] Equation (1) and Equation (2) give the expression in Equation (4);

$$\ln\left(\frac{V_{Vis}(\lambda)}{3.912}\right) = \alpha\ln(\lambda) - \ln(\beta) \tag{4}$$

Performing a regression analysis on Kasten's (1969) representation of Equation (1) gives α (Angstrom exponent) and β (turbidity) [12,24]. An empirical relationship between visibility and wavelength can then be obtained with a 2nd-order polynomial [25-27].

$$\ln\left(\frac{V_{Vis}(\lambda)}{3.912}\right) = \alpha_1\left(\ln(\lambda)\right) + \alpha_2\left(\ln(\lambda)\right)^2 - \ln(\beta) \tag{5}$$

Where α_2 indicates aerosol particle size [28], $-\alpha_2$ means fine mode particle dominance and $+\alpha_2$ coarse mode particle dominance [24,29].

The Visibility Enhancement which gives the relationship between visibility and relative humidity is presented in Equation (6) [30-31].

$$f(RH,\lambda) = \frac{V_{Vis}(RH,\lambda)}{V_{Vis}(RH_0,\lambda)} = \left[\frac{1-RH}{1-(RH_0)}\right]^{-\gamma} \tag{6}$$

To be considered for regression analysis Equation (6) takes the form;

$$ln\left(\frac{V_{Vis}(RH,\lambda)}{V_{Vis}(RH_0,\lambda)}\right) = -\gamma ln(1-RH) \tag{7}$$

Where RH_0=0% and $V_{Vis}(RH, \lambda)$ is the visibility at wavelength λ at any given relative humidity (RH). γ can be expressed as [27];

$$\mu\gamma = v - 1 \tag{8}$$

Where γ shows the dependence of visibility on relative humidity (RH) resulting from the change in the particle size of the aerosol particles upon humidification [32]. μ is the mean exponent aerosol growth curve [33] while υ is the mean exponent aerosol size distribution presented in the Junge power law size distribution function;

$$\frac{dn(r)}{d(logr)} = cr^{-\upsilon} \tag{9}$$

with c as a constant and $dn(r)$ representing number of particles with radii between r and $r + dr$ [33].

The hygroscopic growth $g(RH)$ experienced by a single particle according to [34] is given by;

$$g(RH) = \frac{r(RH)}{r(RH_0)} \tag{10}$$

with $r(RH)$ being the radius at a given relative humidity RH and $r(RH_0)$ representing the radius at 0% relative humidity. For different aerosols of different components Equation (10) takes the form of Equation (11) which is the effective hygroscopic growth of the whole aerosol population;

DOI: https://doi.org/10.30564/jasr.v4i3.3430

$$g_{eff}(RH) = \left(\sum_k x_k g_k^3(RH)\right)^{\frac{1}{3}} \tag{11}$$

where x_k is the volume mix ratio of the kth term and g_k is the hygroscopic growth of the kth component [32]. The relationship between effective growth and relative humidity (RH) is expressed as [34];

$$g_{eff}(RH) = \left[\frac{1-(RH)}{1-(RH_0)}\right]^{-\frac{1}{\mu}} \tag{12}$$

where μ is the mean exponent of the aerosol growth curve as defined in Equation (8). Equation (12) can be written as Equation (13) for regression analysis purposes;

$$lng_{eff}(RH) = -\frac{1}{\mu}ln(1-RH) \tag{13}$$

Using Equation (8), the mean exponent of the aerosol size distribution (υ) can be expressed Equation (14) in terms of μ and γ.

$$\upsilon = \mu\gamma + 1 \tag{14}$$

3. Method

3.1 OPAC Implementation

The method employed in this research is a simulation carried out using the software package Optical Properties of Aerosols and Clouds (OPAC 4.0). The first part of OPAC is a dataset of microphysical properties which gives results on aerosol components at different wavelengths for different relative humidities. FORTRAN is the second part of the program from which the user can extract data from the above mentioned datasets for calculation of optical properties of mixtures of stored aerosol components. This work used three aerosol components representing the urban environment and varied the components to obtain five models each. The three components considered were WASO (water-soluble), INSO (insoluble) and SOOT.

To vary component mixtures for WASO, selection was made for component number density such that WASO aerosol concentration is varied at constant INSO and SOOT aerosol concentration. For INSO, selection was made for component number density such that INSO aerosol concentration is varied at constant WASO and SOOT aerosol concentration while for SOOT, selection was made for component number density such that SOOT aerosol concentration is varied at constant INSO and WASO aerosol concentrations. The input for height profile designated for urban aerosols was selected to give the aerosol mixing layer (layer above ground and Top of atmosphere) for the distribution of aerosol particles with height as suggested by Hess, Koepke and Schult (1998) [35]. Only wavelengths belonging to aerosols at the visible spectral range were considered at eight relative humidities. The optical parameters of extinction coefficients, scattering coefficients and absorption coefficients were extracted.

3.2 Data Analysis

The extracted data from the OPAC simulation output files were used in the evaluation of the Angstrom coefficient (α), Curvature (α_2), Turbidity (β), Mean exponent hygroscopic growth curve (μ), Mean exponent aerosol size distribution (υ) and Humidification factor (γ). Equation 1 was used for visibility calculations while a regression analysis was performed on Equation 4 to obtain α and β. From the regression analysis of the second order of the Kaufman's representation of the Koschmeider equation for atmospheric visibility (Equation 5), α_2 is obtained. γ and μ calculations are carried out using the inverse power law from Equation 6 and Equation 12 respectively while calculations for υ are carried out using Equation 7, Equation 13 and Equation 14.

4. Results and Discussions

In the simulation carried out, to vary component mixture concentrations, selection was made for number density such that for the WASO (water soluble) component mixture, number density takes values from 28,000.00 cm^3 to 29,000.00 cm^3 through 200.00 cm^3 increment at constant INSO and SOOT aerosol concentrations of 1.50 cm^3 and 130,000.00 cm^3 respectively. INSO aerosol number density had input values from 1.50 cm^3 to 2.30 cm^3 through 0.20 cm^3 increment at constant WASO and SOOT aerosol concentrations of 28,000.00 cm^3 and 130,000.00 cm^3 respectively. SOOT aerosol number density however, had input values from 130,000.00 cm^3 to 140,000.00 cm^3 through 2,000 cm^3 increment at constant WASO and INSO aerosol concentrations of 1.50 cm^3 and 28,000.00 cm^3 respectively. For the distribution of aerosol particles with height, the height profile designated for urban aerosols as suggested by Hess (1998) was selected to give the aerosol mixing layer with $\mathrm{H_{min}} = 2Km$ (layer above ground), $\mathrm{H_{max}} = 10\ \mathrm{Km}$ (top of atmosphere) and $\mathrm{Z} = 8\ \mathrm{Km}$ (aerosol scale height). Only wavelengths belonging to aerosols were selected and these wavelengths were of the visible spectral wavelength of 0.4 µm to 0.8 µm at eight relative humidities (0%, 50%, 70%, 80%, 90%, 95%, 98% and 99% RH). The maximum radius for mass calculation used was 7.5 µm radius (only particles up to 7.5 µm radius were considered). In this work, the Visibility Enhancement $f\,(RH, \lambda)$, analyzed at λ = 0.55 µm, λ = 0.65 µm and λ = 0.75 µm.

DOI: https://doi.org/10.30564/jasr.v4i3.3430

4.1 Water-Soluble (WASO) Particle Concentration

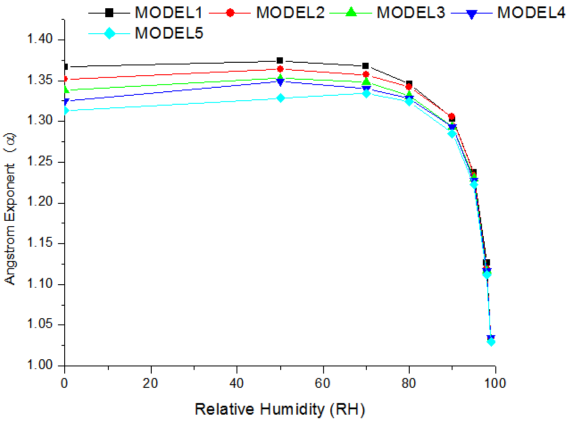

Figure 1. Graph of Angstrom Exponent (α) against Relative Humidity (RH) for five WASO Models

From Figure 1 at 0% RH there is a very noticeable difference between α values of the five models. The values of α decrease from Model 1 to Model 5 such that with increasing WASO concentrations, there is an increase in fine mode particle distribution. α for each model is constant from 0-50% RH and then decreases from 50-100% RH. This indicates sedimentation of heavier particles from 50-99% RH and saturation at 100% RH.

Table 1. Visibility analysis (Model 1- WASO)

	Linear			Quadratic			
RH	R^2	α	β	R^2	α_1	α_2	β
0%	0.99904	1.36649	0.08552	0.99994	1.59994	0.20704	0.08091
50%	0.99835	1.37425	0.11476	0.99994	1.67971	0.27090	0.10673
70%	0.99835	1.36823	0.13385	0.99994	1.71846	0.31060	0.12317
80%	0.99835	1.34585	0.15620	0.99994	1.66395	0.28211	0.14484
90%	0.99835	1.30340	0.21248	0.99994	1.66099	0.31713	0.19519
95%	0.99641	1.23764	0.30775	0.99994	1.66011	0.37467	0.27840
98%	0.99641	1.12685	0.52057	0.99994	1.55508	0.37978	0.47027
99%	0.99405	1.03234	0.74748	0.99994	1.48430	0.40082	0.67146

From Table 1 Model 1, R^2 values fit the equation models. From the linear part, the values of α are greater than 1. This shows that the aerosols are fine mode particles. There is an increase in α value from 0-50% relative humidity and this is due to coagulation of particles at the onset of water uptake, these particles later drop from the atmosphere when they become too heavy. α values decrease from 50-99% relative humidity, this implies hygroscopic growth in aerosol particles and an increase in particle size distribution. From the quadratic part, α_2 is positive which indicates a bimodal distribution and dominance of fine mode particles. The Turbidity (β) is seen to increase from 0-99% relative humidity which indicates hazy atmospheric conditions and deterioration in visibility as relative humidity increases.

The variations in α, α_2 and β in Models 2, 3, 4 and 5 are similar to those of Model 1 from Table 1 as seen from Appendix A Table 1, 3, 5, and 7 respectively.

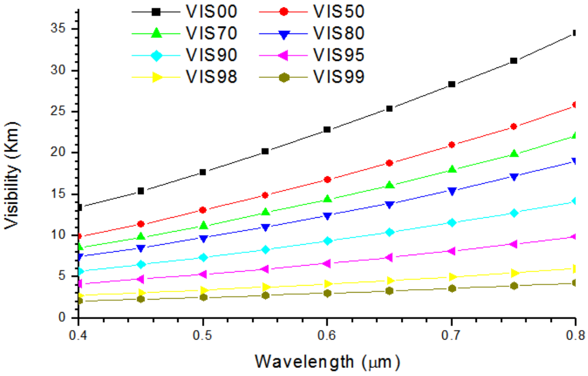

Figure 2. Visibility against Wavelength for WASO

From Figure 2, it can be seen that the visibility decreases with the increase in RH but increases with the increase in wavelength. There is a more noticeable decrease in visibility with increase in relative humidity (RH) from 0% (RH) to 50% (RH) due to the onset of the intake of water by fine mode aerosol particles.

Table 2. Size Distribution and Hygroscopic Growth analysis (Model 1-WASO)

			μ=5.12521
λ	R^2	γ	v
0.55	0.998	0.416	3.135338
0.65	0.997	0.424	3.176105
0.75	0.997	0.430	3.205313

From Table 2 Model 1, R^2 values fit the equation models. The Visibility Enhancement $f(RH,\lambda)$ has satisfied the inverse power law. The increase in humidification factor (γ) and the mean aerosol particle size distribution (v) with wavelength implies that the number of larger particles increases compared to the number of smaller particles at longer wavelengths and smaller particles have more effect in decreasing visibility at shorter wavelengths. The values of $v > 3$ imply typical hazy atmospheric conditions (Junge 1958).

The variations in the humidification factor (γ) and the mean aerosol particle size distribution (v) of Models 2, 3, 4 and 5 are similar to those of Model 1 from Table 2 as seen in Appendix A Table 2, 4, 6 and 8 respectively.

The values of the mean exponent hygroscopic growth curve (μ) decreases with an increase in WASO aerosol concentration across the models and this implies an increase in the effective hygroscopic growth (g_{eff}).

DOI: https://doi.org/10.30564/jasr.v4i3.3430

4.2 Insoluble (INSO) Particle Concentration

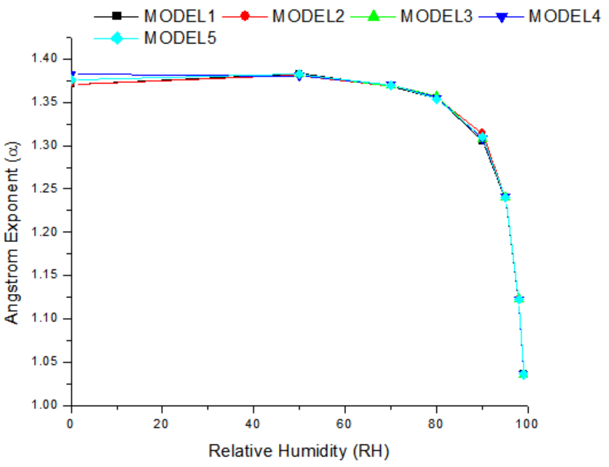

Figure 3. Graph of Angstrom Exponent (α) against Relative Humidity (RH) for five INSO Models

From Figure 3, for the five models, a slight difference is observed between α values as INSO concentration increases. This may be attributed to the dissolution of the outer soluble coating surrounding INSO aerosol particles. At 40-50% RH α values show constant particle size distribution. This particle size distribution decreases form 90-100% RH indicating no hygroscopic growth.

Table 3. Visibility analysis (Model 1-INSO)

	Linear			Quadratic			
RH	R^2	α	β	R^2	α_1	α_2	β
0%	0.99894	1.37041	0.08477	0.99985	1.60567	0.20864	0.08017
50%	0.99827	1.38295	0.11396	0.99985	1.70502	0.28563	0.10557
70%	0.99827	1.36909	0.13380	0.99985	1.71453	0.30636	0.12327
80%	0.99827	1.35505	0.15507	0.99985	1.68279	0.29066	0.14347
90%	0.99749	1.30490	0.21250	0.99985	1.67672	0.32975	0.19455
95%	0.99639	1.23990	0.30787	0.99985	1.66485	0.37687	0.27834
98%	0.99510	1.12185	0.52262	0.99985	1.57011	0.39754	0.46988
99%	0.99398	1.03662	0.74795	0.99985	1.49644	0.40780	0.67064

From Table 3, Model 1 the R^2 values for both the quadratic and linear parts show that R^2 values fit the equation models well. From the linear part, the values of α are greater than 1. This shows that the aerosols are fine mode particles. There is an increase in α value from 0-50% relative humidity and this is due to coagulation of particles at the onset of water uptake by the WASO particles present in the aerosol mixture, these particles later drop from the atmosphere when they become too heavy. α values decrease from 50-99% relative humidity, this implies hygroscopic growth in aerosol particles and an increase in particle size distribution. From the quadratic part, α_2 is positive which indicates a bimodal distribution and dominance of fine mode particles. The Turbidity (β) is seen to increase from 0-99% relative humidity which indicates hazy atmospheric conditions and deterioration in visibility as relative humidity increases.

The variations in α, α_2 and β in Models 2, 3, 4 and 5 are similar to those of Model 1 from Table 3 as seen from Appendix B Table 1, 3, 5, and 7 respectively.

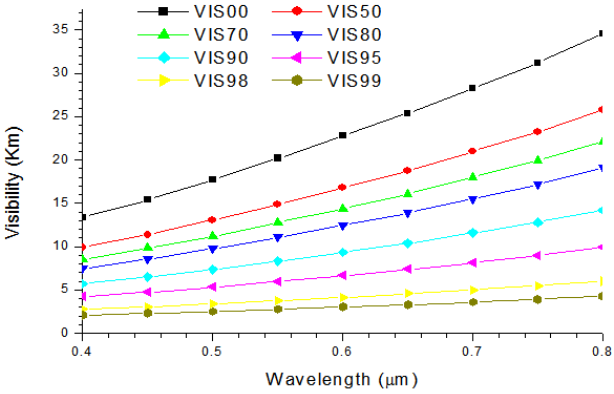

Figure 4. Visibility against Wavelength for INSO

From Figure 4, the visibility decreases with the increase in RH but increases with the increase in wavelength. Visibility is lower at shorter wavelength due to dominance of fine mode aerosol particles.

Table 4. Size Distribution and Hygroscopic Growth analysis (Model 1-INSO)

			μ=5.12735
λ	R^2	γ	v
0.55	0.998	0.409	3.098481
0.65	0.997	0.416	3.130541
0.75	0.996	0.417	3.139715

From Table 4 Model 1, R^2 values fit the equation models very well. The Visibility Enhancement $f(RH,\lambda)$ has satisfied the inverse power law. The increase in humidification factor (γ) and the mean aerosol particle size distribution (v) with wavelength implies that the number of larger particles increases compared to the number of smaller particles at longer wavelengths and smaller particles have more effect in decreasing visibility at shorter wavelengths. The values of $v > 3$ imply typical hazy atmospheric conditions (Junge 1958).

The variations in the humidification factor (γ) and the mean aerosol particle size distribution (v) of Models 2, 3, 4 and 5 are similar to those of Model 1 from Table 4 as seen in Appendix B Table 2, 4, 6 and 8 respectively.

For varying INSO aerosol concentration, the mean

DOI: https://doi.org/10.30564/jasr.v4i3.3430

exponent hygroscopic growth curve (μ) increases with increasing INSO concentration and this implies a decrease in effective hygroscopic growth (g_{eff}).

4.3 SOOT Particle Concentration

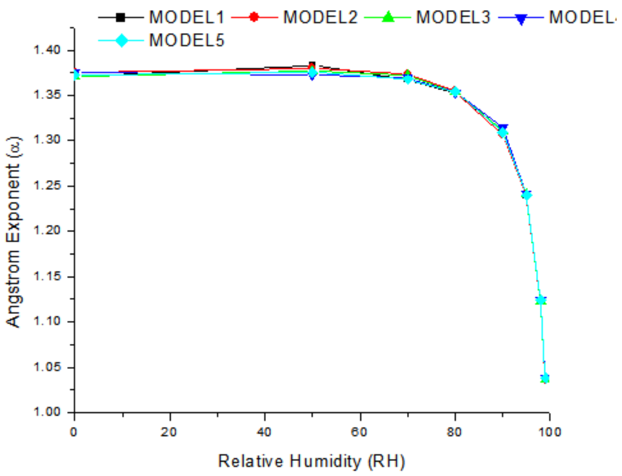

Figure 5. Graph of Angstrom Exponent (α) against Relative Humidity (RH) for five SOOT Models

From Figure 5 constant α values are observed for all models at 0% RH as SOOT concentration increases. For each model, α values show an increase in particle size distribution at 50% RH which may be attributed to the small percentage of insoluble aerosol concentration found within the SOOT aerosol mixture.

Table 5. Visibility analysis (Model 1-SOOT)

	Linear			Quadratic			
RH	R^2	α	β	R^2	α_1	α_2	β
0%	0.99894	1.37041	0.08477	0.99985	1.60567	0.20864	0.08017
50%	0.99894	1.38349	0.11380	0.99985	1.67475	0.25831	0.10620
70%	0.99791	1.36764	0.13388	0.99985	1.71819	0.31089	0.12319
80%	0.99791	1.35324	0.15517	0.99985	1.68392	0.29326	0.14346
90%	0.99706	1.31005	0.21144	0.99985	1.70855	0.35341	0.19237
95%	0.99643	1.23999	0.30716	0.99985	1.66222	0.37446	0.27788
98%	0.99516	1.12366	0.52074	0.99985	1.56992	0.39577	0.46842
99%	0.99392	1.03680	0.74575	0.99985	1.49880	0.40973	0.66832

From Table 5, Model 1 R^2 values fit the equation models very well. From the linear part, the values of α are greater than 1. This shows that the aerosols are fine mode particles. There is an increase in α value from 0-50% relative humidity and this is due to coagulation of water soluble particles present in the mixture particles as they begin to absorb water. α values decrease from 50-99% relative humidity, this implies hygroscopic growth in aerosol particles and an increase in particle size distribution this can be attributed to the hygroscopic properties of the outer soluble coating of the insoluble core combined with the effect of some of the water soluble aerosols found within the mixture. From the quadratic part, α_2 is positive which indicates a bimodal distribution and dominance of fine mode particles. The Turbidity (β) is seen to increase from 0-99% relative humidity which indicates hazy atmospheric conditions and deterioration in visibility as relative humidity increases.

The variations in α, α_2 and β in Models 2, 3, 4 and 5 are similar to those of Model 1 from Table 5 as seen from Appendix C Table 1, 3, 5, and 7 respectively.

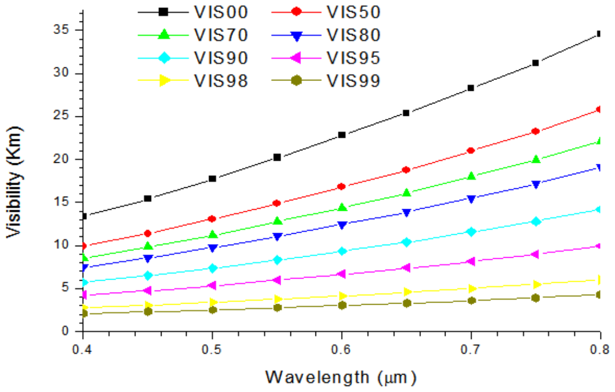

Figure 6. Visibility against Wavelength for SOOT

From Figure 6, the visibility decreases with the increase in RH but increases with the increase in wavelength. Visibility is lower at shorter wavelength due to dominance of soot particles.

Table 6. Size Distribution and Hygroscopic Growth analysis (Model 1-SOOT)

			μ=5.12877
λ	R^2	γ	*v*
0.55	0.998	0.421	3.158174
0.65	0.997	0.429	3.201624
0.75	0.996	0.434	3.226229

From Table 6 Model 1, the values of R^2 show that the data fitted the equation models very well. The Visibility Enhancement $f(RH, \lambda)$ has satisfied the inverse power law. The increase in humidification factor (γ) and the mean aerosol particle size distribution (*v*) with wavelength implies that the number of larger particles increases compared to the number of smaller particles at longer wavelengths and smaller particles have more effect in decreasing visibility at shorter wavelengths. The values of *v* > 3 imply typical hazy atmospheric conditions (Junge 1958).

The variations in the humidification factor (γ) and the mean aerosol particle size distribution (*v*) of Models 2, 3, 4 and 5 are similar to those of Model 1 from Table 6 as seen in Appendix C Table 2, 4, 6 and 8 respectively.

The values of the mean exponent hygroscopic growth curve (μ) increases with increasing SOOT aerosol concentration across the models and this implies a decrease in the effective hygroscopic growth (g_{eff}).

5. Conclusions

From the five model analyses carried out for each component (WASO, INSO and SOOT) respectively, it was concluded that α is greater than 1 which indicates fine mode particles. As WASO concentration increases, α increases and this implies an increase in fine mode particles. α_2 is positive for all models. This shows that the aerosol distribution is bimodal with fine mode particles as dominant. Additionally, it was observed that as the RH and WASO concentration increases, there were fluctuations in the values of α_2 and this may imply a non-linear relationship between the externally mixed aerosols. Similarly, the above conclusions apply for varying INSO and SOOT concentrations respectively. The Turbidity (β) was observed to increase from 0-99% relative humidity which indicated hazy atmospheric conditions and deterioration in visibility as relative humidity increased.

Visibility decreases with an increase in relative humidity and WASO, INSO and SOOT aerosol concentrations across all models respectively. As INSO and WASO aerosol concentrations and relative humidity increased, the hygroscopic or water soluble part of the aerosol mixture were found to be the main contributors in the degradation of visibility.

It was observed that across the models as RH increased (1-RH) decreased. With the increase in WASO concentration, μ decreased this implied that as WASO concentration increased, $^1/_\mu$ increased and g_{eff} increased. The Visibility enhancement decreased as RH increased. The humidification factor (γ) decreased then later increased this maybe due to a non linear relationship between WASO concentration and Visibility enhancement. ν behaved as γ thus this implies that there is also a non linear relationship between the variation in WASO concentration and the change in particle size distribution. As relative humidity increased, g_{eff} increased while μ decreased and as WASO concentration increased, g_{eff} increased while μ decreased. γ decreased and then increased.

With the increase in INSO concentration, μ increased this implied that as INSO concentration increased, $^1/_\mu$ decreased and g_{eff} decreased.The humidification factor (γ) decreased and this implied that increase in INSO concentration reduced absorption of water. υ fluctuates, this implies that there is also a non linear relationship between the variation in INSO concentration and the change in particle size distribution. As relative humidity increased, g_{eff} decreased while μ increased and as INSO concentration increased, g_{eff} decreased while μ increased, γ decreased all through.

With increasing SOOT concentration, g_{eff} decreased as $^1/_\mu$ decreased and the humidification factor (γ) decreases which implies that the increase in SOOT concentration reduced water uptake. ν decreases which implies a decrease in particle size distribution. As relative humidity increased, g_{eff} decreased while μ increased and as SOOT concentration increased, g_{eff} decreased while μ increased, γ decreased all through.

Author Contributions

Both authors named in this work took part in data generation, analysis, result presentation and conclusions.

Conflict of Interest

All authors whose names are indicated in this write-up certify that they have no affiliations or involvement with any organization that has financial or non financial interest in the content of this research.

Funding

This research did not receive any external funding.

Acknowledgements

The authors are grateful to Prof. Usman M. Gana and Prof. Muntari Hajara Ali of the Physics Department Bayero University, Kano, Nigeria for reading this article and forwarding all necessary corrections. The OPAC 4.0 software package used to generate the data for this work is available at http://www.rascin.net/en/opac40.

References

[1] Wu, D., Li, X. X., Ying, C. C., Lau, Z. M., Huang, A. K. H., Deng, J., X. J.,&Bi, X. Y. (2005): An extremely low visibility event over the Guangzhou region: A case study, *Atmos. Environ.,* 39(35), 6568-6577. https://doi.org/10.1016/j.atmosenv.2005.07.061.

[2] Bret, A. S., Rudolf, B. H., Stefan. R. F, & William E.W., (2001). Haze trends over the United States, 1980-1995. *Journal of Atmosphere and Environment.* 35: 5205-5210. https://doi.org/10.1016/S1352-2310(01)00317-X.

[3] Chan, Y.C., Simpson, R.W., Mctainsh, G. H., Vowles, P. D., Cohen D. D.,& Bailey, G. M., (1999). Source Apportionment of Visibility Degradation Problems in Brisbane (Australia) Using the Multiple Linear

Regression Techniques. *Journal of Atmosphere and Environment*. 33: 3237-3250. https://doi.org/10.1016/S1352-2310(99)00091-6.

[4] Doylem, M. & Dorling S., (2002). Visibility Trends in the UK 1950-1997. *Journal of Atmosphere and Environment*. 36: 3163-3172. https://doi.org/10.1016/S1352-2310(02)00248-0.

[5] Kotchenruther, R. A., Hobbs, P.V., Hegg, D. A., (1999). Humidification factors for atmospheric aerosol off the midAtlantic coast of United States. *J. Geophys. Res.* 104 (D2), 2239-2251. https://doi.org/10.1029/98JD01751.

[6] Yoon, S.C., Kim, J., (2006). Influences of relative humidity on aerosol optical properties and aerosol radiative forcing during ACE-Asia. *Atmos. Environ.* 40 (23), 4328-4338 https://doi.org/10.1016/j.atmosenv.2006.03.036.

[7] Chan, C. K., & Yao, X. H., (2008): Air pollution in mega cities in China, Atmos. Environ., 42, 1-42. https://doi.org/10.1016/j.atmosenv.2007.09.003.

[8] Deng, X. J., Tie X. X., Wu, D., Zhou, X. J., Bi, X.Y., Tan H. B., Li F., & Jiang C. L., (2008): Long- Term Trend of Visibility and Its Characterizations in the Pearl River Delta (PRD) Region, China. *Journal of Atmosphere and Environment* .42(7), 1424-1435. https://doi.org/10.1016/j.atmosenv.2007.11.025.

[9] Massoli, P., Bates, T. S., Quinn, P.K., Lack, D.A., Baynard, T., Lerner, B.M., TuckerS.C.,,Brioude, J., Stohl, A., Williams, E.J., (2009). Aerosol optical and hygroscopic properties during TexAQS-GoMACCS 2006 and their impact on aerosol direct radiative forcing. *J. Geophys. Res.* 114, D00F07. https://doi.org/10.1029/2008JD011604.

[10] Tijjani B. I. (2013). The Effect of Soot and Water Soluble on the Hygroscopicity of Urban Aerosols. *Advances in Physics Theories and Applications*. www.iiste.org ISSN 2224-719X (Paper) ISSN 2225-0638, Vol.26.

[11] Cheng, Y. F., Wiedensohler A., Eichler H., Heintzenberg J., Tesche M., Ansmann A., Wendisch M., Su H.,Althausen D.,HerrmannH., Gnauk T., Bruggemann E., Hu M., Zhang Y.H., (2008). Relative Humidity Dependence of Aerosol Optical Properties and Direct Radiative Forcing in The Surface Boundary Layer at Xinken in Pearl River Delta of China: An Observation Based Numerical Study. *Journal of Atmosphere and Environment*. 42, 6373-6397. https://doi.org/10.1016/j.atmosenv.2008.04.009.

[12] Koschmieder, H., (1972): Theorie der horizontalen-Sichtweite, BeiträgezurPhysik der freienAtmosphäre, Meteorol. Z., 12, 33-55.

[13] Liu et al. X. (2012). 'Aerosol Hygroscopicity and Its Impact on Atmospheric Visibility and Radiative Forcing in Guangzhou during the 2006 PRIDE-PRD Campaign'. *Atmospheric Environment* 60: 59-67. https://doi.org/10.1016/j.atmosenv.2012.06.016.

[14] Liu, X.G., Zhang, Y.H., Jung, J.S., Gu, J.W., Li, Y.P., Guo, S., Chang, S.Y., Yue, D., Lin, P., Kim, Y.J., Hu, M., Zeng, L.M.,Zhu, T., (2009). Research on aerosol hygroscopic properties by measurement and model during the 2006 CARE Beijing campaign.*J. Geophys. Res.* 114, D00G16.

[15] Liu, X.G., Zhang, Y.H., Wen, M.T., Wang, J.L., Jung, J.S., Chang, S.Y., Hu, M., Zeng, L.M., Kim, Y.J., (2010).A closure study of aerosol hygroscopic growth factor during the 2006 PRD campaign. *Adv. Atmos. Sci.*.

[16] Reid, J.S., Jayaraman, A., Kiehl, J.T., Krishnamurti, T.N.&Lubin, D. (1999). Physical, chemical and optical regional hazes dominated by smoke in Brazil. *Journal of Geophysical Research,* 103: 32059-32080. https://doi.org/10.1029/98JD00458.

[17] Sjogren, S. et al. (2007). 'Hygroscopic Growth and Water Uptake Kinetics of Two-Phase Aerosol Particles Consisting of Ammonium Sulfate , Adipic and Humic Acid Mixtures'. 38: 157-71.

[18] Tijjani, B. I. Aliyu, A. & Shaaibu F. (2014b). 'The Effect of Relative Humidity on Continental Average Aerosols'. *Open Journal of Applied Sciences*, 4, 399-423 (6) 10.4236/ojapps.2014.47038.

[19] King, M.& Byrne, D. (1976). A method for inferring total ozone content from the spectral variation of total optical depth obtained with a solar radiometer. *Journal of Geophysical Research*, 33: 3251-3254. https://doi.org/10.1175/1520-0469(1976)033<2242:AMFITO>2.0.CO;2.

[20] Yuan, C. S., Lee, C. G, Chang J. C. & Yuan C. (2005) Effects of Aerosol Species on Atmospheric Visibility in Kaohsiung City, Taiwan. *Journal of Air & Waste Management Association.*55:1031-1041 https://doi.org/10.1080/10473289.2005.10464683.

[21] Kim, Jiyoung, Soon-chang Yoon, Anne Jefferson, and Sang-woo Kim. (2006). 'Aerosol Hygroscopic Properties during Asian Dust, Pollution , and Biomass Burning Episodes at Gosan , Korea in April 2001. Atmos. Environ., 40, 1550-1560.

[22] Ångström A. (1961). Techniques of Determining the Turbidity. Tellus, 13(2): 214-223. https://doi.org/10.3402/tellusa.v13i2.9493.

[23] Galadanci, G.S.M., Tijjani, B.I., Abubakar, A.I., Koki, F. S., Adamu, I. D., Nura, A. M., Saleh, M.,&Uba, S. (2015): The Effect of Kelvin Effect On

The Equilibrium Effective Radii And Hygroscopic Growth of Atmospheric Aerosols. IISTE- *Journal of Natural Sciences Research,* Vol.5, No.22, 2015 p96-111. https://core.ac.uk/download/pdf/234656185.pdf.

[24] Kasten F. (1969). Visibility forecast in the phase of pre-condensation. *Tellus*, XXI, 5, 631-635. https://doi.org/10.1111/j.2153-3490.1969.tb00469.x.

[25] Kaufman Y. (1993). Aerosol optical thickness and path radiance.*Journal of Geophysical research* 98 (D2) 2677-2692. https://doi.org/10.1029/92JD02427.

[26] Tang, I.N., Munkelwitz, H.R., (1994). Water activities, densities, and refractive indices of aqueous sulfate and sodium nitrate droplets of atmospheric importance.*J. Geophys. Res.* 99 (D9), 18,801-18,808. https://doi.org/10.1029/94JD01345.

[27] Tijjani, B. I., Sha'aibu F.&Aliyu. A. (2014a).The Effect of Relative Humidity on Maritime Polluted Aerosols.*International Journal of Pure and Applied Physics* Vol.2, No.1, Pp.9-36.

[28] Eck, T. F., Holben, B. N., Ward,D. E., Dubovic, R. J. S., Smirnov, A., Mukelabai M. M., Hsu, N. C., O' Neil N. T.,&Slutsker I. (2001) Characterization of The Optical Properties of Biomass Burning Aerosols in Zambia During the 1997 ZIBBEE Field Campaign, *Journal of Geophysics Research,* 106(D4), 3425-3448. https://doi.org/10.1029/2000JD900555.

[29] Moln´ar, A., M´esz´aros, E., Imre, K., &R¨ull, A. (2008): Trends in visibility over Hungary between 1996 and 2002, Atmos. Environ., 42, 2621-2629. https://doi.org/10.1016/j.atmosenv.2007.05.012.

[30] Frankenberger, E. (1967) Beitr. Phys. Atmos. 37, 183.

[31] Zieger, P., Fierz-Schmidhauser,R., Poulain, L., Müller, T., Birmili, W., Spindler, G., Wiedensohler, A.,Baltensperger, U., &Weingartner, E. (2013): Effects of relative humidity on aerosol light scattering: results from different European sites, Atmos. Chem. Phys., 13, 10609-10631. https://doi.org/10.5194/acp-13-10609-2013.

[32] Quinn, P. K.,et al. (2005) , Impact of particulate organic matter on the relative humidity dependence of light scattering: A simplified parameterization, Geophys. Res. Lett., 32, L22809,. https://doi.org/10.1029/2005GL024322.

[33] Junge, C. E. (1958). Atmospheric Chemistry. Advances in geophysics (Vol. 4, pp 1-108). Elsevier. https://doi.org/10.1016/S0065-2687(08)60484-7.

[34] TangI. N. (1996).Chemical and size effects of hygroscopic aerosols on light scattering coefficients. *Journal of Geophysical Research* 101 (D14), 19,245-19,250 https://doi.org/10.1029/96JD03003.

[35] Hess, M., Koepke, P., and Schult, I. (1998): Optical properties of aerosols and clouds: The software package OPAC, B. Am. Meteor. Soc., 79, 831-844.

Appendix A

Water-Soluble (WASO)

Table 1. Visibility analysis (Model 2- WASO)

	Linear			Quadratic			
RH	R^2	α	β	R^2	α_1	α_2	β
0%	0.99906	1.35151	0.08688	0.99974	1.55343	0.17907	0.08282
50%	0.99906	1.36385	0.11608	0.99974	1.61834	0.22570	0.10928
70%	0.99793	1.35748	0.13548	0.99974	1.70018	0.30393	0.12490
80%	0.99793	1.34193	0.15736	0.99974	1.69715	0.31504	0.14464
90%	0.99722	1.30589	0.21267	0.99974	1.69886	0.34851	0.19373
95%	0.99649	1.23363	0.30933	0.99974	1.65025	0.36949	0.28021
98%	0.99516	1.11938	0.52310	0.99974	1.56387	0.39420	0.47074
99%	0.99392	1.03360	0.74808	0.99974	1.49403	0.40834	0.67065

Table 2. Size Distribution and Hygroscopic Growth analysis (Model 2-WASO)

			μ=5.12299
λ	R^2	γ	v
0.55	0.998	0.416	3.13200
0.65	0.997	0.424	3.17235
0.75	0.996	0.427	3.19177

Table 3. Visibility analysis (Model 3- WASO)

Linear				Quadratic			
RH	R^2	α	β	R^2	α_1	α_2	β
0%	0.99942	1.33858	0.08836	0.99987	1.50106	0.14410	0.08502
50%	0.99847	1.35279	0.11773	0.99987	1.63925	0.25405	0.11000
70%	0.99847	1.34792	0.13705	0.99987	1.65862	0.27555	0.12731
80%	0.99847	1.33113	0.15898	0.99987	1.62521	0.26081	0.14827
90%	0.99747	1.29306	0.21535	0.99987	1.66314	0.32821	0.19725
95%	0.99646	1.23035	0.31083	0.99987	1.64759	0.37003	0.28153
98%	0.99519	1.11688	0.52472	0.99987	1.55909	0.39218	0.47245
99%	0.99408	1.03238	0.74970	0.99987	1.48631	0.40257	0.67314

Table 4. Size Distribution and Hygroscopic Growth analysis (Model 3-WASO)

			μ =5.12079
λ	R^2	γ	v
0.55	0.998	0.414	3.121978
0.65	0.997	0.421	3.160147
0.75	0.996	0.425	3.177426

Table 5. Visibility analysis (Model 4- WASO)

Linear				Quadratic			
RH	R^2	α	β	R^2	α_1	α_2	β
0%	0.99900	1.32447	0.08993	0.99965	1.51808	0.17170	0.08589
50%	0.99850	1.34896	0.11883	0.99965	1.63267	0.25161	0.11109
70%	0.99850	1.34027	0.13852	0.99965	1.65464	0.27880	0.12856
80%	0.99850	1.32827	0.16036	0.99965	1.68449	0.31592	0.14736
90%	0.99728	1.29296	0.21611	0.99965	1.66853	0.33308	0.19768
95%	0.99728	1.22767	0.31207	0.99965	1.63779	0.36371	0.28313
98%	0.99539	1.11634	0.52579	0.99965	1.54599	0.38104	0.47483
99%	0.99373	1.03402	0.75093	0.99965	1.50203	0.41506	0.67200

Table 6. Size Distribution and Hygroscopic Growth analysis (Model 4-WASO)

			μ=5.11871
λ	R^2	γ	v
0.55	0.998	0.412	3.11302
0.65	0.997	0.419	3.148495
0.75	0.996	0.422	3.161708

Table 7. Visibility analysis (Model 5- WASO)

	Linear			Quadratic			
RH	R^2	α	β	R^2	$α_1$	$α_2$	β
0%	0.99939	1.31346	0.09157	0.99982	1.46925	0.13816	0.08825
50%	0.99939	1.32863	0.12111	0.99982	1.57453	0.21808	0.11424
70%	0.99829	1.33482	0.13964	0.99982	1.63901	0.26977	0.12991
80%	0.99829	1.32433	0.16122	0.99982	1.65024	0.28904	0.14922
90%	0.99742	1.28527	0.21799	0.99982	1.65620	0.32897	0.19962
95%	0.99742	1.22247	0.31398	0.99982	1.62767	0.35936	0.28519
98%	0.99518	1.11222	0.52816	0.99982	1.55306	0.39096	0.47570
99%	0.99396	1.02970	0.75276	0.99982	1.48734	0.40587	0.67530

Table 8. Size Distribution and Hygroscopic Growth analysis (Model 5-WASO)

			μ= 5.11657
λ	R^2	γ	v
0.55	0.998	0.410	3.10370
0.65	0.997	0.416	3.130541
0.75	0.996	0.419	3.147515

Appendix B

Insoluble (INSO)

Table 1. Visibility analysis (Model 2- INSO)

	Linear			Quadratic			
RH	R^2	α	β	R^2	$α_1$	$α_2$	β
0%	0.99902	1.37058	0.08533	0.99985	1.59501	0.19904	0.08091
50%	0.99842	1.38126	0.11463	0.99985	1.68550	0.26982	0.10665
70%	0.99871	1.36932	0.13408	0.99985	1.64651	0.24583	0.12555
80%	0.99751	1.35485	0.15626	0.99985	1.73701	0.33893	0.14272
90%	0.99712	1.31448	0.21223	0.99985	1.71683	0.35683	0.19291
95%	0.99635	1.24052	0.30969	0.99985	1.66775	0.37889	0.27983
98%	0.99518	1.12282	0.52574	0.99985	1.56806	0.39487	0.47302
99%	0.99388	1.03637	0.75302	0.99985	1.49985	0.41104	0.67460

Table 2. Size Distribution and Hygroscopic Growth analysis (Model 2-INSO)

			μ=5.15606
λ	R^2	γ	v
0.55	0.998	0.418	3.144787
0.65	0.997	0.427	3.189630
0.75	0.996	0.431	3.211264

DOI: https://doi.org/10.30564/jasr.v4i3.3430

Table 3. Visibility analysis (Model 3- INSO)

	Linear			Quadratic			
RH	R^2	α	β	R^2	α_1	α_2	β
0%	0.99894	1.37596	0.08528	0.99996	1.62793	0.22346	0.08033
50%	0.99847	1.38263	0.11498	0.99996	1.67868	0.26255	0.10718
70%	0.99847	1.36909	0.13515	0.99996	1.71453	0.30636	0.12451
80%	0.99847	1.35685	0.15653	0.99996	1.68166	0.28806	0.14492
90%	0.99743	1.30791	0.21453	0.99996	1.68537	0.33475	0.19615
95%	0.99638	1.24005	0.31167	0.99996	1.66513	0.37699	0.28177
98%	0.99520	1.12275	0.52927	0.99996	1.56688	0.39388	0.47633
99%	0.99387	1.03626	0.75816	0.99996	1.49990	0.41118	0.67917

Table 4. Size Distribution and Hygroscopic Growth analysis (Model 3-INSO)

			$\mu=5.18455$
λ	R^2	γ	v
0.55	0.998	0.419	3.150005
0.65	0.997	0.427	3.191274
0.75	0.996	0.432	3.216909

Table 5. Visibility analysis (Model 4- INSO)

	Linear			Quadratic			
RH	R^2	α	β	R^2	α_1	α_2	β
0%	0.99908	1.38252	0.08526	0.99978	1.59173	0.18554	0.08113
50%	0.99836	1.38041	0.11583	0.99978	1.68943	0.27406	0.10764
70%	0.99871	1.36991	0.13540	0.99978	1.64678	0.24554	0.12679
80%	0.99748	1.35520	0.15782	0.99978	1.73955	0.34086	0.14406
90%	0.99748	1.30839	0.21576	0.99978	1.70144	0.34858	0.19655
95%	0.99635	1.24049	0.31351	0.99978	1.66727	0.37849	0.28332
98%	0.99513	1.12283	0.53251	0.99978	1.57072	0.39722	0.47882
99%	0.99392	1.03570	0.76325	0.99978	1.49707	0.40917	0.68410

Table 6. Size Distribution and Hygroscopic Growth analysis (Model 4-INSO)

			$\mu=5.21256$
λ	R^2	γ	v
0.55	0.998	0.420	3.153959
0.65	0.997	0.428	3.196834
0.75	0.997	0.433	3.220585

Table 7. Visibility analysis (Model 5- INSO)

Linear				Quadratic			
RH	R^2	α	β	R^2	α_1	α_2	β
0%	0.99894	1.37596	0.08613	0.99996	1.62793	0.22346	0.08114
50%	0.99847	1.38263	0.11614	0.99996	1.67868	0.26255	0.10826
70%	0.99847	1.36968	0.13648	0.99996	1.71480	0.30607	0.12575
80%	0.99847	1.35406	0.15855	0.99996	1.68115	0.29008	0.14671
90%	0.99730	1.30987	0.21665	0.99996	1.69804	0.34425	0.19758
95%	0.99640	1.24022	0.31541	0.99996	1.66435	0.37614	0.28521
98%	0.99499	1.12263	0.53612	0.99996	1.57614	0.40220	0.48142
99%	0.99390	1.03612	0.76813	0.99996	1.49871	0.41025	0.68828

Table 8. Size Distribution and Hygroscopic Growth analysis (Model 5-INSO)

			μ=5.24028
λ	R^2	γ	v
0.55	0.998	0.420	3.155501
0.65	0.997	0.429	3.200019
0.75	0.997	0.433	3.222553

Appendix C

SOOT

Table 1. Visibility analysis (Model 2- SOOT)

Linear				Quadratic			
RH	R^2	α	β	R^2	α_1	α_2	β
0%	0.99894	1.37596	0.08528	0.99996	1.62793	0.22346	0.08033
50%	0.99836	1.38041	0.11467	0.99996	1.68943	0.27406	0.10657
70%	0.99836	1.37343	0.13358	0.99996	1.70354	0.29277	0.12352
80%	0.99836	1.35501	0.15537	0.99996	1.68395	0.29173	0.14370
90%	0.99836	1.30612	0.21243	0.99996	1.67494	0.32709	0.19463
95%	0.99646	1.24013	0.30772	0.99996	1.66073	0.37301	0.27849
98%	0.99514	1.12342	0.52133	0.99996	1.57068	0.39666	0.46883
99%	0.99397	1.03585	0.74650	0.99996	1.49549	0.40764	0.66936

Table 2. Size Distribution and Hygroscopic Growth analysis (Model 2-SOOT)

			μ=5.13031
λ	R^2	γ	v
0.55	0.998	0.416	3.135338
0.65	0.997	0.425	3.178341
0.75	0.996	0.429	3.198118

DOI: https://doi.org/10.30564/jasr.v4i3.3430

Table 3. Visibility analysis (Model 3- SOOT)

	Linear			Quadratic			
RH	R^2	α	β	R^2	α_1	α_2	β
0%	0.99937	1.37151	0.08596	0.99985	1.54290	0.15200	0.08253
50%	0.99937	1.37682	0.11507	0.99985	1.62401	0.21922	0.10852
70%	0.99811	1.37223	0.13422	0.99985	1.70665	0.29658	0.12398
80%	0.99811	1.35425	0.15630	0.99985	1.73675	0.33922	0.14273
90%	0.99737	1.31072	0.21228	0.99985	1.69411	0.34001	0.19382
95%	0.99644	1.24092	0.30806	0.99985	1.66315	0.37446	0.27869
98%	0.99515	1.12343	0.52184	0.99985	1.57038	0.39638	0.46933
99%	0.99408	1.03748	0.74654	0.99985	1.49361	0.40453	0.66996

Table 4. Size Distribution and Hygroscopic Growth analysis (Model 3-SOOT)

			μ=5.13170
λ	R^2	γ	*v*
0.55	0.998	0.415	3.125654
0.65	0.997	0.424	3.172354
0.75	0.996	0.428	3.195594

Table 5. Visibility analysis (Model 4- SOOT)

	Linear			Quadratic			
RH	R^2	α	β	R^2	α_1	α_2	β
0%	0.99894	1.37596	0.08613	0.99996	1.62793	0.22346	0.08114
50%	0.99823	1.37277	0.11614	0.99996	1.69462	0.28544	0.10760
70%	0.99823	1.36909	0.13515	0.99996	1.71453	0.30636	0.12451
80%	0.99823	1.35324	0.15673	0.99996	1.68392	0.29326	0.14490
90%	0.99724	1.31463	0.21215	0.99996	1.70860	0.34939	0.19321
95%	0.99648	1.24101	0.30859	0.99996	1.66052	0.37205	0.27935
98%	0.99521	1.12462	0.52215	0.99996	1.56895	0.39406	0.46990
99%	0.99410	1.03813	0.74689	0.99996	1.49388	0.40419	0.67033

Table 6. Size Distribution and Hygroscopic Growth analysis (Model 4-SOOT)

			μ=5.13321
λ	R^2	γ	*v*
0.55	0.998	0.414	3.122768
0.65	0.997	0.422	3.163033
0.75	0.997	0.427	3.188241

Table 7. Visibility analysis (Model 5- SOOT)

Linear				Quadratic			
RH	R^2	α	β	R^2	α_1	α_2	β
0%	0.99917	1.37292	0.08685	0.99985	1.57617	0.18025	0.08276
50%	0.99917	1.37596	0.11627	0.99985	1.62793	0.22346	0.10952
70%	0.99917	1.36787	0.13551	0.99985	1.65017	0.25036	0.12673
80%	0.99812	1.35465	0.15694	0.99985	1.68142	0.28979	0.14523
90%	0.99712	1.30915	0.21360	0.99985	1.70272	0.34904	0.19455
95%	0.99649	1.24048	0.30922	0.99985	1.65916	0.37131	0.27997
98%	0.99521	1.12461	0.52268	0.99985	1.56926	0.39434	0.47034
99%	0.99404	1.03795	0.74757	0.99985	1.49576	0.40601	0.67061

Table 8. Size Distribution and Hygroscopic Growth analysis (Model 5-SOOT)

			μ=5.13466
λ	R^2	γ	*ν*
0.55	0.998	0.413	3.116334
0.65	0.997	0.421	3.156321
0.75	0.996	0.426	3.182447

DOI: https://doi.org/10.30564/jasr.v4i3.3430

BILINGUAL PUBLISHING CO.
Pioneer of Global Academics Since 1984

Journal of Atmospheric Science Research
https://ojs.bilpublishing.com/index.php/jasr

ARTICLE

Long Term Spatio-temporal Variations of Seasonal and Decadal Aridity in India

Pavan Kumar B[1] **Bhavani Pinjarla**[2*] **P K Joshi**[3] **P S Roy**[4]

1. International Crops Research Institute for the SemiArid Tropics, Hyderabad, 502324, India
2. International Maize and Wheat Improvement Center (CIMMYT), New Delhi, 110012, India
3. School of Environmental Sciences (SES), Special Center for Disaster Research (SCDR), Jawaharlal Nehru University (JNU), New Delhi, 110067, India
4. World Resources Institute India, New Delhi, 110016, India

ARTICLE INFO

Article history
Received: 19 July 2021
Accepted: 9 August 2021
Published Online: 12 August 2021

Keywords:
Aridity index
Aridity index anomaly
NDVI
Potential evapotranspiration
Precipitation
SPI

ABSTRACT

A comprehensive analysis of climate data (1958-2018) is carried out at the national scale in India to assess spatiotemporal variation in aridity. The aridity is analyzed using UNEP (United Nations Environment Programme) Aridity Index (AI), which is the ratio between Precipitation (P) and Potential Evapotranspiration (PET). Freely available Terra-Climate database, P and PET variables, offered an unprecedented opportunity for monitoring variations in AI and aridity index anomalies (AIA) at inter-seasonal and inter-decadal basis. The study also assesses longer term patterns of P and AI anomalies with vegetation anomalies. The results indicate that significant clustered areas with maximum dryness are located at west-central part of India, the state of Maharashtra. Overall, there is a gradual increase in the extent of arid zone during 60-year period and spatially maximum extent of percentage change in aridity area is observed. The change patterns of AI in India are largely driven by the changing patterns of precipitation. The maximum impact of decline in precipitation on AIA was observed during Kharif season frequently, for every 4-5 years during 1972-1992. The pattern repeated in the last few recent years (2013-2018), the decline in precipitation resulted increased aridity. The study also reveals that the availability and usage of irrigation sources have increased from 2014 to 2018. Thus, despite of less precipitation positive vegetation has been resulted in this period. The findings are important to understand the impacts of climate change on land use pattern, and land and water resource management.

1. Introduction

India is an agrarian country with two-third of its population depending on agriculture and allied activities. It stands the first among the rain-fed agricultural countries of the world [1] with about 61 per cent of farmers relying on rain-fed agriculture. Half of the gross cropped area in India under rain-fed farming [2] and is the second largest producer of rice and wheat, staple food for millions of the world (FAO, 2020). The agriculture productivity primarily depends on climatic factors, namely, precipitation, temperature and evapotranspiration [3,4]. The precipitation

---

**Corresponding Author:*
Bhavani Pinjarla,
International Maize and Wheat Improvement Center (CIMMYT), New Delhi, 110012, India;
Email: B.Pinjarla@cgiar.org

DOI: https://doi.org/10.30564/jasr.v4i3.3475

(P), i.e., the quantity of rainfall, its intensity, and its distribution over an area during each cropping season can define the economy of any agriculture dependent country like India [5]. The precipitation and its pattern are also important for gaining an understanding of the micro-level availability of water, which in turn is useful for planning agricultural activities, and land and water development activities for future use [6]. Potential Evapotranspiration (PET) is the rate at which evapotranspiration occurs from a large area that is completely and uniformly covered with growing vegetation that has access to an unlimited supply of soil water, without advection or heat storage effects [7-9]. P and PET can collectively affect the availability of water spatially and temporally [10] impacting society and ecosystems [11]. The relationship with these two climatic factors informs about degree of aridity in the given area. Here, aridity index (AI) is an indicator of degree dryness of the climate at a given location, which is generally calculated as mathematical measures of P (long-term average water supply) and PET (long-term average water demand). This depends on six climatic factors, namely, maximum air temperature, precipitation, actual vapor pressure, actual solar radiation, minimum air temperature and wind speed [12]. Studying AI and its anomalies (Aridity Index Anomaly - AIA) are like monitoring climate variability and its impact on vegetation. The study of these indices is a good tool that policy makers can use to plan agricultural activities, and the use of water resource [13] and its management.

The United Nations Environmental Programme ((UNEP, 1993) defined AI as the ratio of the annual P to the total PET. The high- spatial and temporal resolution Terra Climate dataset has information on various climate variables (both primary and secondary) such as P and PET at a global scale. The monthly datasets of Terra Climate are useful in aridity and other drought index studies [12]. McKee *et al.* [15,16]. [17] developed Standardized Precipitation Index (SPI) a drought index which is simple, easy to calculate and statistically relevant and meaningful. It depends on a single meteorological element, i.e. P, hence flexible and temporally versatile [18,19]. Similarly, the impact of climatic variability on the vegetation can be measured using various remote sensing indices. For example, Normalized Difference Vegetation Index (NDVI) [20] is used most often for monitoring vegetation during growing seasons because of its good correlation with crop productivity [21,22]. Similarly, Enhanced Vegetation Index (EVI) was developed as an alternative vegetation index to address some of the limitations of the NDVI [23]. The Moderate Resolution Imaging Spectro-radiometer (MODIS) provides these vegetation indices fortnightly that are useful in anomaly studies. The NDVI anomaly can be studied along with meteorological indices (AIA and SPI) to characterize drought related impacts on growing vegetation at timescales from month to year [24-27].

The primary objective of the research is to understand distribution of aridity, ranging from month to season, to year across India using Terra Climate (1958-2018) data. The spatio-temporal changes in aridity are assessed using data for 1958-1968 and 2008-2018. To understand the seasonal pattern (aridity anomalies, drought anomalies and vegetation anomalies), State of Maharashtra is taken as a case study, where MODIS-NDVI (2000-2008) anomalies are analyzed with AI and SPI (monthly precipitation and PET data of Terra Climate). These anomalies are compared with agriculture and irrigation data sources. Maharashtra is known for dependence of around 55% of population on agriculture and its allied activities [28,17]. The region has a history of drought [29] and is in a constant state of drought since the year 2012 with deficits in rainfall after every 5-6 years [30,31].

2. Study Area and Data Used

2.1 Study Area

India is a tropical country situated between 06°44′ and 37°30′ north latitude and 68°7′ and 97°25′ east longitude, covering an area of 3,287,263 km^2. The country depicts heterogeneous climatic variation with Himalayan arc in the north, Indian Ocean in south, Arabian Sea in southwest, and the Bay of Bengal in its southeast. The country can be divided into six aridity classes, namely, hyper-arid, arid, semi-arid, dry sub-humid, moist sub-humid and humid. About 15.8% (50.8 Mha) of the geographic area is arid and nearly 37.6% (123.4 Mha) is characterized by semi-arid climatic conditions. Different types of crops are adapted to the natural climate in their respective zones. Over 75% of the cropped area of India falls in the semi-arid tropics (131 million ha out of 174 million ha), which is regularly hit by drought. Both hot and cold arid zones are found in India. In the cold arid zones, the precipitation is low, the vegetation is scattered, and the PET is even as low as zero. Thus, AI values cannot be determined in the cold arid zones. So in this study only the hot arid zone of India (Figure 1) is considered to analyze aridity and its anomalies.

For the study of NDVI, AI and SPI anomalies, state of Maharashtra is taken as a case study. It is situated between 15°44’ and 22°6’ north latitude and 72°36’ E to 80°54’ east longitude. Around 83% of the state is characterized by semi-arid climatic condition [31]. The western boundary is a narrow string of dry and moist sub-humid zones between semi-arid and Ghat region. The Konkan and the

DOI: https://doi.org/10.30564/jasr.v4i3.3475

Ghat regions are humid and per-humid respectively. One-third of Maharashtra receives scanty rainfall. This area constitutes 24% of the drought prone area of India [32]. Several region-wide droughts of moderate to extreme intensity were experienced in Maharashtra between 1871 and 2016, which have adversely affected the agricultural crops [31,33]. The state accounts for about 9.3% of India's population (2011) and 11.6% of gross cropped area (2015-16). Only 18% of the cropped area, which is predominantly rain-fed, is irrigated. In the state, the share of agriculture and allied sectors declined from 26.01% to 17.90% during 1960-61 to 1990-91 respectively and further to 9.9% in 2018-19 [34]. Considering the challenges involved, only agricultural land was studied in the present work.

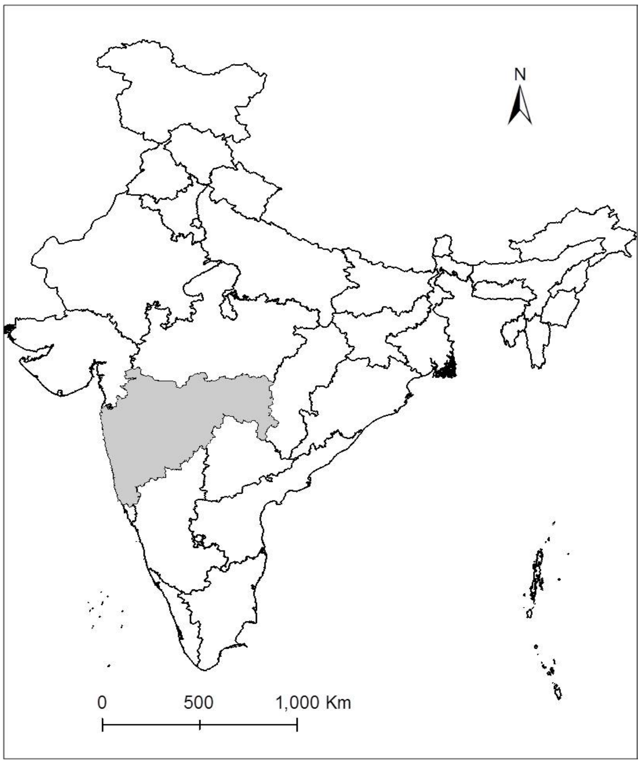

Figure 1. Location of the Study Area. Regional level analysis is done for entire India and local level analysis is done for state of Maharashtra show in grey shade

2.2 Data Used

This study used two types of datasets (i) climate data and (ii) remote sensing data.

2.2.1 Climate data

The meteorological data (P and PET) were downloaded using Google Earth Engine (GEE) platform from Terra Climate database with spatial resolution of ~4 km for a period of 60 years (1958-2018) [14]. These datasets were used to compute AI, AIA, and SPI; over entire India. These were also used to assess the aridity and relationship with precipitation and vegetation indices (NDVI; NDVI Dev) over the state of Maharashtra.

2.2.2 Remote sensing data

MODIS NDVI (MOD13Q1) product with spatial resolution of 250 m generated every 16 days was obtained from LPDAAC (https://lpdaac.usgs.gov) for the years 2000-2018. It was processed using MODIS Reprojection Tool (MRT). Land Use Land Cover (LULC) map of the year 2005 [35] was used to extract agricultural area and other areas were masked out.

2.3 Methodology

The methodology is organized in two sections. The first section describes calculation of assessment of aridity index anomaly and seasonal long-term (60 years) pattern of aridity anomaly across India. The second section describes seasonal patterns of AIA, NDVI anomaly, and SPI.

2.3.1 Aridity Index Anomaly (AIA) and decadal changes

The monthly AI was computed using Terra Climate monthly variables i.e., P and PET for the period 1958-2018 while applying the UNEP (United Nations Environment Programme) Aridity Index (AI) (= ratio of P and PET) (UNEP, 1993). The monthly AI data (for 1958-2018) was staked forming altogether 720 layer (60 years × 12 months) database. These AI layers were used to generate AIA [=, where, is the long-term (60-year) mean AI and is the AI layer of the year (1958-2018)]. To carry the inter-seasonal and inter-decadal studies, these monthly AI and AIA layers were converted to seasonal (monsoon, winter, and summer, where each season consist of 60 layers), annual and decadal dataset. The spatial change detection of AI maps for monthly, seasonal, and decadal over regional and local scales (India and Maharashtra, respectively) and hot spot analysis was carried using ArcGIS (Getis-Ord Gi*) tools. AI values were classified into six classes based on UNEP [36,17], i.e., Hyper-arid (HA) ($AI < 0.05$), Arid (A) ($0.05 \leq AI < 0.20$), Semi-Arid (SA) ($0.20 \leq AI < 0.50$), Dry sub-Humid (DsHu) ($0.50 \leq AI < 0.65$), and Humid (Hu) ($AI \geq 1$). The resulted hot and cold spots were classified into seven categories based on their Gi Bin values: Hotspot (HS) 99% significant, HS 95% significant, HS 90% significant, not statistically significant, cold spot (CS) 90% significant, CS 95% significant, and CS 99% significant [37]. The temporal variation plots and change in area and percentage of total arid area were carried out by extracting statistical values of AI and AIA using R software and ArcGIS tools.

2.3.2 Seasonal patterns analysis of AIA, NDVI anomaly, and Standardized Precipitation Index (SPI)

The seasonal pattern of AIA along with SPI is carried out to assess the impact on agriculture over extremely significant hot spot regions of aridity. The AIA for the year 2000-2018 was computed using the methodology as explained in the earlier section. For the computation of NDVI anomaly and SPI the following methods were used.

2.3.3 NDVI anomaly

MODIS NDVI products of 250 m resolution produced fortnightly were downloaded from the LPDAAC data pool. The dataset was re-projected with the WSG84 datum. The fortnightly NDVI products were transformed into monthly data by selecting the maximum NDVI of each month from 2000 to 2018. These monthly NDVI data were stacked in sequence for each month. The masking out of the non-agricultural area was carried out using the agriculture area (cropland and fallow land) from the LULC map of the year 2005 [35] to prepare MODIS agricultural NDVI files. The monthly NDVI files were used to generate the NDVI anomaly [=, where, is the mean NDVI and is the NDVI layer for each month of the year (2000-2018)].

2.3.4 Standardized Precipitation Index (SPI)

The SPI is a drought index representing the probability of occurrence of the observed rainfall at a location compared with a long-term reference period. The monthly precipitation data were stacked for the period from 2000 to 2018. The mean and standard deviation of these layers were calculated using the ERDAS software package. The monthly precipitation data were used to calculate the SPI [=, where, and represent the ith value and the mean value and σ represents the deviation from the mean value]. The non-agricultural area was masked out from the monthly (2000-2018) SPI layers.

The AI anomaly, NDVI anomaly, and SPI were determined for three seasons: the summer monsoon (June-September), winter (October-January) and summer (February-May) as the mean values of the months of each season. The seasonal files were extracted using the R software package (http://openwetware.org/wiki/R_Statistics). The overall methodology of this study is illustrated in Figure 2 (a, b).

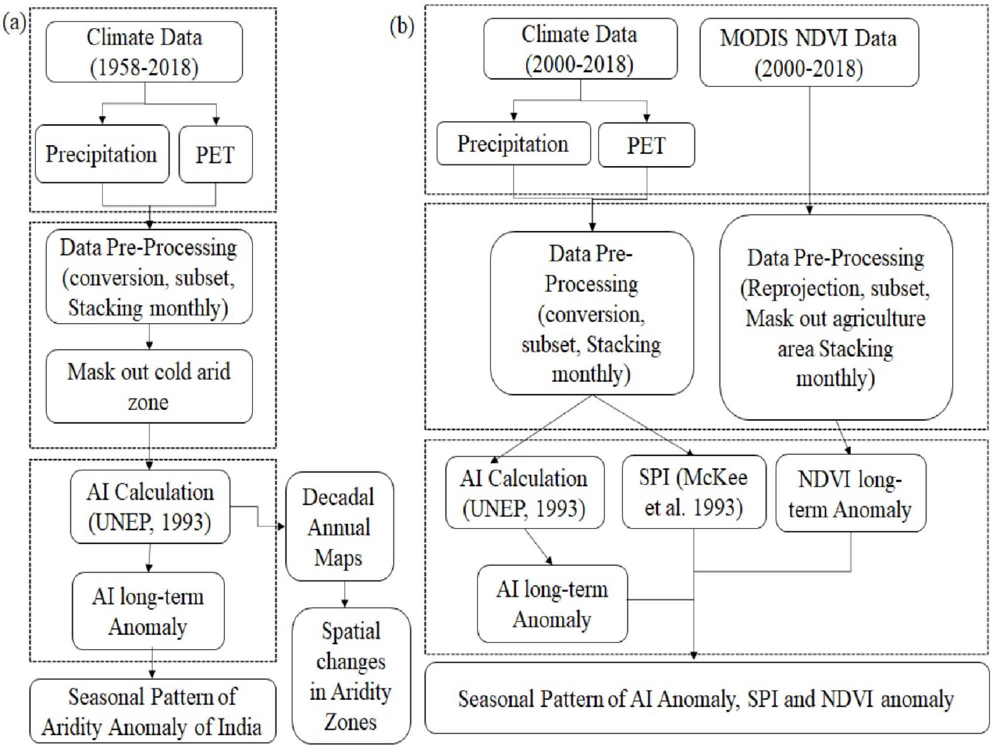

Figure 2. Schematic diagram of approach used for (a) long-term aridity anomaly and decadal changes in arid zones in India, and (b) seasonal analysis of aridity anomaly, SPI and NDVI anomaly

DOI: https://doi.org/10.30564/jasr.v4i3.3475

3. Results

Climate parameters play an important role in deciding the aridity over a region, and the quality of precipitation and PET performs an essential position in terms of understanding the extent and scale of aridity over the region. The AI, which is an indicator of degree of dryness, was analyzed for temporal (monthly, seasonal, decadal and sixty year) and spatial changes in arid zones. The AI was spatially analyzed to identify significant hot spot arid region and the impact of climate and aridity variation on agricultural regions.

3.1 Seasonal Pattern of AIA (1958-2018)

The seasonal patterns of AIA are explained by bisecting the monthly into seasonal pattern i.e., monsoon (June-September), winter (October-January) and summer (February-May) to understand the seasonal variability over India (Figure 3 a-c). The temporal patterns were inferred, by comparing the frequency (number of years) of negative AIA (more than 2 months in each season) between 1958-92 and 1993-2018 years. During monsoon, frequency of negative AIA is the maximum in the last 25 years compared to 1958-1992. This indicates that the region is turning to dryer. Extreme dryness is observed during the year 2002-03 (Figure 3a). During winter, the fluctuation of aridity level is noticed for the year 1958-1992, whereas the magnitude of aridity is extreme in the beginning of October month, followed by end of January month in sixty years. The consistent increasing trend in aridity is observed in the last 18 years (2000-2018), except the years 2005-06, 2010-11 and 2013-14. And for summer, the maximum number of years showed negative AIA during 1958-1992 (Figure 3 b-c).

3.2 Long Term (1958-2018) Pattern of AIA with Precipitation Anomaly

The long-term (1958-2018) analysis, monthly precipitation and PET data were used, and the mean seasonal and annual AIA anomaly with annual precipitation anomaly was assessed at regional level of India (Figure 4). Analysis of Seasonal AIA with

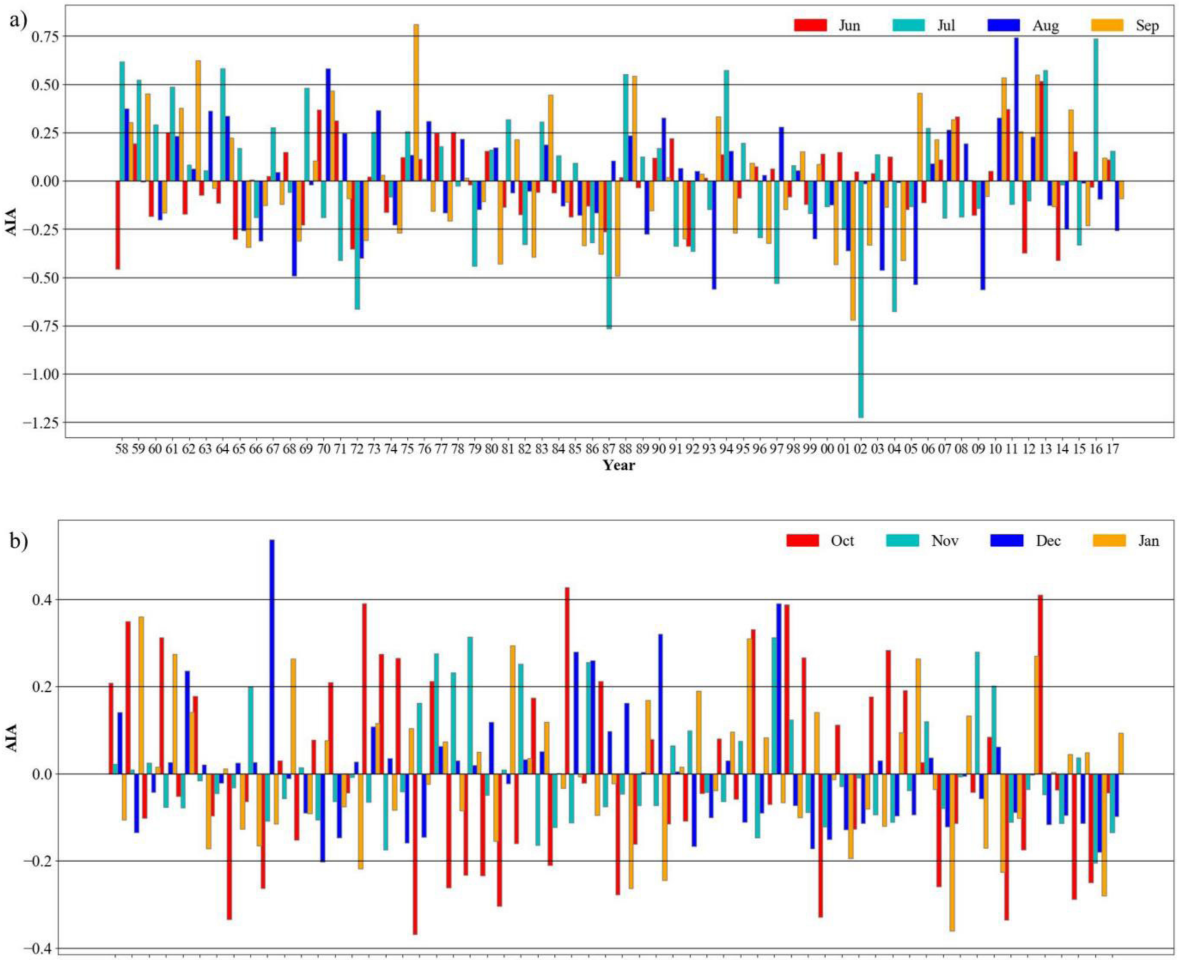

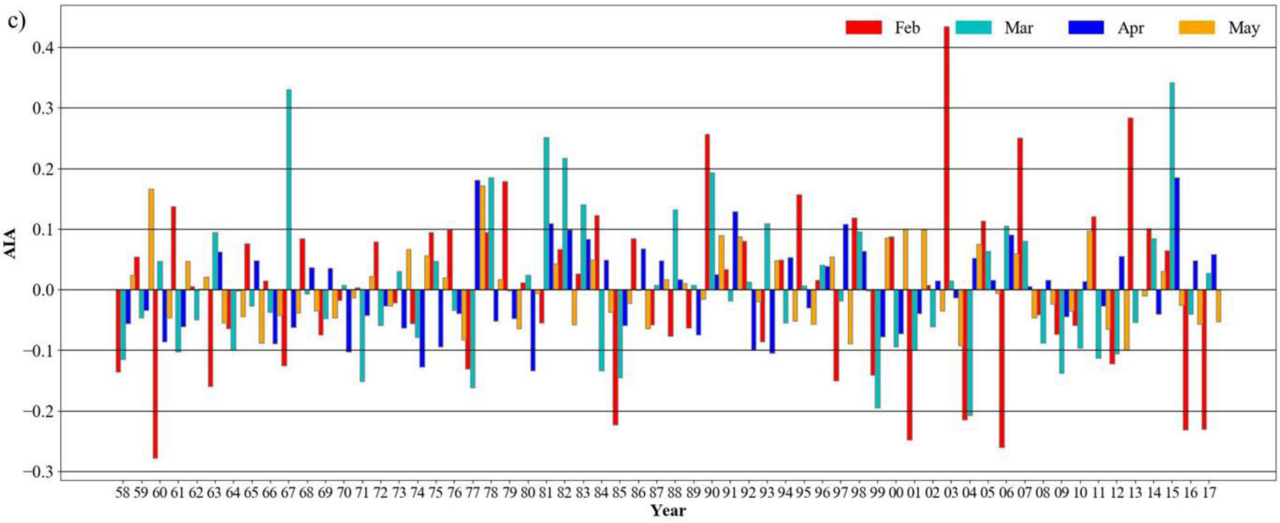

Figure 3. Monthly/seasonal pattern of AIA during 1958-2018 (a) monsoon, (b) winter, and (c) summer seasons

precipitation anomaly shows that the season-wise AIA follows the pattern with annual precipitation anomaly. The negative anomalies (AIA and precipitation anomalies) were found continued in all the seasons from 1965 to 1967, followed by 2002-2005. The maximum impact of decline in precipitation on AIA was observed during kharif season. This was very frequent for every 4-5 years during 1972-1992. In the last few years (2013-2018) over again, the decline in precipitation had an impact on aridity of an area. The changed patterns of AI over a period in India are largely driven by the changing patterns of precipitation [38].

3.2.1 Spatial (monthly) change in AI

Spatial distribution of monthly mean of AI (for 60 years) is shown in Figure 5. Distribution during January-March shows an increasing (maximum) range of aridity levels from eastern to western part of India. In the extremely dry months (April-May), northern and central regions of India indicate characteristics of hyper-arid zone. An increasing level of humid condition is observed during wet months (June-September). Due to excess in rainfall in July-August months, these months fall under humid zones. While in October-December an increase in arid condition from south towards north-west regions is been noticed indicating dryness in the north-west part of India.

3.2.2 Seasonal variation (60 years) of AIA

The sixty years spatial distribution of AIA over India in different seasons (monsoon/kharif, winter/rabi and summer/zaid) and annual are given Figure 6. In the monsoon, an

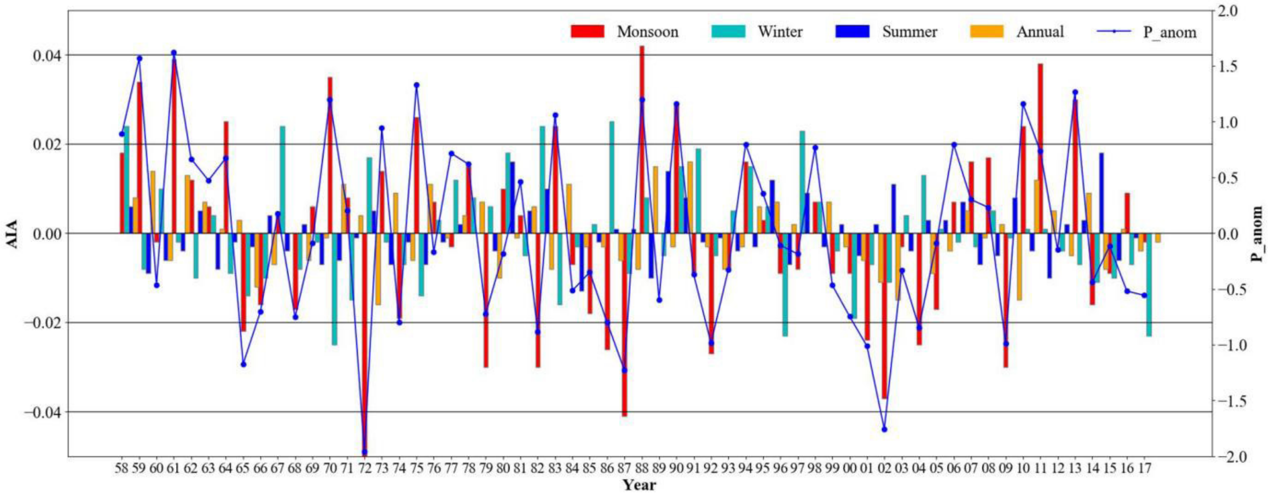

Figure 4. Long term seasonal/annual pattern of AIA with precipitation anomaly in three cropping seasons of India

DOI: https://doi.org/10.30564/jasr.v4i3.3475

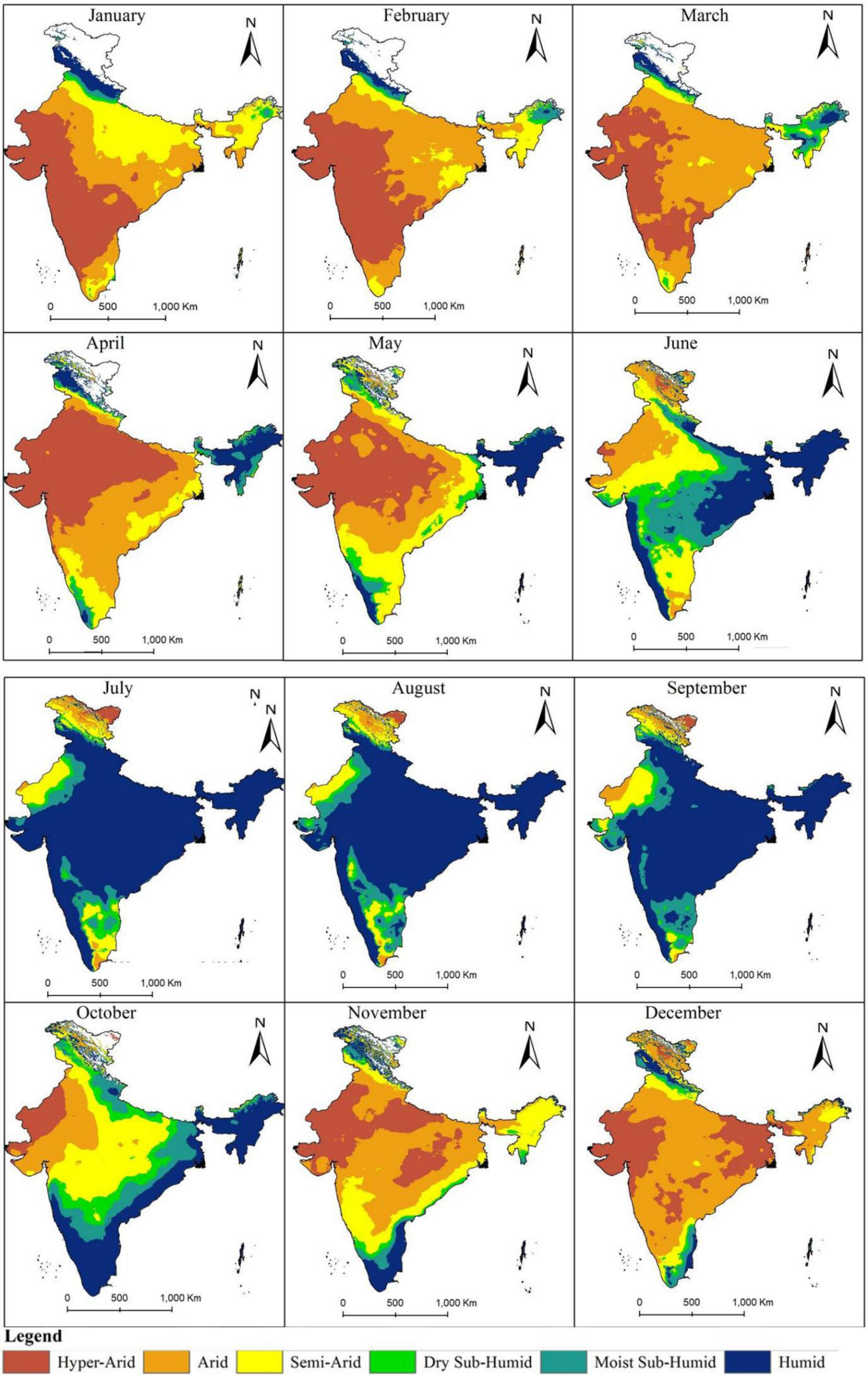

Figure 5. Spatial distribution of monthly mean of 60 years AISeasonal variation (60 years) of AI

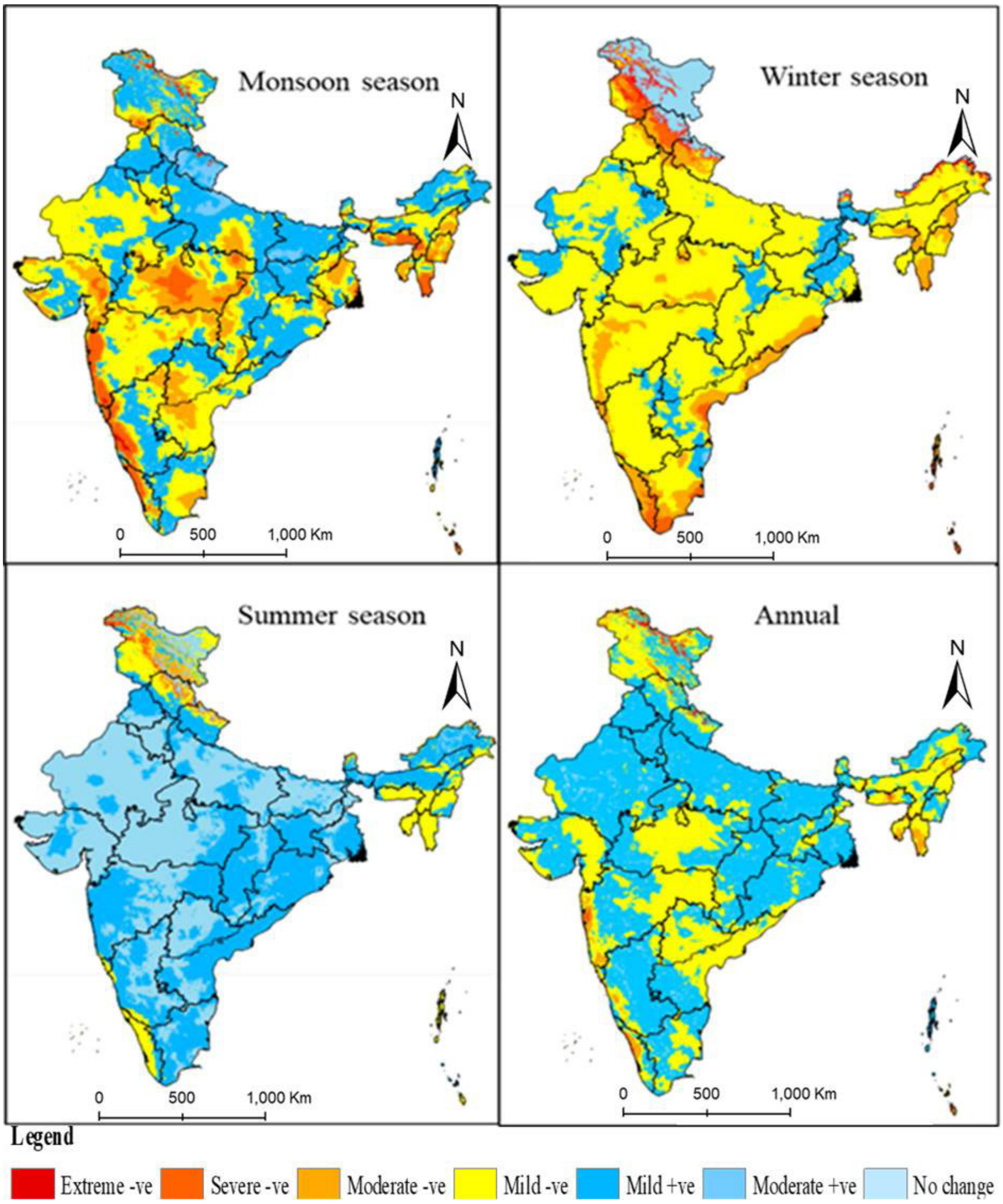

Figure 6. 60 year spatial patter of AIA for the three seasons (monsoon, winter and summer) and annual

extreme negative AIA was observed in the Western Ghats and central part of India. Whereas during winter, most of the area falls at moderate negative AIA and extremely negative is observed towards the tip and eastern costal parts of India. Overall, the annual AIA map over India shows mildly negative to moderately positive distribution.

3.2.3 Annual aridity (1958 and 2018) analysis

The spatial extent of change in the aridity zones over India between 1958 and 2018 is shown in Figure 7. The change in area and percentage of AI from one zone to other i.e., A-H, SA-A, DsHu-SA, DsHu-A, Hu-DsHu, and Hu-SA at state wise are illustrated in tabular format (Table A1). The spatially map shows, a maximum negative change of AI is towards western-central part of India, which indicates that the area is gradually shifting to dryer. The change in area percentage of aridity conditions, from A-H and DsHu-SA are highest at Rajasthan (0.12%) and Maharashtra (1.85%) states. Whereas changes from SA-A, DsHu-SA, and Hu-SA are high at Gujarat states (1.77 %, 0.03% and 1.04%). Overall, there is a gradual increase in the extent of the arid zone during 60-year period and spatially maximum extent of change is observed at Maharashtra region.

3.2.4 Hot spot analysis

The hot spot analysis tool used to identify the areas with significant spatial clustering of high variable values, is illustrated in Figure 8. The results indicate, most of the very high hot spots (statistically significant clustered areas with high negative change in AI are located at west-central part of India. State wise percentage area of hotspot computed from total geographical area of India is shown in Table A2. The maximum percentage areas of HS 99%, and HS 95% confidence level is shown at Maharashtra state, indicating highly significant occurrence of change in arid condition noticed at Maharashtra, followed by Madhya Pradesh state at HS 90% confidence. This indicates that the increase in change in extent of aridity is highest at Maharashtra region.

3.3 Local Scale Analysis - Maharashtra

The climatic parameters and aridity variations will have impact on agriculture. As Maharashtra is proven, highest arid change region from the section 4.1.2. Hence the study carried to assess the impact of aridity and precipitation by comparing the seasonal relationship between AIA and SPI with NDVI anomaly over Maharashtra region.

3.3.1 AIA with NDVI anomaly

The temporal pattern of AIA with NDVI anomaly in three seasons during 2000-2018 is illustrated in Figure 9 a-c. Frequency of occurrence of minimal to maximal range negative AIA are majority (out of 18 years, 11 years are shown negative AIA) during monsoon. Similar NDVI anomaly falls the pattern with AIA is observed over a study period, except during 2015-2018. Whereas, in winter season, the positive pattern of both anomalies was observed only during 2010 and 2011 followed by 2014 and 2015. During dry/summer season, only 5 years (2006, 2011, 2014, 2015 and 2018) are shown positive anomalies indicate good vegetation with residual moist condition.

3.3.2 NDVI and SPI anomalies

The Standardized Precipitation Index (SPI) was calculated using monthly precipitation data for 2000-2018 from Terra Climate. The temporal pattern of SPI with NDVI anomaly in three seasons during 2000-2018 is illustrated in Figure 10a-c. The plots of the NDVI anomalies, mostly aligns with those of the AIA and SPI temporal patters in the three seasons indicating that the

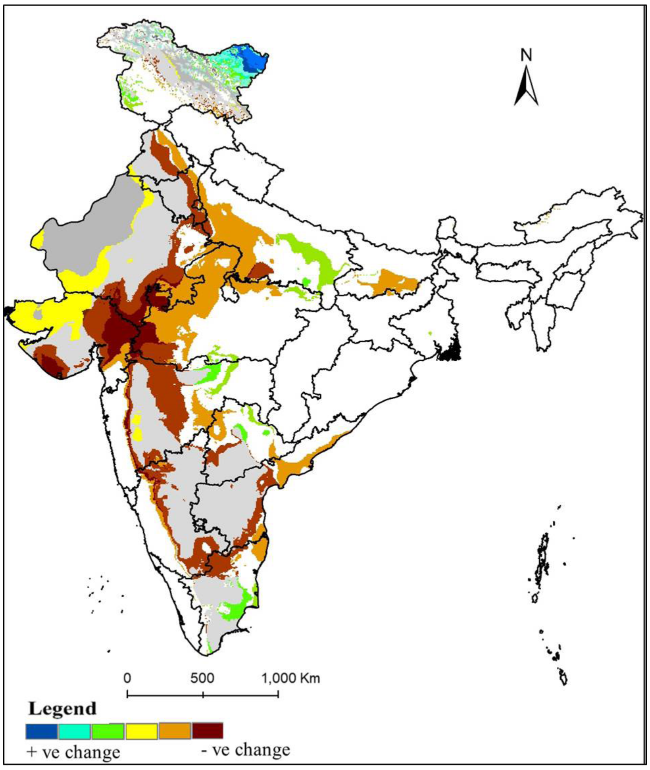

Figure 7. Changes in AI between 1958 and 2018

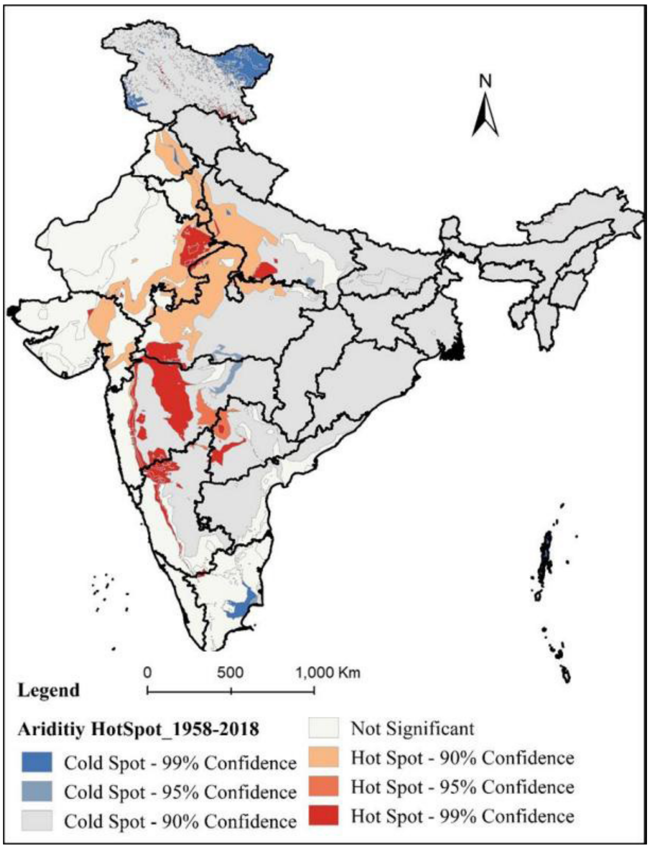

Figure 8. Spatial hotspot analysis of aridity between 1958 and 2018

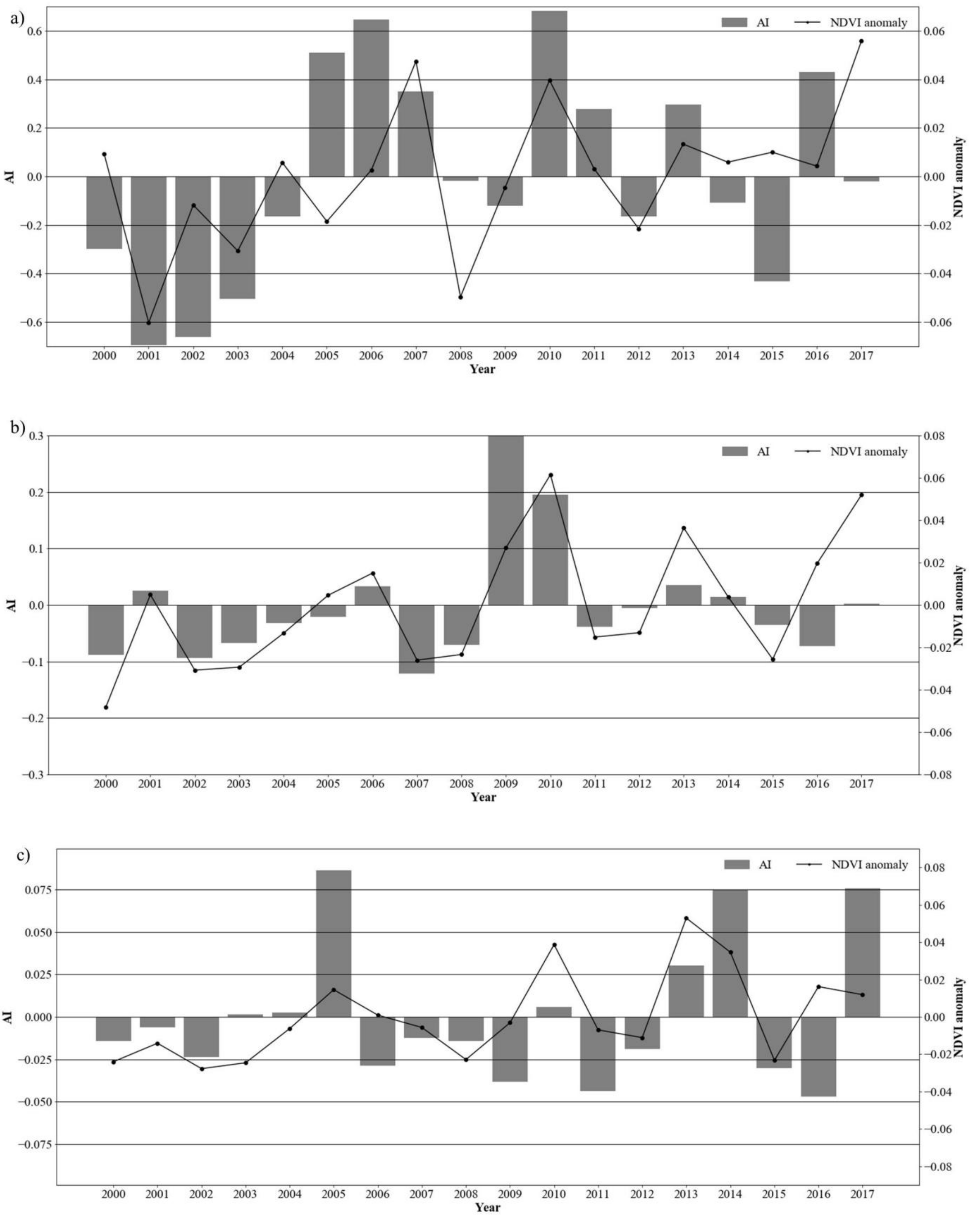

Figure 9. Temporal patterns of AI and NDVI anomaly during 2000-01 to 2017-18, (a) monsoon/kharif, (b) winter/rabi, and (c) summer/zaid season

DOI: https://doi.org/10.30564/jasr.v4i3.3475

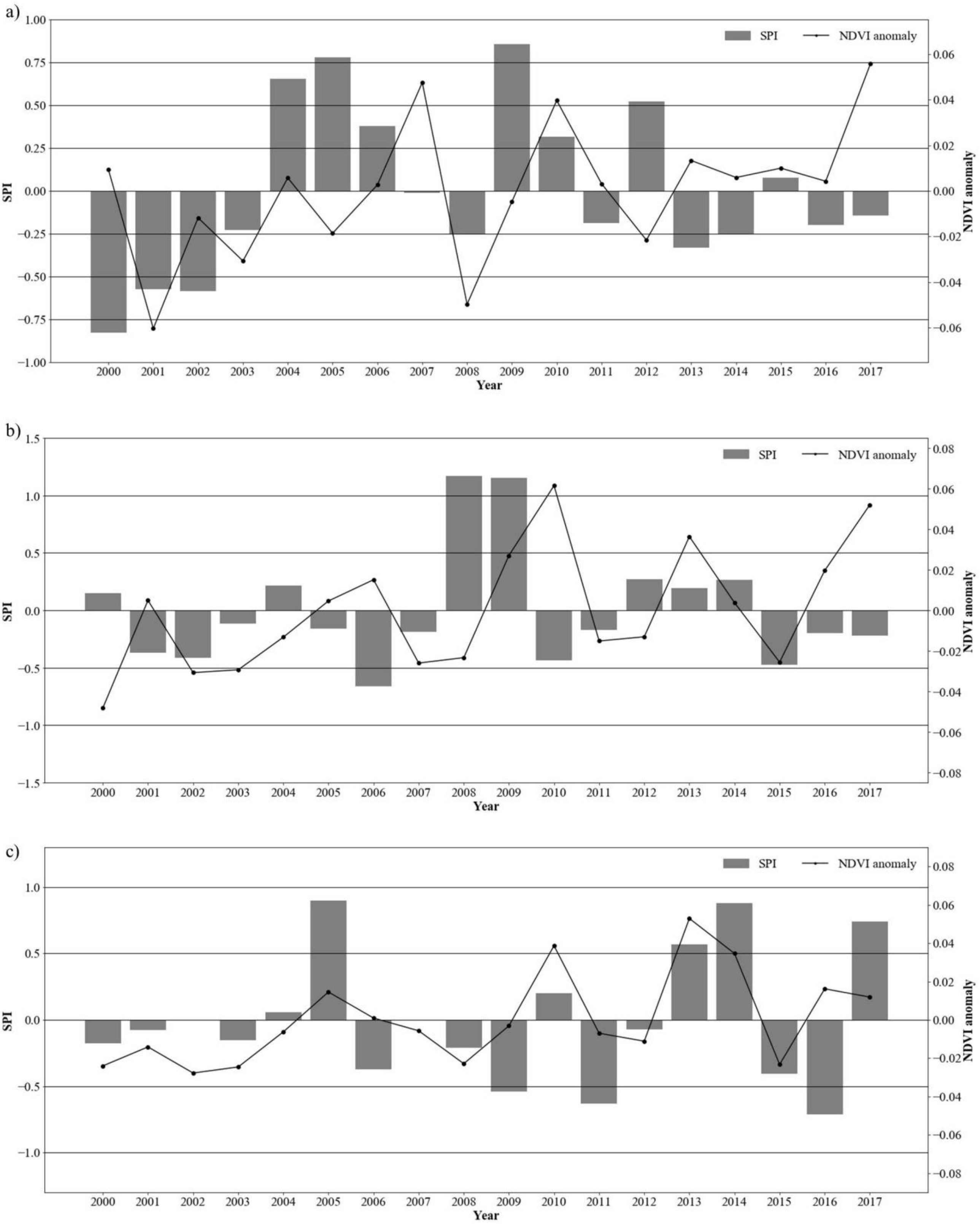

Figure 10. Temporal patterns of SPI and NDVI anomaly during 2000-01 to 2017-18, (a) monsoon/kharif, (b) winter/rabi, and (c) summer/Zaid season

DOI: https://doi.org/10.30564/jasr.v4i3.3475

change in vegetation is due to the precipitation and PET. However, the positive vegetation anomalies during monsoon season shown for recent years (2014 to 2017) despite there being a less precipitation, indicates that usage of available irrigation sources have been increased simultaneously. It was observed that with various major, medium, and minor irrigation projects, a total irrigation potential of 49.26 lakh ha had been created by the end of 2012 [39].

4. Discussion

The effective wetness or dryness of climate over a land area is decided by way of the terrestrial aridity of that area, that is measured with the aid of the ratio of annual mean precipitation to the annual imply ability evapotranspiration [12,13,36]. Earlier studies noted that globally the increase in aridity is due to the fact that the rise in atmospheric demand over land use practices leading to sever land degradation, can amplify the near-surface climatic changes and lead to further desertification over longer periods with exceed in the precipitation changes [40,41]. Thus, the degrees of dryness and the relation with precipitation carried in most of the studies to examine impacts on food grain production over India [38,42] used coarse resolution gridded datasets. Meteorological phenomena, such as fast moving clouds, forefronts variation of solar radiation. This study addresses the research gaps of previous studies with using the fine resolution gridded data sets ($0.05^o \times 0.05^o$) to assess the long term (1958-2018) spatio-temporal change in aridity. This also identifies the most significant hot spots and examines the relation with precipitation and arid conditions on agriculture. The results suggest that the increase in aridity may cause loss of agricultural productivity and impact the food security if mitigation actions are not initiated. More than this the findings are important to understand impacts of climate change on land use pattern, and land and water resource management.

Studying the change in aridity at the regional scale helps to understand the magnitude, identify the extreme hot spot areas and spatial pattern of the changes as well as the shift of lands from one class of aridity to another arid class. The transition of aridity is considered as a foremost and assertive impact of global climate change [27,43,44]. The study examines the sensitivity of gridded precipitation data sets for identification of semi-arid regions over India. It makes reliable assessment of the observed regional aridity changes. Such evidence is important for decision-makers as a signaling mechanism to think about adaptation planning over the semi-arid regions of India (Ramarao *et al*., 2018). Such assessment features the need of satisfactory planning for the water conservation during seasonal precipitation which is often overflown. Such overflow of water during the monsoon season can be utilized for succeeding dry months. Such strategic planning can meet the harvest soil dampness request and lift horticultural creation altogether. To remedy rainfall venture and preserve crop production in the area, piloting irrigation for selected plants, as some farmers are already doing, is particularly endorsed.

5. Conclusions

The present study was conducted to understand the effect of recent changes in climate on aridity and shift of arid land in India between 1958 -1968 and 2008 -2018. For a regional picture across country the monthly and seasonal pattern of AI using Terra Climate (1958 -2018) data was carried out. The Terra Climate data provided trends in precipitation and PET, and these were used to assess the aridity shifts and the impact of aridly. It further focuses on aridity anomalies, drought anomalies and vegetation anomalies and the relations between them while taking a case of state of Maharashtra, India. The MODIS NDVI data were found useful while assessing NDVI anomalies along with AI and SPI. We also used data in agriculture and sources of agriculture to support our results.The incline in aridity in resulted in last 25 and 18 years during monsoon and winter seasons, whereas extreme dryness is noticed in 2002-03 year. The changed patterns of AI over a period are largely driven by the changing patterns of precipitation for every 4-5 years period. Spatial north-west portion of India shows an increase in aridity condition. Spatially variation of change in seasonal change aridity condition is observed i.e, during monsoon Western Ghats and central part of India extreme AIA and towards the tip and eastern costal parts of India in winter season.

Acknowledgements

PKB and PSR are thankful to National Academy of Sciences, India (NASI) Government of India, for the financial support and ICRISAT for the facilities and guidance.

References

[1] A.R. Sathyan, C. Funk, T. Aenis, L. Breuer, Climate Vulnerability in Rainfed Farming: Analysis from Indian Watersheds, Sustainability. 10 (2018). https://doi.org/10.3390/su10093357.

[2] DK Barik, A Need of Climate Smart and Sustainable Agriculture in India, Acta Scientific Agriculture. 3 (2019) 1-3.

[3] R.K. Mall, R. Singh, A. Gupta, G. Srinivasan, L.S. Rathore, Impact of Climate Change on Indian Agriculture: A Review, Climatic Change. 78 (2006) 445-478. https://doi.org/10.1007/s10584-005-9042-x.

[4] S. Singh, S. Nayak, CLIMATE VARIABILITY AND AGRICULTURAL PRODUCTIVITY IN UTTAR PRADESH, INDIA: EVIDENCE FROM PANEL STUDY, (2017).

[5] S. Sangkhaphan, Y. Shu, The Effect of Rainfall on Economic Growth in Thailand: A Blessing for Poor Provinces, Economies . 8 (2020). https://doi.org/10.3390/economies8010001.

[6] P.K. Thornton, P.J. Ericksen, M. Herrero, A.J. Challinor, Climate variability and vulnerability to climate change: a review, Global Change Biology. 20 (2014) 3313-3328. https://doi.org/https://doi.org/10.1111/gcb.12581.

[7] C.W. Thornthwaite, An Approach toward a Rational Classification of Climate, Geographical Review. 38 (1948) 55-94. https://doi.org/10.2307/210739.

[8] S. Sahin, An aridity index defined by precipitation and specific humidity, Journal of Hydrology. 444-445 (2012) 199-208. https://doi.org/https://doi.org/10.1016/j.jhydrol.2012.04.019.

[9] M. Barzani, K. Osman Salleh, Assessment of aridity index in Iran, International Journal of Information and Decision Sciences. 9 (2017) 405. https://doi.org/10.1504/IJIDS.2017.088105.

[10] B.B. Fand, H.E.Z. Tonnang, M. Kumar, S.K. Bal, N.P. Singh, D.V.K.N. Rao, A.L. Kamble, D.D. Nangare, P.S. Minhas, Predicting the impact of climate change on regional and seasonal abundance of the mealybug Phenacoccus solenopsis Tinsley (Hemiptera: Pseudococcidae) using temperature-driven phenology model linked to GIS, Ecological Modelling. 288 (2014) 62-78. https://doi.org/https://doi.org/10.1016/j.ecolmodel.2014.05.018.

[11] G. Konapala, A.K. Mishra, Y. Wada, M.E. Mann, Climate change will affect global water availability through compounding changes in seasonal precipitation and evaporation, Nature Communications. 11 (2020) 3044. https://doi.org/10.1038/s41467-020-16757-w.

[12] C. Li, P. Wu, X. Li, T. Zhou, S. Sun, Y. Wang, X. Luan, X. Yu, Spatial and temporal evolution of climatic factors and its impacts on potential evapotranspiration in Loess Plateau of Northern Shaanxi, China, Science of The Total Environment. 589 (2017). https://doi.org/10.1016/j.scitotenv.2017.02.122.

[13] M.-M. Nistor, P.K. Rai, V. Dugesar, V.N. Mishra, P. Singh, A. Arora, V.K. Kumra, I.-A. Carebia, Climate change effect on water resources in Varanasi district, India, Meteorological Applications. 27 (2020) e1863. https://doi.org/https://doi.org/10.1002/met.1863.

[14] J.T. Abatzoglou, S.Z. Dobrowski, S.A. Parks, K.C. Hegewisch, TerraClimate, a high-resolution global dataset of monthly climate and climatic water balance from 1958-2015, Scientific Data. 5 (2018) 170191. https://doi.org/10.1038/sdata.2017.191.

[15] T. Mckee, N. Doesken, J. Kleist, THE RELATIONSHIP OF DROUGHT FREQUENCY AND DURATION TO TIME SCALES, in: 1993.

[16] T.B. McKee, N.J. Doesken, J. Kleist, Drought Monitoring with Multiple Time Scales, 9th Conference, Applied climatology, in: CONFERENCE ON APPLIED CLIMATOLOGY, Applied Climatology, 9th Conference, Applied Climatology, The Society;, 1995: pp. 233-236. https://www.tib.eu/de/suchen/id/BLCP%3ACN008169111.

[17] State of Indian Agriculture 2015-16. https://agricoop.nic.in/sites/default/files/State_of_Indian_Agriculture%2C2015-16.pdf.

[18] C.A. Karavitis, S. Alexandris, D.E. Tsesmelis, G. Athanasopoulos, Application of the Standardized Precipitation Index (SPI) in Greece, Water . 3 (2011). https://doi.org/10.3390/w3030787.

[19] S. Cheval, The Standardized Precipitation Index - an overview, Romanian Journal of Meteorology. 12 (2015) 17-64.

[20] Jr. Rouse J.~W., R. ~H. Haas, J. ~A. Schell, D. ~W. Deering, Monitoring Vegetation Systems in the Great Plains with Erts, in: NASA Special Publication, 1974: p. 309.

[21] K.R. Hogrefe, V.P. Patil, D.R. Ruthrauff, B.W. Meixell, M.E. Budde, J.W. Hupp, D.H. Ward, Normalized Difference Vegetation Index as an Estimator for Abundance and Quality of Avian Herbivore Forage in Arctic Alaska, Remote Sensing . 9 (2017). https://doi.org/10.3390/rs9121234.

[22] L. Nanzad, J. Zhang, B. Tuvdendorj, M. Nabil, S. Zhang, Y. Bai, NDVI anomaly for drought monitoring and its correlation with climate factors over Mongolia from 2000 to 2016, Journal of Arid Environments. 164 (2019) 69-77. https://doi.org/https://doi.org/10.1016/j.jaridenv.2019.01.019.

[23] A. Huete, K. Didan, T. Miura, E.P. Rodriguez, X. Gao, L.G. Ferreira, Overview of the radiometric and biophysical performance of the MODIS vegetation indices, Remote Sensing of Environment. 83 (2002) 195-213. https://doi.org/https://doi.org/10.1016/S0034-4257(02)00096-2.

[24] B. P., C. V., P.S. Roy, P.K. Joshi, C. K., Long-term agricultural performance and climate variability for drought assessment: a regional study from Telangana and Andhra Pradesh states, India, Geomatics, Natural Hazards and Risk. 8 (2017) 822-840. https://doi.org/10.1080/19475705.2016.1271831.

[25] S. Measho, B. Chen, Y. Trisurat, P. Pellikka, L. Guo, S. Arunyawat, V. Tuankrua, W. Ogbazghi, T. Yemane,

Spatio-Temporal Analysis of Vegetation Dynamics as a Response to Climate Variability and Drought Patterns in the Semiarid Region, Eritrea, Remote Sensing . 11 (2019). https://doi.org/10.3390/rs11060724.

[26] P. Páscoa, C.M. Gouveia, C. Kurz-Besson, A Simple Method to Identify Potential Groundwater-Dependent Vegetation Using NDVI MODIS, Forests . 11 (2020). https://doi.org/10.3390/f11020147.

[27] Y. Wang, C. Zhang, F.-R. Meng, C.P.-A. Bourque, C. Zhang, Evaluation of the suitability of six drought indices in naturally growing, transitional vegetation zones in Inner Mongolia (China), PLOS ONE. 15 (2020) e0233525. https://doi.org/10.1371/journal.pone.0233525.

[28] S.S. Kalamkar, Agricultural growth and productivity in Maharashtra: trends and determinants., Allied Publishers Private Ltd, New Delhi, 2011.

[29] S. Brahme, Drought in Maharashtra, Social Scientist. 1 (1973) 47-54. https://doi.org/10.2307/3516345.

[30] Katalakute, V. Wagh, D. Panaskar, S. Mukate, Impact of Drought on Environmental, Agricultural and Socio-economic Status in Maharashtra State, India, Natural Resources and Conservation. 4 (2016) 35-41. https://doi.org/10.13189/nrc.2016.040301.

[31] R.S. Todmal, Droughts and Agriculture in the Semi-Arid Region of Maharashtra, Western India, Weather, Climate, and Society. 11 (n.d.) 741-754. https://doi.org/10.1175/WCAS-D-18-0131.1.

[32] NIC, Maharashtra State Agricultural Portal - Software Requirement Specification. Department of Agriculture & Cooperation, Ministry of Agriculture, Government of India, 2012. http://agricoop.nic.in/sites/default/files/Maharashtra-SAP_V1.3-2.pdf (accessed September 9, 2020).

[33] Gore PG Ray, KC Sinha, Variability of drought incidence over districts of Maharashtra., Mausam. 53 (2002) 533-538. http://metnet.imd.gov.in/mausamdocs/25341.pdf.

[34] Mumbai. Directorate of Economics & Statistics, Planning Department, Government of -Maharashtra, Economic Survey of Maharashtra 2019-20, 2020. https://mahades.maharashtra.gov.in/files/publication/ESM_18_19_eng.pdf.

[35] P.S. Roy, A. Roy, P.K. Joshi, M.P. Kale, V.K. Srivastava, S.K. Srivastava, R.S. Dwevidi, C. Joshi, M.D. Behera, P. Meiyappan, Y. Sharma, A.K. Jain, J.S. Singh, Y. Palchowdhuri, Reshma.M. Ramachandran, B. Pinjarla, V. Chakravarthi, N. Babu, M.S. Gowsalya, P. Thiruvengadam, M. Kotteeswaran, V. Priya, K.M.V.N. Yelishetty, S. Maithani, G. Talukdar, I. Mondal, K.S. Rajan, P.S. Narendra, S. Biswal, A. Chakraborty, H. Padalia, M. Chavan, S.N. Pardeshi, S.A. Chaudhari, A. Anand, A. Vyas, M.K. Reddy, M. Ramalingam, R. Manonmani, P. Behera, P. Das, P. Tripathi, S. Matin, M.L. Khan, O.P. Tripathi, J. Deka, P. Kumar, D. Kushwaha, Development of Decadal (1985-1995-2005) Land Use and Land Cover Database for India, Remote Sensing . 7 (2015). https://doi.org/10.3390/rs70302401.

[36] UNEP, World Atlas of Desertification, 1993.

[37] D.X. Tran, F. Pla, P. Latorre-Carmona, S.W. Myint, M. Caetano, H. v Kieu, Characterizing the relationship between land use land cover change and land surface temperature, ISPRS Journal of Photogrammetry and Remote Sensing. 124 (2017) 119-132. https://doi.org/https://doi.org/10.1016/j.isprsjprs.2017.01.001.

[38] M. Ramarao, J. Sanjay, K. Raghavan, M. Mujumdar, A. Bazaz, A. Revi, On observed aridity changes over the semiarid regions of India in a warming climate, Theoretical and Applied Climatology. 136 (2019) 1-10. https://doi.org/10.1007/s00704-018-2513-6.

[39] P.V. Salve, A socio economic study of irrigation projects in Maharashtra state with special reference to marathwada region., (2016). http://shodhganga.inflibnet.ac.in:8080/jspui/handle/10603/305734#.

[40] A. Berg, K. Findell, B. Lintner, A. Giannini, S.I. Seneviratne, B. van den Hurk, R. Lorenz, A. Pitman, S. Hagemann, A. Meier, F. Cheruy, A. Ducharne, S. Malyshev, P.C.D. Milly, Land-atmosphere feedbacks amplify aridity increase over land under global warming, Nature Climate Change. 6 (2016) 869-874. https://doi.org/10.1038/nclimate3029.

[41] P. D’Odorico, A. Bhattachan, K.F. Davis, S. Ravi, C.W. Runyan, Global desertification: Drivers and feedbacks, Advances in Water Resources. 51 (2013) 326-344. https://doi.org/https://doi.org/10.1016/j.advwatres.2012.01.013.

[42] L. Goparaju, F. Ahmad, Analysis of Seasonal Precipitation, Potential Evapotranspiration, Aridity, Future Precipitation Anomaly and Major Crops at District Level of India, KN - Journal of Cartography and Geographic Information. 69 (2019) 143-154. https://doi.org/10.1007/s42489-019-00020-4.

[43] M.R. Houmsi, M.S. Shiru, M.S. Nashwan, K. Ahmed, G.F. Ziarh, S. Shahid, E.-S. Chung, S. Kim, Spatial Shift of Aridity and Its Impact on Land Use of Syria, Sustainability . 11 (2019). https://doi.org/10.3390/su11247047.

[44] S. Hadipour, A.K. Abd Wahab, S. Shahid, Spatiotemporal changes in aridity and the shift of drylands in Iran, Atmospheric Research. 233 (2019). https://doi.org/10.1016/j.atmosres.2019.104704.

Supplementary Material

Spatial pattern of dryness

The spatial extent of dryness is computed by differencing two different years' annual AI mean images. The map is categorized into 5 classes based of degree of dryness. In 1958 to 2000, the major extreme to dry classes has been observed at west to central part of India, followed by eastern part of India. In 1958 to 2018, the maximum extent of dryness is observed towards west part of India (Gujarat).

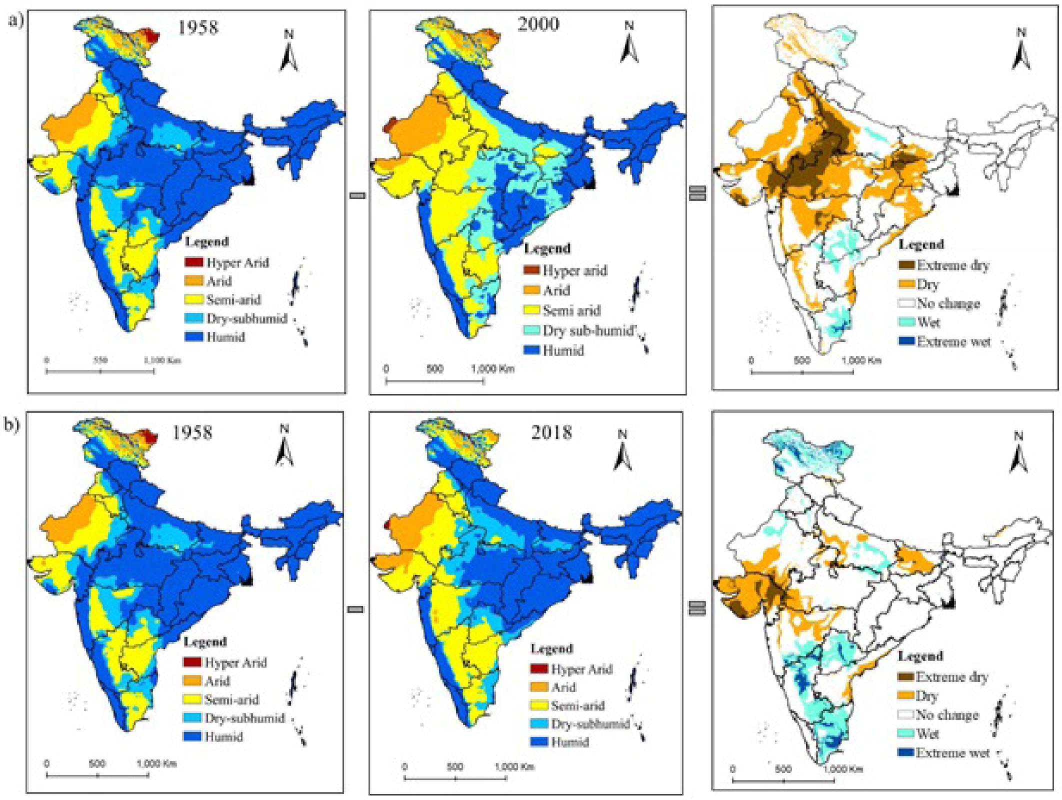

Figure A1. Spatial distribution of extent of dryness maps (a) 1958, 2002 and difference of 1958-2000, and b) 1958, 2018 and difference of 1958-2018

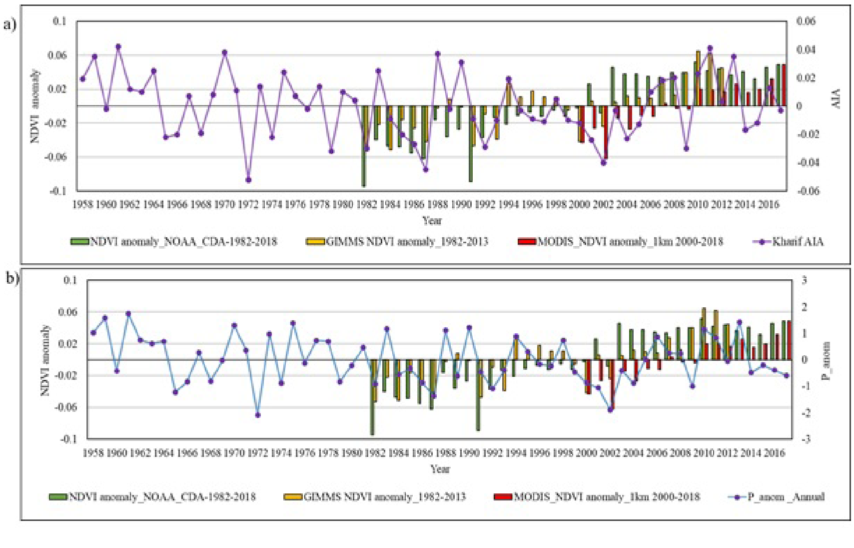

Figure A2. Long term seasonal pattern of (a) Kharif season AIA with NDVI anomaly for 1958-2018, and (b) annual precipitation anomaly with Kharif season inter-sensor NDVI anomaly

DOI: https://doi.org/10.30564/jasr.v4i3.3475

Table A1. State wise percentage change in AI classes

States Names	A-HA	SA-A	DsHu-SA	DsHu-A	Hu-SA
Andaman and Nicobar	0.00	0.00	0.00	0.00	0.00
Andhra Pradesh	0.00	0.00	0.79	0.00	0.01
Arunachal Pradesh	0.00	0.00	0.00	0.00	0.00
Assam	0.00	0.00	0.00	0.00	0.00
Bihar	0.00	0.00	0.00	0.00	0.00
Chandigarh	0.00	0.00	0.00	0.00	0.00
Chhattisgarh	0.00	0.00	0.00	0.00	0.00
Dadra and Nagar Haveli	0.00	0.00	0.00	0.00	0.00
Daman and Diu	0.00	0.00	0.01	0.00	0.01
Delhi	0.00	0.00	0.02	0.00	0.00
Goa	0.00	0.00	0.00	0.00	0.00
Gujarat	0.00	1.77*	1.08	0.03*	1.04*
Haryana	0.00	0.03	0.31	0.00	0.00
Himachal Pradesh	0.00	0.00	0.00	0.00	0.00
Jammu and Kashmir	0.00	0.04	0.11	0.00	0.00
Jharkhand	0.00	0.00	0.00	0.00	0.00
Karnataka	0.00	0.00	1.11	0.00	0.10
Kerala	0.00	0.00	0.00	0.00	0.00
Madhya Pradesh	0.00	0.00	0.46	0.00	0.60
Maharashtra	0.00	0.13	1.85*	0.00	0.19
Manipur	0.00	0.00	0.00	0.00	0.00
Meghalaya	0.00	0.00	0.00	0.00	0.00
Mizoram	0.00	0.00	0.00	0.00	0.00
Nagaland	0.00	0.00	0.00	0.00	0.00
Orissa	0.00	0.00	0.00	0.00	0.00
Pondicherry	0.00	0.00	0.00	0.00	0.00
Punjab	0.00	0.04	0.35	0.00	0.00
Rajasthan	0.12*	0.97	1.23	0.00	0.51
Sikkim	0.00	0.00	0.00	0.00	0.00
Tamil Nadu	0.00	0.00	0.51	0.00	0.00
Tripura	0.00	0.00	0.00	0.00	0.00
Uttar Pradesh	0.00	0.00	0.27	0.00	0.01
Uttaranchal	0.00	0.00	0.00	0.00	0.00
West Bengal	0.00	0.00	0.00	0.00	0.00
India	0.12	2.98	8.10	0.03	2.46

HA - Hyper-arid; A - Arid; SA - Semi-Arid; DsHu - Dry sub-Humid; Hu - Humid

*Highest values among all states

DOI: https://doi.org/10.30564/jasr.v4i3.3475

Table A2. State wise area Percentage of hot spot

State Names	Area Percentage of hot spot						
	CS_99%	**CS_95%**	**CS_90%**	**No Change**	**HS_90%**	**HS_95%**	**HS_99%**
Andaman and Nicobar	0.15	0.00	0.05	0.00	0.00	0.00	0.00
Andhra Pradesh	0.00	0.00	6.20	1.64	0.00	0.28	0.25
Arunachal Pradesh	0.00	0.00	2.57	0.00	0.00	0.00	0.01
Assam	0.00	0.00	2.46	0.00	0.00	0.00	0.00
Bihar	0.00	0.00	2.86	0.02	0.00	0.00	0.01
Chandigarh	0.00	0.00	0.00	0.00	0.00	0.00	0.00
Chhattisgarh	0.00	0.00	4.12	0.00	0.00	0.00	0.00
Dadra and Nagar Haveli	0.00	0.00	0.00	0.02	0.00	0.00	0.00
Daman and Diu	0.00	0.00	0.00	0.02	0.00	0.00	0.00
Delhi	0.00	0.01	0.00	0.00	0.04	0.00	0.00
Goa	0.00	0.00	0.00	0.11	0.00	0.00	0.00
Gujarat	0.00	0.00	0.00	4.76	0.94	0.00	0.04
Haryana	0.01	0.00	0.13	0.78	0.43	0.00	0.00
Himachal Pradesh	0.00	0.00	1.68	0.00	0.00	0.00	0.02
Jammu and Kashmir	1.39	0.02	4.97	0.07	0.00	0.01	0.16
Jharkhand	0.00	0.00	2.46	0.00	0.00	0.00	0.00
Karnataka	0.00	0.00	2.81	2.35	0.00	0.05	0.66
Kerala	0.00	0.00	0.00	1.15	0.00	0.00	0.00
Madhya Pradesh	0.00	0.11	5.02	0.82	2.88	0.01	0.55
Maharashtra	0.00	0.17	4.83	1.77	0.09	0.35*	2.21*
Manipur	0.00	0.00	0.71	0.00	0.00	0.00	0.00
Meghalaya	0.00	0.00	0.70	0.00	0.00	0.00	0.00
Mizoram	0.00	0.00	0.66	0.00	0.00	0.00	0.00
Nagaland	0.00	0.00	0.53	0.00	0.00	0.00	0.00
Orissa	0.00	0.00	4.75	0.00	0.00	0.00	0.00
Pondicherry	0.00	0.00	0.00	0.01	0.00	0.00	0.00
Punjab	0.03	0.01	0.21	0.69	0.61	0.00	0.00
Rajasthan	0.00	0.00	0.00	8.07	1.82	0.01	0.65
Sikkim	0.00	0.00	0.22	0.00	0.00	0.00	0.00
Tamil Nadu	0.32	0.03	0.10	3.49	0.00	0.00	0.02
Tripura	0.00	0.00	0.32	0.00	0.00	0.00	0.00
Uttar Pradesh	0.01	0.04	4.52	0.73	1.79	0.01	0.24
Uttaranchal	0.00	0.00	1.62	0.00	0.00	0.00	0.00
West Bengal	0.00	0.00	2.56	0.01	0.00	0.00	0.00

C - Cold Spot; HS - Hot Spot and value % is significant level.

*Highest values among all states

BILINGUAL PUBLISHING CO.
Pioneer of Global Academics Since 1984

Journal of Atmospheric Science Research
https://ojs.bilpublishing.com/index.php/jasr

ARTICLE

Kinetics of the Oxidation of Hydrogen Sulfide by Atmospheric Oxygen in an Aqueous Medium

Deepak Singh Rathore Vimlesh Kumar Meena Chandra Pal Singh Chandel Krishna Swarup Gupta*

Atmospheric Chemistry Laboratory, Department of Chemistry, University of Rajasthan, Jaipur, 302004, India

ARTICLE INFO

Article history
Received: 15 July 2021
Accepted: 12 August 2021
Published Online: 16 August 2021

Keywords:
Hydrogen sulfide
Oxygen
Oxidation
Kinetics
Effect of organics

ABSTRACT

Hydrogen sulfide is an important acid rain precursor and this led us to investigate the kinetics of its oxidation in aqueous phase by atmospheric oxygen. The kinetics was followed by measuring the depletion of oxygen in a reactor. The reaction was studied under pseudo order conditions with $[H_2S]$ in excess. The kinetics followed the rate law:

$$-d[O_2]/dt = k[S][O_2]_t \qquad \text{(A)}$$

Where [S] represents the total concentration of hydrogen sulfide, $[O_2]_t$ is the concentration of oxygen at time t and k is the second order rate constant.

The equilibria (B - C) govern the dissolution of H_2S; the sulfide ion in water forms different species:

$$H_2S \xrightleftharpoons{K_1} HS^- + H^+ \qquad \text{(B)}$$

$$HS^- \xrightleftharpoons{K_2} S^{2-} + H^+ \qquad \text{(C)}$$

Where K_1 and K_2 are first and second dissociation constants of H_2S.

Although, H_2S is present as undissociated H_2S, HS^- and S^{2-} ions, nature of $[H^+]$ dependence of reaction rate required only HS^- to be reactive and dominant. The rate law (A) on including $[H^+]$ dependence became Equation (D).

$$-d[O_2]/dt = k_1K_1[H^+][S][O_2]_t / ([H^+]^2 + K_1[H^+] + K_1K_2) \qquad \text{(D)}$$

Our results indicate anthropogenic VOCs such as acetanilide, benzene, ethanol, aniline, toluene, benzamide, *o*-xylene, *m*-xylene, *p*-xylene and anisole to have no significant effect on the reaction rate and any observed small effect is within the uncertainty of the rate measurements.

1. Introduction

There are several reasons for undertaking studies on the aqueous phase atmospheric oxidation of hydrogen sulfide, H_2S, by oxygen. Firstly, along with sulfur dioxide, SO_2, and dimethyl sulfide, CH_3SCH_3, it is among the major sulfur – based trace atmospheric gases, which are all acid rain precursors. H_2S is emitted by both natural and anthropogenic sources. The natural sources of H_2S include the anaerobic degradation of organic matter [1], sulfur springs, swamps, volcanoes, natural gas, some well waters, geothermal active areas, etc. The anaerobic biogenic reactions in coastal wetlands, soils and plants, volcanoes, and biomass burning [2], produce reduced sulfur compounds like H_2S, COS, DMS, etc. The sulfide minerals, which are the most important group of ore

---

**Corresponding Author:*
Krishna Swarup Gupta,
Atmospheric Chemistry Laboratory, Department of Chemistry, University of Rajasthan, Jaipur, 302004, India;
Email: guptaks200@gmail.com

DOI: https://doi.org/10.30564/jasr.v4i3.3465

minerals, are the other natural source of sulfides. Several industrial processes such as coke production, viscose rayon production, wood pulp production, sulfur extraction processes, oil- refining, tanning, oil and gas drilling, production and refining, liquid manure are the man made sources of H_2S. The stagnant bodies of water and sewers also release H_2S.

Secondly, bacterial breakdown of organic materials in human and animal wastes, sewage, stagnant wastewater and sewers is responsible of toxic H_2S and its foul smell. It affects the human health adversely and causes health hazards.

Thirdly, whereas the atmospheric chemistry of aqueous SO_2 has been the subject of extensive studies [3-5], the same is not true of H_2S. The oxidations of SO_2 directly and that of H_2S via SO_2 in to sulfate are responsible for acidification of atmospheric waters and formation of sulfate aerosols. Obviously, for understanding the aqueous phase atmospheric oxidation of H_2S by oxygen, there are some aspects, which from atmospheric chemistry point of view need serious reinvestigation under ambient experimental conditions of pH, $[O_2]$, anthropogenic VOCs, etc, which mimic atmospheric waters.

Fourthly, the atmospheric chemistry of hydrogen sulfide plays an important role in sulfur cycle. Along with other reduced sulfur compounds, it is oxidized to SO_2, and thereafter largely to sulfate. Organization for Economic Co-operation and Development(OECD) [6] estimates that the origin of about half of the global SO_2 is the oxidation of H_2S. Lifetime of H_2S is ~ 4.4 days. Thus, H_2S is one of the main precursors of SO_2 and sulfate in atmosphere [7].

Finally, volatile organic compounds intervene and influence the atmospheric chemistry of acid rain [8], photochemical smog [9], etc. Even then, there appears to be only few cursory brief reports on the role of some organic compounds on the inhibition of the autoxidation of H_2S [10,11]. Similarly, on the role of ammonia no report has come to our notice.

Generally, very low ambient concentrations of hydrogen sulfide are found in the atmosphere. While the ambient H_2S concentrations range from 0.11 ppb to 0.33 ppb in rural areas, the values are generally less than 1 ppb in urban areas [12]. In some cases, relatively very high concentrations, exceeding 90 ppb, have been reported near natural sources and H_2S releasing industries [13].

Oxygen readily oxidizes hydrogen sulfide. A decrease in pH decreases the rate of hydrogen sulfide oxidation [14], which may have implications for sulfide ore mines with acid mine drainage; in the latter case, the acid would be sulfuric acid, but hydrogen sulfide gas may still be present. The oxidation of H_2S by O_2, i.e., autoxidation of H_2S, takes place in all forms of atmospheric waters resulting in a variety of oxidation products such as sulfur, S^o, sulfite ion, SO_3^{2-}, thiosulfate ion, $S_2O_3^{2-}$, and sulfate ion, SO_4^{2-}, etc. [15-20]. This reaction is of great significance in seawater [21-29] and wastewater [30,31].

The oxidation of H_2S by other oxidants such as chromate(VI) [32], ferrate(VI) [33], hydrogen peroxide [34] and peroxomonosulfate [35] has also been studied. Tomar and Abdullah [36] found the oxidation of H_2S in wastewater to be slow.

The results of reported H_2S autoxidation kinetics studies differ widely although in general kinetics order in each of H_2S and O_2 is reported to be one [21,37-39] although some studies report higher, lower or complex orders [16]. Some studies have been carried out with highly pure solutions and reagents [17]. Luther et al. [37] reported that in the absence of trace metals the reaction is very slow. There are conflicting reports about induction period and colloidal sulfur formation. Whereas, Chen and Morris [16] in their buffered study of uncatalyzed reaction in the pH range 6-13 observed an induction period of up to one hour, under similar reaction conditions O'Brien and Birkner [18] (pH= 4-10) found no induction period. Whereas, Chen and Morris [16], Millero [21] reported the polysulfide formation, Avrahami and Golding [17], O'Brien and Birkner [18] did not report any such phenomenon. As regards the products, sulfate was reported as a final product [17,18].

This led us to look afresh into the atmospheric chemistry of H_2S oxidation and to examine the effect of several parameters such as reactant concentrations, pH and importantly the effect of some anthropogenic volatile organic compounds(VOCs) particularly those which are reported to strongly inhibit the oxidation of aqueous SO_2 by oxygen in laboratory water. The oxidation kinetics of aqueous SO_2 and effect of VOCs has been studied by several groups [3,8,40-57].

2. Experimental

The experimental procedure for studying the kinetics of aqueous hydrogen sulfide oxidation by oxygen was same as described previously [58]. Briefly it is described here. Reactions were conducted in air-tight sealed three necked glass reactor of 250 ml capacity which was immersed in a thermostated water bath to maintain the desired temperature (±0.1). The dissolved oxygen probe was fitted in one neck and the oxygen from a cylinder was passed through the other neck. The third neck was used for adding standard sodium sulfide solution. The procedure for studying kinetics was as follows. At first the oxygen was passed in the reactor till the desired concentration of O_2 was achieved. Immediately, afterwards, the

DOI: https://doi.org/10.30564/jasr.v4i3.3465

standardized Na_2S solution was added and the reactor sealed. The kinetics was followed by recording decrease in O_2 concentration by DO meter (Durox Oxi-3205).

In lieu of hydrogen sulfide, sodium sulfide was used, which generated sulfide species in aqueous solution through hydrolysis of sulfide ion, S^{2-}.

$$S^{2-} + H_2O \rightleftharpoons HS^- + OH^- \tag{1}$$

$$HS^- + H_2O \rightleftharpoons H_2S + OH^- \tag{2}$$

The solution of Na_2S was prepared in double distilled water daily afresh.

The replicate rate determinations were generally reproducible within ± 20%. As discussed later the high uncertainty results from the catalytic activity of trace metal ion impurities [59]. All calculations were performed on MS Excel 2007. The values of rate coefficients together with standard deviations and correlation coefficients have been presented.

2.1 Product Analysis

The kinetics of this reaction has been studied under deficit $[O_2]$ at a ratio $[O_2]/[S] \approx 0.012 - 0.12$, where $[O_2]$ and [S] represent initial O_2 and H_2S concentrations, respectively. This $[O_2]/[S]$ ratio was optimum for studying kinetics study although it is much different than the atmospheric ratio. The products were identified by running the experiments at $[S] = 2\times 10^{-3}$ mol L^{-1} and $[O_2] = 2\times 10^{-4}$ mol L^{-1} at pH ≈10.6 and T= 30°C. The reaction was allowed to reach completion. No change in color of the reaction mixture during the progress as well as at the end of the reaction was noticed. There was no appearance of turbidity showing that no formation of colloidal sulfur/poly sulfides took place [11] and the mixture remained transparent. Thus, our experimental conditions do not appear to favor colloidal sulfur formation. Although the formation of polysulfides species in solutions of pH more than 8 has been noted [16], stoichiometry of sulfide-oxygen reaction depends on pH, concentration of reactants, and the existence of extraneous substances or impurities. The sulfite ion, which is an important intermediate, could not be detected. Probably, even if it is formed, it is oxidized to sulfate [16]. So, sulfate was found to be the only product, which could be detected.

Since $[O_2]$ was low ($\approx 10^{-4}$ mol L^{-1}) any oxidation product formed would also be low. To collect a measurable amount of the products, these experiments were repeated ten times. All final reaction solutions were mixed. And the resultant solution was acidified and heated to expel sulfide as H_2S. Sulfate was detected as a product by precipitating it as insoluble $BaSO_4$ and following the usual procedure. Like the present work, there are many other studies which also indicate the formation of sulfate as a major product in alkaline media. Zhang and Millero [60] reported that the final product from the oxidation of sulfide is sulfate.

Although many intermediates such as sulfite, thiosulfate, sulfur (0), polysulfides etc. have been proposed for this reaction, sulfite has been considered as a initial product, which is oxidized ultimately to sulfate [61].

3. Results

3.1 Preliminary Investigations

Kinetics was studied under pseudo first order conditions and the oxygen was in deficit. Concentration of sulfide was in excess at least ten times over oxygen concentration. Hereafter, [S] represents the total H_2S concentration including its all species. The rate of oxidation was measured by following the disappearance of $[O_2]$. In most cases, the reaction obeyed a first order kinetics in $[O_2]$ (Figure 1). Values of pseudo first order rate constants, k_{obs}, were obtained from log $[O_2]_t$ versus time, t, plots defined by Equation (3).

$$-d[O_2]/dt = k_{obs}[O_2]_t \tag{3}$$

Where $[O_2]_t$ is concentration of oxygen at time, t.

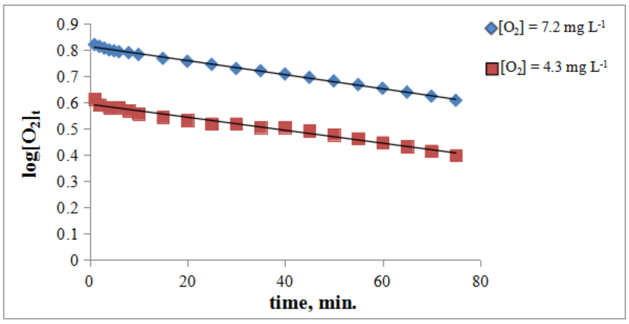

Figure 1. The plot of log $[O_2]_t$ versus time at pH = 10.82-10.86, $[S] = 2\times10^{-3}$ mol L^{-1} and T = 30°C

The dependence of reaction rate on pH is an important parameter due to the equilibria (1-2). The initial forays on pH dependence were made by carrying out the variation in pH in both the unbuffered and phosphate buffered media. In case of buffered study, in the kinetics run, the initial pH was fixed with the help of phosphate buffer by fixing the desired initial pH (±0.02) by varying $[Na_2HPO_4]/[NaH_2PO_4]$ ratio. In case of unbuffered study, the desired initial pH (±0.02) of the reaction mixture was fixed by addition of dilute perchloric acid. In this case, pH decreased with the progress of the reaction.

The results of pH dependence of rate at almost similar initial pH of reaction mixtures in both buffered and unbuffered media are compared in Table 1, which shows k_{obs} values to be relatively high (130%) in buffered

DOI: https://doi.org/10.30564/jasr.v4i3.3465

media. This is probably due to introduction of trace metal impurities, when the buffer is used. Similar to S(IV) autoxidation studies [3], several previous studies report the catalysis of H_2S oxidation by trace metal ions [59]. Recent studies from our laboratory report the presence of catalytic metal ions such as iron, manganese, cobalt, copper, etc in rainwater samples collected at Jaipur [8,61,62-64]. The concentrations of metal ions in rainwater are larger than those in distilled water [64].

In general, the homogenous trace metal catalyzed reactions are inhibited by Ethylenediamine tetraacetate (EDTA). Indeed the latter is reported to inhibit the sulfide autoxidation [11]. The catalytic metal ions present as impurity in water and reagent samples are strongly complexed by EDTA and rendered inactive resulting in inhibition. In this study, the addition of EDTA led to a decrease in the rate of oxidation of H_2S (Figure 2) and at [EDTA] $\geq 1\times10^{-5}$ mol L^{-1} the reaction was completely inhibited (Figure 3). This clearly indicates that the impurity metal ions catalyze the rate of this reaction [63]. In view of this, to avoid the introduction of impurity ions, the entire study has been carried out in an unbuffered medium without using any buffer.

3.2 Rate Law

To arrive at the rate law, at first the effect of [S] was

Table 1. Values of k_{obs} in phosphate buffered and unbuffered media at [S] = 2×10^{-3} mol L^{-1} and T = 30°C

Experiment	Unbuffered medium		Buffered medium		$k_{obs(Buffered)}/\ k_{obs(Unbuffered)}$
	Initial pH	k_{obs}, s^{-1}	Initial pH	k_{obs}, s^{-1}	
1	8.85	1.14×10^{-4}	8.83	1.74×10^{-4}	1.53
2	8.26	9.94×10^{-5}	8.27	3.23×10^{-4}	3.25
3	8.04	7.64×10^{-5}	8.01	1.53×10^{-4}	2.02
4	7.7	8.37×10^{-5}	7.71	1.93×10^{-4}	2.31 Average = 2.3 ± 0.5

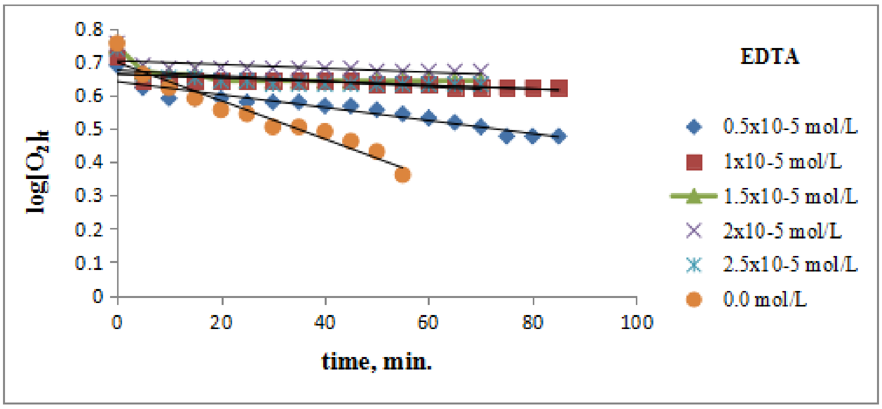

Figure 2. Effect of EDTA on the rate of H_2S autoxidation at pH = 10.81-10.9 at [S] = 2×10^{-3} mol L^{-1} and T = 30°C

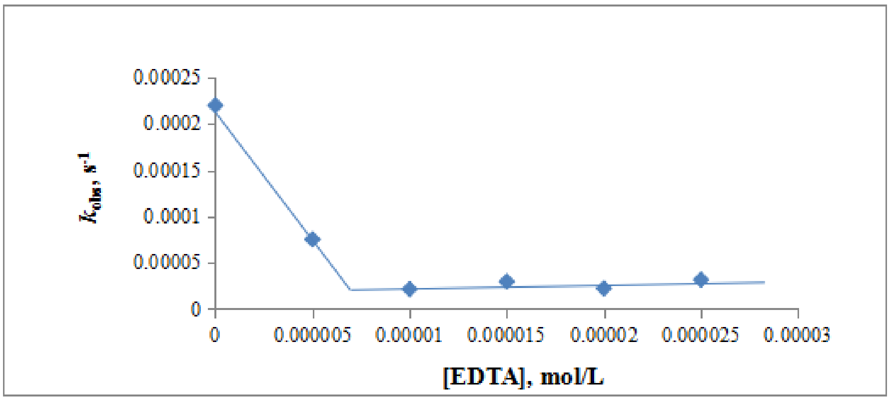

Figure 3. Effect of [EDTA] on k_{obs} of H_2S autoxidation at pH = 10.81-10.9, [S] = 2×10^{-3} mol L^{-1} and T = 30°C

DOI: https://doi.org/10.30564/jasr.v4i3.3465

studied by varying Na_2S (2×10^{-3} - 8×10^{-3} mol L^{-1}) in unbuffered medium. From eight [S]-dependence rate studies (Table 2) at three temperatures, 25, 30 and 35 °C, from log k_{obs} versus log[S] plots, the kinetics order was found to be 1.02 ± 0.13.

Table 2. The values of order in [S] determined from log k_{obs} versus log[S] plots

Temp., °C	25	25	30	30	30	30	30	35
Order in [S]	1.25	0.58	0.98	1.28	0.78	1.54	0.76	0.96
Average order in [S]	1.02 ± 0.13							

Thus, [S] and k_{obs} are related by Equation (4).

$$k_{obs} = k\,[S] \tag{4}$$

On combining Equations (3) and (4), we get Equation (5).

$$-d[O_2]/dt = k\,[S][O_2]_t \tag{5}$$

In accordance with Equation 5, the plot of k_{obs} versus [S] is linear (Figure 4).

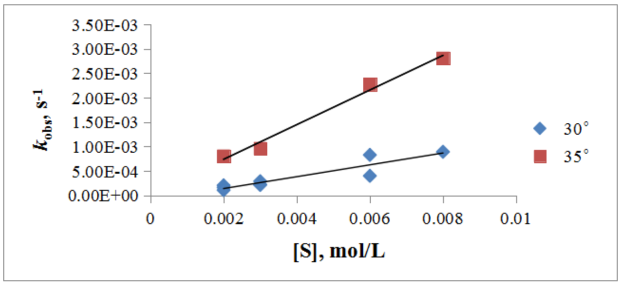

Figure 4. The plots of k_{obs} versus [S] at two different temperatures.

The values of k_{obs} at different [S] and $[O_2]$ are in Table 3. Since the kinetics has been performed in unbuffered medium, attempts were made to keep the same initial pH. However, despite our best efforts it was not possible to have exactly the same pH of the reaction mixtures, while varying [S] and $[O_2]$. Aside from trace metal ions catalysis, this is also one of the reasons for greater than normal uncertainty and scatter in k_{obs} values [59].

Table 3. The selected values of rate constants, k_{obs}, at different [S] and $[O_2]$

Temperature, °C	Initial pH	[S], mol L^{-1}	$[O_2]$, mg L^{-1}	k_{obs}, s^{-1}
25	10.77	2×10^{-3}	6.22	0.54×10^{-4}
	11.06	4×10^{-3}	6.31	1.39×10^{-4}
	11.23	6×10^{-3}	5.98	1.92×10^{-4}
	11.32	8×10^{-3}	6.25	3.32×10^{-4}
25	10.89	2×10^{-3}	5.5	3.66×10^{-4}
	11.17	3×10^{-3}	5.5	5.14×10^{-4}
	11.43	6×10^{-3}	5.5	7.41×10^{-4}
	11.58	8×10^{-3}	5.5	8.38×10^{-4}
30	10.86	2×10^{-3}	6	3.15×10^{-4}
	11.02	2×10^{-3}	6.2	2.33×10^{-4}
	11.17	3×10^{-3}	5.8	5.81×10^{-4}
	11.37	6×10^{-3}	5.1	2.25×10^{-3}
	11.57	8×10^{-3}	6	1.81×10^{-3}
30	10.81	2×10^{-3}	6.5	1.86×10^{-4}
	11.06	3×10^{-3}	6.3	2.25×10^{-4}
	11.32	6×10^{-3}	6.3	8.29×10^{-4}
	11.55	8×10^{-3}	6.7	8.93×10^{-4}
30	10.66	2×10^{-3}	5.72	1.08×10^{-4}
	10.85	4×10^{-3}	5.58	2.43×10^{-4}
	11.12	6×10^{-3}	5.72	3.12×10^{-4}
	11.21	8×10^{-3}	5.68	4.41×10^{-4}
30	10.68	2×10^{-3}	6.04	2.01×10^{-4}
	10.88	4×10^{-3}	6.05	2.96×10^{-4}
	11.16	6×10^{-3}	5.98	4.96×10^{-4}
	11.28	8×10^{-3}	5.61	5.58×10^{-4}
30	10.71	2×10^{-3}	5.58	1.92×10^{-4}
	10.91	4×10^{-3}	5.56	3.24×10^{-4}
	11.15	6×10^{-3}	5.45	3.99×10^{-4}
	11.26	8×10^{-3}	5.45	5.82×10^{-4}
35	10.77	2×10^{-3}	5.8	8.09×10^{-4}
	10.94	3×10^{-3}	5.9	9.64×10^{-4}
	11.3	6×10^{-3}	5.9	2.27×10^{-3}
	11.49	8×10^{-3}	5.8	2.81×10^{-3}

3.3 pH- Dependence

To study the effect of pH, the desired pH of water was adjusted with the help of dilute perchloric acid. In this process, the initial pH differed from the desired pH by about ± 0.02 units. To take into account this pH difference, each experiment was repeated three times and the k_{obs} values reported here are the average values of these replicate determinations. Since in each kinetics run, the pH changed with the progress of reaction, in the calculation of $[H^+]$ only the initial pH has been considered. k_{obs} values at different pH (Table 4) are seen to increase with increase in pH (Figure 5).

Since in this reaction, multiple hydrogen sulfide species are involved, $[H^+]$- dependence is an important parameter. The order of reaction with respect to $[H^+]$ was determined from the plot of log k_{obs} versus log $[H^+]$ and found to be -0.20. The small fractional negative order in $[H^+]$ indicates the effect of H^+ ion to be small. Indeed, a change in $[H^+]$ by an order of three resulted in a change in k_{obs} by an order of less than one.

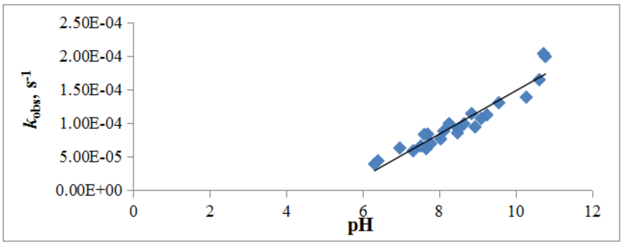

Figure 5. The plot of k_{obs} versus pH at [S] = 2×10^{-3} mol L^{-1} and T = 30°C

3.4 Effect of Ammonium Nitrate

Ammonium aerosols and ammonia gas are important trace atmospheric constituents and, therefore, the effect of ammonium nitrate was examined. The addition of ammonium nitrate had little effect on the reaction rate. This is contrary to findings of dissolved SO_2 oxidation in which both ammonia and ammonium ions strongly inhibited SO_2 oxidation [64].

3.5 Energy of Activation

By determining k_{obs} at three different temperatures and at [S] = 2×10^{-3} mol L^{-1}, the energy of activation, E_a, was determined to be 28.3 kcal mol^{-1}. Energy of activation is defined as the minimum amount of energy that must be provided to compounds to result in a chemical reaction. In previous studies using highly purified systems, E_a values have been reported to be 8 ± 0.4 kcal mol^{-1} [17] and 14.07 kcal mol^{-1} [19]. The significant difference in E_a values appears to be due the difference in reaction conditions employed.

3.6 Effect of Anthropogenic VOCs

Variety of volatile organic compounds such as aromatics, alcohols, terpenes, phenols, carbonyl compounds, carboxylic acids, esters, etc. are found as trace constituents in atmosphere. Sources of VOCs are both biogenic and anthropogenic. VOCs are involved

Table 4. The values of k_{obs} at different pH at [S] = 2×10^{-3} mol L^{-1} and T= 30°C

pH	$k_{obs}\{[H^+]^2+K_1[H^+]+K_1K_2\}$	k_{obs}, s^{-1}	$k_{obs}/[S] = k$ L mol^{-1}s^{-1}	$k\{[H^+]^2+K_1[H^+]+K_1K_2\}$
10.78	3.22×10^{-22}	2.00×10^{-4}	9.98×10^{-2}	1.61×10^{-19}
10.73	3.69×10^{-22}	2.04×10^{-4}	1.02×10^{-1}	1.84×10^{-19}
10.62	3.83×10^{-22}	1.65×10^{-4}	8.25×10^{-2}	1.92×10^{-19}
10.57	1.03×10^{-21}	3.94×10^{-4}	1.97×10^{-1}	5.13×10^{-19}
10.48	8.04×10^{-22}	2.51×10^{-4}	1.26×10^{-1}	4.02×10^{-19}
10.41	4.78×10^{-22}	1.27×10^{-4}	6.35×10^{-2}	2.39×10^{-19}
10.35	2.21×10^{-21}	5.12×10^{-4}	2.56×10^{-1}	1.11×10^{-18}
10.34	5.74×10^{-22}	1.30×10^{-4}	6.50×10^{-2}	2.87×10^{-19}
10.28	7.05×10^{-22}	1.39×10^{-4}	6.95×10^{-2}	3.52×10^{-19}
10.26	7.33×10^{-22}	1.38×10^{-4}	6.90×10^{-2}	3.66×10^{-19}
10.13	2.37×10^{-21}	3.31×10^{-4}	1.66×10^{-1}	1.18×10^{-18}
10.07	1.63×10^{-21}	1.98×10^{-4}	9.90×10^{-2}	8.14×10^{-19}
10.02	3.45×10^{-21}	3.74×10^{-4}	1.87×10^{-1}	1.73×10^{-18}
9.96	4.24×10^{-21}	4.00×10^{-4}	2.00×10^{-1}	2.12×10^{-18}
9.81	7.57×10^{-21}	5.06×10^{-4}	2.53×10^{-1}	3.78×10^{-18}
9.7	4.34×10^{-21}	2.25×10^{-4}	1.13×10^{-1}	2.17×10^{-18}
9.56	3.47×10^{-21}	1.31×10^{-4}	6.53×10^{-2}	1.74×10^{-18}
9.53	1.06×10^{-20}	3.72×10^{-4}	1.86×10^{-1}	5.31×10^{-18}
9.47	1.09×10^{-20}	3.32×10^{-4}	1.66×10^{-1}	5.44×10^{-18}
9.34	1.55×10^{-20}	3.50×10^{-4}	1.75×10^{-1}	7.74×10^{-18}
9.25	6.13×10^{-21}	1.12×10^{-4}	5.62×10^{-2}	3.06×10^{-18}
9.2	3.71×10^{-20}	6.06×10^{-4}	3.03×10^{-1}	1.85×10^{-17}
9.11	3.90×10^{-20}	5.17×10^{-4}	2.59×10^{-1}	1.95×10^{-17}
9.1	8.26×10^{-21}	1.07×10^{-4}	5.35×10^{-2}	4.13×10^{-18}
9.08	3.64×10^{-20}	4.51×10^{-4}	2.26×10^{-1}	1.82×10^{-17}
8.94	1.06×10^{-20}	9.44×10^{-5}	4.72×10^{-2}	5.28×10^{-18}
8.85	8.59×10^{-20}	6.22×10^{-4}	3.11×10^{-1}	4.29×10^{-17}
8.85	1.58×10^{-20}	1.14×10^{-4}	5.72×10^{-2}	7.90×10^{-18}
8.72	1.65×10^{-19}	8.84×10^{-4}	4.42×10^{-1}	8.27×10^{-17}
8.71	3.85×10^{-20}	2.01×10^{-4}	1.00×10^{-1}	1.92×10^{-17}
8.65	2.19×10^{-20}	9.90×10^{-5}	4.95×10^{-2}	1.09×10^{-17}
8.56	5.55×10^{-20}	2.04×10^{-4}	1.02×10^{-1}	2.78×10^{-17}
8.5	2.89×10^{-20}	9.17×10^{-5}	4.59×10^{-2}	1.44×10^{-17}
8.48	2.82×10^{-20}	8.56×10^{-5}	4.28×10^{-2}	1.41×10^{-17}
8.36	9.76×10^{-20}	2.22×10^{-4}	1.11×10^{-1}	4.88×10^{-17}
8.26	5.56×10^{-20}	9.94×10^{-5}	4.97×10^{-2}	2.78×10^{-17}
8.16	1.63×10^{-20}	2.28×10^{-5}	1.14×10^{-2}	8.16×10^{-18}
8.16	6.32×10^{-20}	8.86×10^{-5}	4.43×10^{-2}	3.16×10^{-17}
8.12	6.96×10^{-20}	8.83×10^{-5}	4.41×10^{-2}	3.48×10^{-17}
8.04	7.35×10^{-20}	7.64×10^{-5}	3.82×10^{-2}	3.67×10^{-17}
7.78	1.30×10^{-19}	6.95×10^{-5}	3.47×10^{-2}	6.51×10^{-17}
7.7	1.94×10^{-19}	8.37×10^{-5}	4.18×10^{-2}	9.71×10^{-17}
7.66	1.60×10^{-19}	6.18×10^{-5}	3.09×10^{-2}	7.99×10^{-17}
7.61	2.47×10^{-19}	8.32×10^{-5}	4.16×10^{-2}	1.23×10^{-16}
7.52	2.52×10^{-19}	6.60×10^{-5}	3.30×10^{-2}	1.26×10^{-16}
7.51	3.11×10^{-19}	7.91×10^{-5}	3.96×10^{-2}	1.55×10^{-16}
7.32	4.05×10^{-19}	5.87×10^{-5}	2.94×10^{-2}	2.03×10^{-16}
7.28	1.66×10^{-19}	2.13×10^{-4}	1.07×10^{-1}	8.32×10^{-16}
7.23	3.42×10^{-19}	3.75×10^{-5}	1.87×10^{-2}	1.71×10^{-16}
6.97	1.37×10^{-18}	6.29×10^{-5}	3.15×10^{-2}	6.86×10^{-16}
6.4	8.61×10^{-18}	4.38×10^{-5}	2.19×10^{-2}	4.31×10^{-15}
6.31	1.26×10^{-17}	3.92×10^{-5}	1.96×10^{-2}	6.28×10^{-15}
5.95	2.84×10^{-17}	2.08×10^{-5}	1.04×10^{-2}	1.42×10^{-14}

in many atmospheric reactions. Chen and Morris [16] examined the effect of some organics and found that, whereas EDTA, nitrilotriacetic acid (NTA), cyanide, peptone, citrate and glycerol inhibit metal catalyzed H_2S autoxidation, hydroquinone, formaldehyde and phenol accelerated the autoxidation [11,21,65].

Unlike the work of Chen and Morris [16], we examined the effect of anthropogenic VOCs on H_2S oxidation in unbuffered medium and in the absence of any added catalyst. Under these conditions, our results indicate anthropogenic VOCs such as acetanilide, benzene, ethanol, aniline, toluene, benzamide, *o*-xylene, *m*-xylene, *p*-xylene, anisole to have no significant effect on the reaction rate and any observed small effect is within the uncertainty of the rate measurements. The results are shown in Table 5.

Table 5. The selected values of first -order rate constants, k_{obs}, at 30°C

Compound	pH	[VOCs], mol L^{-1}	[S], mol L^{-1}	k_{obs}, s^{-1}
Acetanilide	10.73	0	2×10^{-3}	1.65×10^{-4}
	10.83	3×10^{-4}	2×10^{-3}	1.29×10^{-4}
	10.78	7×10^{-4}	2×10^{-3}	1.47×10^{-4}
Benzene	10.73	0	2×10^{-3}	1.36×10^{-4}
	10.78	2×10^{-4}	2×10^{-3}	1.16×10^{-4}
	10.81	3×10^{-4}	2×10^{-3}	1.26×10^{-4}
Toluene	10.8	0	2×10^{-3}	2.27×10^{-4}
	10.88	3×10^{-4}	2×10^{-3}	1.37×10^{-4}
	10.88	5×10^{-4}	2×10^{-3}	1.29×10^{-4}
	10.88	8×10^{-4}	2×10^{-3}	1.80×10^{-4}
Ethanol	10.78	0	2×10^{-3}	1.30×10^{-4}
	10.8	4×10^{-5}	2×10^{-3}	1.16×10^{-4}
	10.8	6×10^{-5}	2×10^{-3}	1.15×10^{-4}
Aniline	10.8	0	2×10^{-3}	1.02×10^{-4}
	10.8	3×10^{-4}	2×10^{-3}	1.45×10^{-4}
	10.81	6×10^{-4}	2×10^{-3}	1.41×10^{-4}
Anisole	10.72	0	2×10^{-3}	1.78×10^{-4}
	10.73	5×10^{-5}	2×10^{-3}	1.78×10^{-4}
	10.73	1×10^{-4}	2×10^{-3}	1.39×10^{-4}
o-xylene	10.75	0	2×10^{-3}	1.35×10^{-4}
	10.74	2×10^{-5}	2×10^{-3}	1.55×10^{-4}
	10.74	2×10^{-4}	2×10^{-3}	1.72×10^{-4}
m-xylene	10.74	0	2×10^{-3}	2.14×10^{-4}
	10.73	5×10^{-5}	2×10^{-3}	2.67×10^{-4}
	10.74	1×10^{-4}	2×10^{-3}	2.60×10^{-4}
p-xylene	10.75	0	2×10^{-3}	2.84×10^{-4}
	10.75	5×10^{-5}	2×10^{-3}	2.41×10^{-4}
	10.74	1×10^{-4}	2×10^{-3}	2.65×10^{-4}
Benzamide	10.75	0	2×10^{-3}	0.80×10^{-4}
	10.74	2×10^{-4}	2×10^{-3}	0.72×10^{-4}

4. Discussion

The equilibria (6-7) govern the dissociation of H_2S:

$$H_2S \xrightleftharpoons{K_1} HS^- + H^+ \qquad (6)$$

$$HS^- \xrightleftharpoons{K_2} S^{2-} + H^+ \qquad (7)$$

Where K_1 and K_2 are first and second dissociation constants of H_2S. The kinetics in this work was investigated in the pH range 6.3- 10.8 and $K_1 = 9.63\times10^{-8}$ and $K_2 = 1.34\times10^{-13}$ were used [66].

A speciation study showed that in aqueous media below pH 7, the dominant form shall be H_2S. On the other hand in the pH range 7-11, HS^- shall be dominant. Species S^{2-} would become important only beyond pH 11.5 [38,67]. This indicates that under our experimental conditions the major reactive species is expected to be HS^- [17]. Chen and Morris [16] have shown that HS^- is the dominant species in sulfide solutions everywhere from pH 7 to pH 12.5 and that it comprises better than 90% of the all sulfide species in aqueous solution from pH 8 to 11.5. Likewise, Millero [21] has shown that at pH 8.1 in aqueous solution $[H_2S]$ = 7.05 %, $[HS^-]$ = 92.95 % and $[S^{2-}] = 2.9\times10^{-5}$ %. Lewis [68] plotted the concentration of sulfide species against pH and showed HS^- to be dominant species between pH 7 -14.

The oxidation of the three principal species H_2S, HS^- and S^{2-} by oxygen is possible. These species are expected to be reactive but at relatively different rates of oxidation. Chen and Morris [16] reported that in acid solutions, pH< 6, where H_2S is the predominant sulfide species, the rate of oxidation is very low. When the pH was increased, the rate also increased, showing that HS^- is much more reactive than H_2S species. This work also showed the S^{2-} species to be less reactive than HS^- species [16]. The reaction has been studied by Avrahami and Golding [17] at very low S^{2-} concentrations in the pH range 11-13 and they explained the kinetics by assuming HS^- to be reactive. Likewise, Luther et al. [37] also assumed HS^- to be reactive species to explain their results in the pH 8-12. All these results indicate that in the oxidation of aquated hydrogen sulfide by O_2, the dominant and reactive species is HS^- in the pH range 7-11.

Now we turn our attention to results of pH dependence of this work. Since all the three species H_2S, HS^- and S^{2-} formed are governed by the equilibria (6) and (7), assuming all the three species to be reactive a following simplified general mechanism of hydrogen sulfide, [S(-II)], for its oxidation by O_2 may be written.

$$H_2S + O_2 \xrightarrow{k_0} \text{Products} \qquad (8)$$

$$HS^- + O_2 \xrightarrow{k_1} \text{Products} \qquad (9)$$

$$S^{2-} + O_2 \xrightarrow{k_2} \text{Products} \qquad (10)$$

Based on the mechanism (8-10), the general rate law (11) can be derived.

$$-d[O_2]/dt = k_0\,[H_2S][O_2] + k_1\,[HS^-][O_2] + k_2\,[S^{2-}][O_2] \qquad (11)$$

Equations (5-11) lead to the rate law (12):

$$\frac{-d[O_2]}{dt} = \frac{[S][O_2]_t(\,k_0[H^+]^2 + k_1K_1[H^+] + k_2K_1K_2)}{([H^+]^2 + K_1[H^+] + K_1K_2)} \qquad (12)$$

The rate law (12) predicts that the plot of k_{obs} versus $[H^+]$ should be non-linear, which was actually found to be true.

In this study, which was carried out in the pH range 6-10.5, the species present largely would be H_2S and HS^- with the latter being dominant. A detailed analysis of the $[H^+]$-dependence indicated only HS^- to be reactive. Hence, when only HS^- is considered to be reactive and dominant, the Equation (12) is modified to Equation (13).

$$\frac{-d[O_2]}{dt} = \frac{k_1K_1[H^+][S][O_2]_t}{(\,[H^+]^2 + K_1[H^+] + K_1K_2)} \qquad (13)$$

On comparing Equations (5) and (13), we get Equation (14), which rearranges to Equation (15).

$$k = \frac{k_1K_1[H^+]}{(\,[H^+]^2 + K_1[H^+] + K_1K_2)} \qquad (14)$$

$$k\,([H^+]^2 + K_1[H^+] + K_1K_2) = k_1K_1[H^+] \qquad (15)$$

As required by Equation (15), the plot between $k(\,[H^+]^2 + K_1[H^+] + K_1K_2)$ and $[H^+]$ was linear (Figure 6). Since $[H^+]$ dependence is important in deciding the reactive S(-II) species, more than seventy experiments were performed at 30°C and at different pH values keeping all other parameters constant. These k_{obs} values were used in drawing the plot between $k(\,[H^+]^2 + K_1[H^+] + K_1K_2)$ and $[H^+]$, which was a straight line passing through origin(Figure 6). The values of parameter, $k(\,[H^+]^2 + K_1[H^+] + K_1K_2)$, at different $[H^+]$ are collected in Table 4. According to Equation (15), the slope is equal to k_1K_1 (Figure 6), which on division by K_1 yielded the value of k_1. From the value of slope $(1.25 \pm 0.02) \times 10^{-8}$, using $K_1 = 9.63 \times 10^{-8}$ the value of k_1 was found to be 0.13 L $mol^{-1}s^{-1}$ at t = 30°C.

In the region of pH (7-11) generally used in this study, the reaction of O_2 with HS^- may occur through either a one-electron transfer reaction (16) or a two-electron transfer reaction(17).

$$O_{2(aq)} + HS^- \longrightarrow O_2^-{}_{(aq)} + HS^{\cdot} \qquad (16)$$

$$O_2 + H_2S \longrightarrow S^0 + H_2O_2 \qquad (17)$$

Thermodynamically, one-electron transfer and two-electron transfer reactions have been shown to be unfavorable and favorable, respectively and, therefore, the formation of superoxide ion, O_2^-, and bisulfide radical, $HS^{\cdot}$, has been considered unlikely [37]. It has been pointed out that sulfur (S^0) combines with sulfide ion to form polysulfide (S_x^{2-}) (x = 2-5) ions (18), but when pH > 7.5 sulfide has a higher holding capacity for sulfur [16]. Thus, the precipitation of sulfur becomes less likely: indeed, we found no precipitation of colloidal sulfur.

$$HS^- + (x\text{-}1)S \longrightarrow S_x^{2-} + H^+ \qquad (18)$$

Chen and Morris [16] suggested that the ultimate product of HS^- and O_2 is sulfate after passing through several intermediates.

For this autoxidation reaction, many diverse speculative mechanisms have been proposed [11,16,59,60,69]. These mechanisms fall in two distinct kinds of detailed oxidation mechanisms- polar and chain mechanisms. Polar mechanism suggested by Hoffmann and Lim [70] included the intermediates HSO_2^-, O_2^-, HSO_3^-, HO_2, H_2O_2, etc. The formation of sulfate comes from the oxidation of sulfite with oxygen. On the other hand a free radical mechanism involves metal ion as catalyst and several intermediates [60].

Before discussing the mechanism for sulfide - O_2 reaction, it is important to point out that this reaction is affected by traces of catalytic metals present in the reagent solutions even when no catalyst is added from outside. For this reason, the autoxidation reaction is characterized by poor reproducibility of reaction rate [59]. The involvement of trace

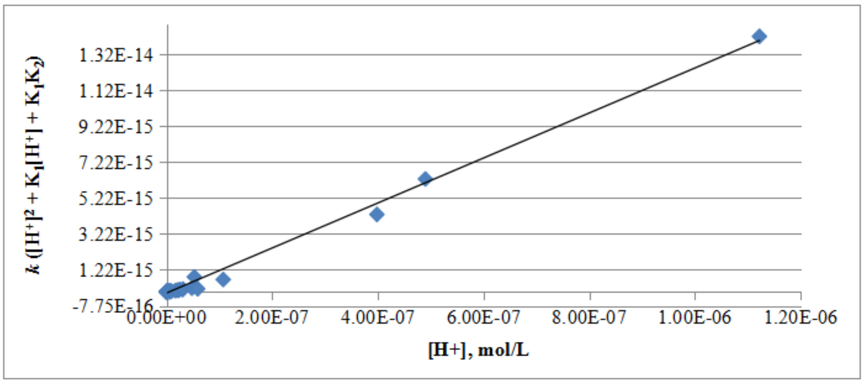

Figure 6. The plot of $k\{[H^+]^2 + K_1[H^+] + K_1K_2\}$ versus $[H^+]$ at $[S] = 2 \times 10^{-3}$ mol L^{-1} and T = 30°C

DOI: https://doi.org/10.30564/jasr.v4i3.3465

metal catalysts has been indicated by decrease in the rate of the reaction by EDTA and other chelating agents [11]. We too found strong inhibiting effect of EDTA (Figure 3). This indicates the involvement of trace metal ions as catalysts in any proposed mechanism. The catalytic role of metal ions in the mechanism can be explained as follows [21,65].

$$M^{2+} + O_2 + H^+ \longrightarrow M^{3+} + HO_2 \qquad (19)$$

$$M^{3+} + HS^- \longrightarrow M^{2+} + HS \qquad (20)$$

or

$$M(HS)^+ + O_2 \longrightarrow M^{2+} + S + HO_2^- \qquad (21)$$

$$HO_2^- + HS^- \longrightarrow 2OH^- + S \qquad (22)$$

The following features of the present study deserve a consideration in proposing any mechanism. One, the strong inhibition of the reaction rate by EDTA suggests the formation of a binary or a ternary complex involving trace metal ions M^{n+}, present as impurity, and ligands, O_2 and/or HS^- as in case of Co(II)-4,4',4'',4'''-tetrasulfophthalocyanine (Co(II)TSP) catalyzed HS^- autoxidation [59]. Two, the effect of VOCs such as benzene, toluene etc., which, are known to strongly inhibit sulfite autoxidation by scavenging intermediates free radicals, is not significant. It suggests that no such free radicals, which can we scavenged by these anthropogenic VOCs are formed and participate in the reaction.

In many proposed mechanisms intermediate O_2^- has been proposed [60,70]. A literature search revealed that the value of the rate constants for the reaction (23) to be 1.5×10^6 L mol^{-1}s^{-1} at pH 7.8 [71].

$$HO_2/O_2^- + S^{2-} \longrightarrow \text{Products} \qquad (23)$$

Although, the concentrations of species HO_2/O_2^- would be very small, and this combined with the low value of rate constants (23), their role is unlikely to be significant. However, there does exist a possibility of coordinated HO_2/O_2^- to be much more reactive than the uncoordinated ones, and then these may contribute significantly.

Our attempt failed to find the rate constants of radicals HO_2/O_2^- with any anthropogenic VOCs studied here and this rules out their inhibitory action as noted by us. This is in contrast to sulfite autoxidation in which the anthropogenic VOCs scavenge the sulfoxy radicals [40,41] and strongly inhibit the oxidation.

The oxidation of H_2S by O_2 appears to proceed via the formation of a tertiary activated complex in which O_2 and HS^- are reversibly bound to the metal complex [59] as in the mechanism (24-27).

$$M^{n+} + O_2 \xrightleftharpoons{K_3} [MO_2]^{n+} \text{ (rapid)} \qquad (24)$$

$$[MO_2]^{n+} + HS^- \xrightleftharpoons{K_4} [M(O_2)(HS)]^{(n-1)+} \text{ (rapid)} \qquad (25)$$

$$[M(O_2)(HS)]^{(n-1)+} \xrightarrow{k_4} M^{n+} + HSO_2^- \text{ (slow)} \qquad (26)$$

$$HSO_2^- + O_2 \longrightarrow HSO_4^- \text{ (fast)} \qquad (27)$$

This mechanism is not unique and can be written in several alternative forms. There is a good possibility of involvement of ternary $M^{n+}/M^{(n-1)+}$- O_2 - HS^- complexes and the catalytic role through transfer of electron via $M^{n+}/M^{(n-1)+}$ cycle in this mechanism. This is akin to catalysis of the autoxidation of S(IV) by Co(II)TSP, which was characterized in terms of an ordered ternary-complex mechanism in which both of S(IV) and oxygen were bound to the Co(II)/Co(III) metal center [72].

The complete rate law may be derived as follows. The rate of the reaction is given by Equation (28).

$$-d[O_2]/dt = k_4[M(O_2)(HS)]^{(n-1)+} \qquad (28)$$

From Equation (25), the concentration of the complex $[M(O_2)(HS)]^{(n-1)+}$ is given by Equation (29).

$$[M(O_2)(HS)]^{(n-1)+} = K_4[MO_2]^{n+}[HS^-] \qquad (29)$$

On substituting the value of $[M(O_2)(HS)]^{(n-1)+}$ in Equation (28), we get Equation (30).

$$-d[O_2]/dt = k_4K_4[MO_2]^{n+}[HS^-] \qquad (30)$$

From Equation (24), we have, the concentration of the complex $[MO_2]^{n+}$ as in Equation (31).

$$[MO_2]^{n+} = K_3[M^{n+}][O_2] \qquad (31)$$

From Equations (30) and (31), we get the rate law (32).

$$-d[O_2]/dt = k_4K_3K_4[M^{n+}][O_2][HS^-] \qquad (32)$$

Since $[HS^-]$ is part of complex $[M(O_2)(HS)]^{(n-1)+}$, the total [S] now would be given by Equation (33).

$$[S] = [H_2S] + [HS^-] + [S^{2-}] + [M(O_2)(HS)]^{(n-1)+} \qquad (33)$$

And the equilibrium concentration of HS^- is given by Equation (34).

$$[HS^-] = \frac{K_1[S][H^+]}{\{[H^+]^2 + K_1[H^+] + K_1K_2 + K_1K_3K_4[M^{n+}][O_2][H^+]\}} \qquad (34)$$

On combining Equations (32) and (34), we get the complete rate law (35).

$$-d[O_2]/dt = \frac{k_4K_1K_3K_4[M^{n+}][O_2][S][H^+]}{\{[H^+]^2 + K_1[H^+] + K_1K_2 + K_1K_3K_4[M^{n+}][O_2][H^+]\}} \qquad (35)$$

Since the reaction shows a first order dependence in each of $[O_2]$ and $[HS^-]$, it appears that the term ($K_1K_3K_4[M^{n+}]$ $[O_2]$ $[H^+]$) is much smaller than ($[H^+]^2 + K_1[H^+] + K_1K_2$). On ignoring the term $K_1K_3K_4[M^{n+}][O_2][H^+]$ in the denominator, the rate law (35) modifies to rate law (36).

$$-d[O_2]/dt = \frac{k_4K_1K_3K_4[M^{n+}][O_2][S][H^+]}{\{[H^+]^2 + K_1[H^+] + K_1K_2\}} \qquad (36)$$

The rate law (36) is same as experimental rate law (13) through $k_1K_1 = k_4K_1K_3K_4[M^{n+}]$.

4.1 Comparison with Previous Studies

There have been several kinetics studies on aquated H_2S autoxidation. In general, most of the studies including the present one support the operation of rate law (13):

$$\frac{-d[O_2]}{dt} = \frac{k_1K_1[H^+][S][O_2]_t}{([H^+]^2 + K_1[H^+] + K_1K_2)} \qquad (13)$$

with HS^- being the dominant and reactive H_2S species in the pH range(7-11).

It is interesting to compare the *k* values obtained in these studies (Table 6). The rate constants are under widely different conditions and are based on the different rate laws. Even then the rate constants are not much different (10^{-1}-10^{-2} L mol^{-1} s^{-1}), although the waters of different types were used. As in previous studies, EDTA [11] inhibited the reaction strongly indicating the involvement of catalytic role of trace metal ions. The effect of organics is small as indicated earlier [11,16,21]. Although, free radicals species have been involved by previous workers [60], our studies found no indication of their involvement. We also did not observe any induction period and formation of any colloidal sulfur.

Table 6. The collection of rate constants, *k*, values

Rate law	Rate constants, *k*	Conditions	Reference
$-d[S^{2-}]/dt_{t=0} = k[H_2S]^{1.34}[O_2]^{0.56}$	0.38×10^{-2}, $M^{-0.9}s^{-1}$	pH= 7.2, $O_2 = 8\times10^{-4}$ 25°C	[16]
	0.41×10^{-2}, $M^{-0.9}s^{-1}$	pH= 10.3, $O_2 = 3.2\times10^{-4}$	
$-d[H_2S]/dt = k_2[H_2S][O_2]$	0.19×10^{-2} L $mol^{-1}s^{-1}$	pH = 12, 25°C	[37]
$-d[H_2S]/dt = k_0[H_2S][O_2]$	$(0 \pm 2.78) \times 10^{-6}$ L $mol^{-1}s^{-1}$	pH = 6-8 , 25°C	[21]
$-d[H_2S]/dt = k_2[H_2S]_t[O_2]_t$	$(3.5\times10^{-6}$-$0.14\times10^{-3})$ s^{-1}	pH = 4.27-8.01, 28°C, O_2= 5-16.4 mgL^1, (Seawater)	[38]
$-d[O_2]/dt = k_1[HS^-][O_2]$	$k_1 = 1.3\times10^{-1}$ L mol^{-1} s^{-1}	Distilled water, pH = 6-11, 30°C	This work

4.2 Comparison with SO_2 Oxidation

The chemical behavior of acid rain precursors SO_2 and H_2S towards the oxidation by atmospheric oxygen is quite different although H_2S is believed to be a precursor of SO_2. There are some kinetics and mechanistic features, which differentiates their autoxidation.

(1) The kinetics of oxidation of aqueous S(IV) at constant pH is characterize by the rate law:

$-d[S(IV)]/dt = k[S(IV)]$

which is independent of $[O_2]$.

On the contrary, H_2S reaction at constant pH follows the rate law (5):

$-d[O_2]/dt = k[S][O_2]_t$

which is first order in O_2.

(2) EDTA inhibition of both reactions indicates a catalytic role for trace metal ions.

(3) A big difference in two studies is the effect of organic free radical scavengers. Whereas, S(IV) reaction is strongly inhibited due to scavenging of sulfate radical anion, SO_4^- [40,41], H_2S oxidation is not affected significantly. The latter observation does not require the invocation of free radicals in the present study.

4.3 Application to Atmospheric Chemistry

The results of this study indicate the oxidation of H_2S to be significant in atmospheric aqueous systems and its atmospheric aqueous phase conversion rates were calculated using Equation (37) [61].

Conversion rate (% day^{-1}) =

$$\left[\frac{\{100\,k[O_2][S]V\}}{\{(1000\,p_{H2S}/RT)+(\eta K_{H2S}\,p_{H2S}\,V)\}}\right]\times 150 day^{-1} \qquad (37)$$

where k = the second order rate constant in L mol^{-1} s^{-1},

p_{H2S} = the partial pressure of hydrogen sulfide in atm,

R= 0.082 L atm $mol^{-1}K^{-1}$,

$[O_2] = 2.6\times10^{-4}$ mol L^{-1} at 25°C [73] and 2.4×10^{-4} mol L^{-1} at 30°C [58]

$\eta = (1 + K_1/[H^+] + K_1K_2/[H^+]^2)$,

$V = 10^{-3}$ L water per m^3 of air,

[S] = the total concentration H_2S in solution = $\eta K_{H2S} p_{H2S}$,

K_{H2S} = the Henry's law constant in mol L^{-1} atm^{-1},

K_1 and K_2 are first and second dissociation constants of H_2S.

The K_{H2S} values are almost the same in the temperature range 25-30°C and, therefore, its value, 0.10132 mol L^{-1} atm^{-1}, was used in all calculations at different temperatures [74]. At the reported ambient p_{H2S} = 30 ppb [12], the conversion rate were calculated at pH = 6 -11.45 range and T = 25-30°C. The values (Table 7) show the conversion rates to be significant particularly when pH ≥ 8 as depicted in Figure 7. It leads to an interesting conclusion that those areas where the rainwater pH is high the aquatic oxidation of H_2S in atmospheric aqueous system would be significant and O_2 - oxidation pathway would be a significant contributor.

Our recent wet deposition studies found rainwater pH to be high in Western India [61,62] and, therefore, the results of this study would be important for such regions globally. On the other hand, for the regions of low rainwater pH < 8.5 such as North America this pathway would be insignificant [75].

DOI: https://doi.org/10.30564/jasr.v4i3.3465

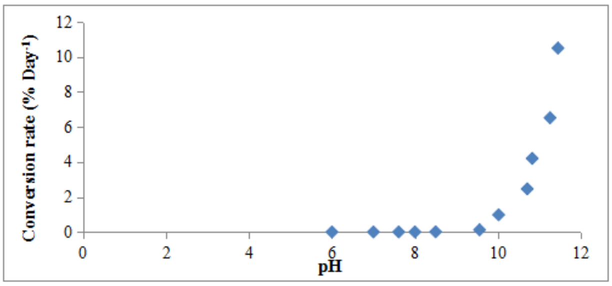

Figure 7. The plot of conversion rate of hydrogen sulfide versus pH at 25 and 30°C

Table 7. The conversion rates(% day^{-1}) of H_2S at 25 and 30°C

T, °C	pH	*k* (L mol^{-1} s^{-1})	η	% day^{-1}
25	11.45	7.31×10^{-2}	28167	10.50
25	10.83	11.8×10^{-2}	6570	4.20
30	11.26	7.25×10^{-2}	17952	6.52
30	10.71	9.60×10^{-2}	4974	2.46
30	10.02	1.87×10^{-1}	1011	0.98
30	9.56	6.53×10^{-2}	351	0.12
30	8.50	4.59×10^{-2}	31	7.5×10^{-3}
30	8.00	3.82×10^{-2}	10	2.1×10^{-3}
30	7.61	4.16×10^{-2}	5	1.0×10^{-3}
30	7.00	3.15×10^{-2}	1	1.5×10^{-4}
30	6.00	1.04×10^{-2}	0.1	5.2×10^{-6}

5. Conclusions

The major findings of this study are:

(1) The kinetics of oxidation of aqueous H_2S by O_2 obeys the rate law:

$$\frac{-d[O_2]}{dt} = \frac{k_1K_1[H^+][S][O_2]_t}{([H^+]_2 + K_1[H^+] + K_1K_2)}$$

This is in conformity the reactive hydrogen sulfide species in aqueous medium being hydrogen sulfide ion, HS^-.

(2) Our results indicate ammonium nitrate and anthropogenic VOCs such as acetanilide, benzene, ethanol, aniline, toluene, benzamide, *o*-xylene, *m*-xylene, *p*-xylene, anisole to have no significant effect.

(3) In this study, the involvement of trace metal catalysts is indicated by strong decrease in the rate of the reaction by EDTA, a strong chelating agent for metal ions.

(4) Both polar and non-polar mechanisms have been discussed.

(5) Calculation of atmospheric conversion rates shows these to increase with increase in pH and become sizable when pH is more than 6.

Acknowledgement

This project SB/S4/AS:143/2014 was funded by Science and Engineering Research Board, Department of Science and Technology, Ministry of Science and Technology, Govt. of India.

References

[1] World Health Organization. (2000). Hydrogen sulfide. In: Air quality guidelines, 2nd Edition, WHO regional office for Europe, Copenhagen, Denmark, pp 146-147.

[2] Crutzen, P. J., & Andreae, M. O. (1990). Biomass burning in the tropics: impact on atmospheric chemistry and biogeochemical cycles. Science, 250, 1669-1678. https://doi.org/10.1126/science.250.4988.1669.

[3] Gupta, K. S. (2012). Aqueous phase atmospheric oxidation of sulfur dioxide by oxygen: Role of trace atmospheric constituents – metals, volatile organic compounds and ammonia. Journal of Indian Chemical Society, 89, 713-724.

[4] Brandt, C., & van Eldik R. (1995). Transition metal catalyzed oxidation of aqueous sulfur(IV) oxides. Atmospheric -relevant process and mechanisms. Chemical Reviews, 95, 119-190. https://doi.org/10.1021/cr00033a006.

[5] Herrmann, H. (2003). Kinetics of aqueous phase reactions relevant to atmospheric chemistry. Chemical Reviews, 103, 4691-4716. https://doi.org/10.1021/cr020658q.

[6] OECD. (1985). Chapter 1, Air, In: The state of the environment, organization for economic cooperation and development, Paris, pp 17-46.

[7] Wayne, R. P. (2000). Chemistry of atmospheres, Oxford University Press, London, pp 27, 366.

[8] Dhayal, Y., Chandel, C. P. S., & Gupta, K. S. (2014). Role of some organic inhibitors on the oxidation of dissolved sulfur dioxide by oxygen in rain water medium. Environmental Science and Pollution Research, 21, 3474-3483. https://doi.org/10.1007/s11356-013-2253-1.

[9] Baird, C., & Cann, M. (2008). Environmental chemistry, W H Freeman, NewYork, pp 185-190.

[10] Bulfur, G., Boyle, A. J., & Baldinger, L. H. (1936). The decomposition of solutions of sodium sulfide. The Journal of the American Pharmaceutical Association, 25, 1104-1106. https://doi.org/10.1002/jps.3080251204.

[11] Weres, O., & Tsao, L. (1983). Reaction of hydrogen sulfide with oxygen in the presence of sulfite. Earth science division, Lawrence Berkeley laboratory, University of California, pp 4-30. https://escholarship.org/content/qt71j1g6p8/qt71j1g6p8.pdf.

[12] ATSDR. (2006). Toxicological guide for hydrogen sulfide. Atlanta, GA, US Department of health and human services, agency for toxic substances and dis-

DOI: https://doi.org/10.30564/jasr.v4i3.3465

ease registry.

[13] World Health Organization. (1981). Hydrogen sulfide, environmental health criteria, p. 19.

[14] Morse, J. W., Millero, F. J., Cornwell, J. C., & Rickard, D. (1987). The chemistry of the hydrogen sulfide and iron sulfide system in natural waters. Earth Science Reviews, 24, 1-42. https://doi.org/10.1016/0012-8252(87)90046-8.

[15] Abel, E. (1956). Autoxidation in the sulfur group. Monatshefte Fur Chemie, 87, 498-502.

[16] Chen, K. Y., & Morris, J. C. (1972). Kinetics of oxidation of aqueous sulfide by O_2. Environmental Science and Technology, 6, 529-537. https://doi.org/10.1021/es60065a008.

[17] Avrahami, M., & Golding, R. M. (1968). The oxidation of sulfide ion at very low concentrations in aqueous solutions. Journal of the Chemical Society A: Inorganic, Physical, Theoretical, 647-651. https://doi.org/10.1039/J19680000647.

[18] O'Brien, D. O., & Birkner, F. B. (1977). Kinetics of oxygenation of reduced sulfur species in aqueous – solution. Environmental Science and Technology, 11, 1114-1120. https://doi.org/10.1021/es60135a009.

[19] Alper, E., & Ozturk, S. (1985). Kinetics of oxidation of aqueous sodium sulfide solutions by gaseous oxygen in a stirred cell reactor. Chemical Engineering Communications, 36, 343-349. https://doi.org/10.1080/00986448508911264.

[20] Wilmot, P. D., Cadee, K., Katinic, J. J., & Kavanagh, B. V. (1988). Kinetics of sulfide oxidation by dissolved oxygen. Journal Water Pollution Control Federation, 60 1264-1270.

[21] Millero, F. J. (1986). The thermodynamics and kinetics of the hydrogen sulfide system in natural waters. Marine Chemistry, 18, 121-147. https://doi.org/10.1016/0304-4203(86)90003-4.

[22] Millero, F. J., Hubinger, S, Fernandez, M., & Garnett, S. (1987). Oxidation of H_2S in seawater as a function of temperature, pH and ionic strength. Environmental Science and Technology, 21, 439-443. https://doi.org/10.1021/es00159a003.

[23] Millero, F. J. (1991). The oxidation of H_2S with O_2 in the Black Sea. NATO ASI Series C: Mathematical and Physical Sciences. Black Sea Oceanography, 351, 205-227 https://link.springer.com/book/10.1007/978-94-011-2608-3.

[24] Millero, F. J. (1991). The oxidation of hydrogen sulfide in Farmvaren Fjord. Limnology and Oceanography, 36, 1007-1014. https://doi.org/10.4319/lo.1991.36.5.1007.

[25] Millero, F. J. (1991). The oxidation of hydrogen sulfide in the Chesapeake Bay. Estuarine, Coastal and Shelf Science, 33, 521-527. https://doi.org/10.1016/0272-7714(91)90088-S.

[26] Emerson, S., Cransto, R., & Liss, P. S. (1979). Redox species in a reducing fjord: equilibrium and kinetic considerations. Deep-Sea Research, Part A: Oceanographic Research Papers, 26, 859-878.

[27] Leonov, A. V., & Aizatullin, T. A. (1987). Kinetics and mechanism of hydrogen sulfide oxidation in sea water. Vodnye Resursy, 14, 89-103.

[28] Cline, J. D., & Richards, F. A. (1969). Oxygenation of hydrogen sulfide in seawater of constant salinity, temperature and pH. Environmental Science and Technology, 3, 838-843. https://doi.org/10.1021/es60032a004.

[29] Ostlund, G. H., & Alexander, J. (1963). Oxidation rate of sulfide in sea water preliminary study. Journal of Geophysical Research, 68, 3995-3997. https://doi.org/10.1029/JZ068i013p03995.

[30] Nielsen, A. H., Vollertsen, J., & Hvitved-Jacobsen, T. (2006). Kinetics and stoichiometry of aerobic sulfide oxidation in wastewater from sewers – effects of pH and temperature. Water Environment Research, 78, 275-283. https://doi.org/10.2175/106143005x94367.

[31] Sharma, K. R., & Yuan, Z. (2010). Kinetics of sulfide oxidation under high dissolved oxygen levels. Proceedings 6th International conference on sewer processes and networks, Gold coast, Australia.

[32] Kim, C., Zhou, Q., Deng, B., Thornton, E. C., & Xu, H. (2001) Chromium(VI) reduction by hydrogen sulfide in aqueous media: stoichiometry and kinetics. Environmental Science and Technology, 35, 2219-2225. https://doi.org/10.1021/es0017007.

[33] Sharma, V. K. (2010). Oxidation of inorganic compounds by ferrate(VI) and ferrate(V): one-electron and two-electron transfer steps. Environmental Science and Technology, 44, 5148-5152. https://doi.org/10.1021/es1005187.

[34] Cadena, F., & Peters, R. W. (1988). Evaluation of chemical oxidizers for hydrogen sulfide control. Journal Water Pollution Control Federation, 60, 1259-1263.

[35] Betterton, E. A., & Hoffmann, M. R. (1990). Kinetics and mechanism of the oxidation of aqueous hydrogen sulfide by peroxomonosulfate. Environmental Science and Technology, 24, 1819-1824. https://doi.org/10.1021/es00082a005.

[36] Tomar, M., & Abdulah, T. H. A. (1994). Evaluation of chemicals to control the generation of malodorous hydrogen sulfide in waste water. Water Research, 28, 2545-2552.

[37] Luther III, G. W., Findlay, A. J., Mcdonald, D. J., Owings, S. M., Hanson, T. E., Beinart, R. A., & Girguis, P. R. (2011). Thermodynamics and kinetics of sulfide oxidation by oxygen: a look at inorganically controlled reactions and biologically mediated processes in the environment. Frontiers in Microbial Physiology and Metabolism, 2, 1-9. https://doi.org/10.3389/fmicb.2011.00062.

[38] Siang, H. Y., Tahir, N. M., Malek, A., & Isa, M. Z. M. (2017). Breakdown of hydrogen sulfide in seawater under different ratio of dissolved oxygen / hydrogen sulfide. Malaysian Journal of Analytical Sciences, 21, 1016-1027. https://doi.org/10.17576/mjas-2017-2105-03.

[39] Nielsen, A. H., Vollertsen, J., & Hvitved-Jacobsen, T. (2004). Chemical sulfide oxidation of wastewater – effects of pH and temperature. Water Science and Technology, 50, 185-192. https://pubmed.ncbi.nlm.nih.gov/15484760.

[40] Meena, V. K., Dhayal, Y., Rathore, D. S., Chandel, C. P. S., & Gupta, K. S. (2017). Inhibition of aquated sulfur dioxide autoxidation by aliphatic, acyclic, aromatic, and heterocyclic volatile organic compounds. International Journal of Chemical Kinetics, 49, 221-233. https://doi.org/10.1002/kin.21069.

[41] Meena, V. K., Dhayal, Y., Rathore, D. S., Chandel, C. P. S., & Gupta, K. S. (2017). Inhibition of atmospheric aqueous phase autoxidation of sulphur dioxide by volatile organic compounds: mono-, di- and tri-substituted benzenes and benzoic acids. Progress in Reaction Kinetics and Mechanism, 42, 111-125. https://doi.org/10.3184%2F146867817X14806858832108.

[42] Meena, V. K., Dhayal, Y., Saxena, D., Rani, A., Chandel, C. P. S., & Gupta, K. S. (2016). The influence of diesel - truck exhaust particles on the kinetics of the atmospheric oxidation of dissolved sulfur dioxide by oxygen. Environmental Science and Pollution Research, 23, 17380-17392. https://doi.org/10.1007/s11356-016-6844-5.

[43] Grgic, I., Dovzan, A., Bercic, G., & Hudnik, V. (1998). The effects of atmospheric organic compounds on the Fe-catalyzed S(IV) autoxidation in aqueous solution. Journal of Atmospheric Chemistry, 29, 315-337. https://link.springer.com/article/10.1023/A:1005918912994.

[44] Grgic, I., Podkrajsek, B., Barzaghi, P., & Herrmann, H. (2007). Scavenging of SO_4^- radical anions by mono- and dicarboxylic acids in the Mn(II)-catalyzed S(IV) oxidation in aqueous solution. Atmospheric Environment, 41, 9187-9194. https://doi.org/10.1016/j.atmosenv.2007.07.051.

[45] Dhayal, Y., Chandel, C. P. S., & Gupta, K. S. (2014). The influence of hydroxyl volatile organic compounds on the oxidation of aqueous sulfur dioxide by oxygen. Environmental Science and Pollution Research, 21, 7805-7817. https://doi.org/10.1007/s11356-014-2661-x.

[46] Gupta, K. S., Mehta, R. K., Sharma, A. K., Mudgal, P. K., & Bansal, S. P. (2008). Kinetics of uninhibited and ethanol–inhibited CoO, Co_2O_3 and Ni_2O_3 catalyzed autoxidation of sulfur(IV) in alkaline medium. Transition Metal Chemistry, 33, 809-817. https://doi.org/10.1007/s10874-009-9123-8.

[47] Martin, L. R., Hill, M. W., Tai, A. F., & Good, T. W. (1991). The iron catalyzed oxidation of sulfur(IV) in aqueous solution: Differing effects of organics at high and low pH. Journal of Geophysical Resarch, 96, 3085-3097. https://doi.org/10.1029/90JD02611.

[48] Pasiuk- Bronikowska, W., Bronikowska, T., & Ulejczyk, M. (2003). Synergy in the autoxdation of S(IV) inhibited by phenolic compounds. Journal of Physical Chemistry A, 107, 1742-1748. https://doi.org/10.1021/jp0208790.

[49] Pasiuk- Bronikowska, W., Bronikowska, T., & Ulejczyk, M. (2003). Inhibition of the S(IV) autoxidation in the atmosphere by secondary terpeinic compounds. Journal of Atmospheric Chemistry, 44, 97-111. https://link.springer.com/article/10.1023/A:1022164702310.

[50] Podkrajsek, B., Grgic, I., Tursic, J., & Bercic, G. (2006). Influence of atmospheric carboxylic acids on catalytic oxidation of sulfur(IV). Journal of Atmospheric Chemistry, 54, 103-120. https://doi.org 10.1007/s10874-006-9018-x.

[51] Rudizinski, K. J. (2004). Degradation of isoprene in the presence of sulphoxy radical anions. Journal of Atmospheric Chemistry, 48, 191-216. https://doi.org/10.1023/B:JOCH.0000036851.98523.ef.

[52] Wang, L.-D., Yi, Z., Ma, Y.-L., & Ji-Ming, H. (2008). Intrinsic kinetics of sulfite oxidation with inhibitor of phenol. Acta Chimica Sinica, 66, 2336-2340.

[53] Wang, L.-D., Ma, Y.-L., Ji-Ming, H., & Yi, Z. (2009). Mechanism and kinetics of sulfite oxidation in the presence of ethanol. Industrial and Engineering Chemistry Research, 48, 4307-4311. https://doi.org/10.1021/ie801731h.

[54] Wolf, A., Deutsch, F., Hoffmann, P., & Ortner, H. M. (2000). The influence of oxalate on Fe-catalyzed S(IV) oxidation by oxygen in aqueous solution. Journal of Atmospheric Chemistry, 37, 125-135. https://doi.org/10.1023/A:1006462025384.

[55] Ziajka, J., Beer, F., & Warneck, P. (1994). Iron-cat-

alyzed oxidation of bisulfate aqueous solution: evidence for a free radical chain mechanism. Atmospheric Environment, 28, 2549-2552. https://doi.org/10.1016/1352-2310(94)90405-7.

[56] Ziajka, J., & Pasiuk-Bronikowska, W. (2005). Rate constants for atmospheric trace organics scavenging SO_4^- in the Fe-catalyzed autoxidation of S(IV). Atmospheric Environment, 39, 1431-1438. https://doi.org/10.1016/j.atmosenv.2004.11.024.

[57] Ziajka, P., & Pasiuk-Bronikowska, W. (2003). Autoxidation of sulfur dioxide in the presence of alcohols under conditions related to tropospheric aqueous phase. Atmospheric Environment, 37, 3913-3922. https://doi.org/10.1016/S1352-2310(03)00503-X.

[58] Mudgal, P. K., Bansal, S. P., & Gupta, K. S. (2007). Kinetics of atmospheric oxidation of nitrous acid by oxygen in aqueous medium. Atmospheric Environment, 41, 4097-4105. https://doi.org/10.1016/j.atmosenv.2007.01.036.

[59] Hoffmann, M. R. (1980). Trace metal catalysis in aquatic environments. Environmental Science and Technology, 14, 1061-1066. https://doi.org/10.1021/es60169a007.

[60] Zhang, J. Z., & Millero, F. J. (1993). Kinetics of oxidation of hydrogen sulfide in natural waters. In: Alpers, C.N., & Blowes, D.W. (Eds) Environmental Geochemisry of Sulfide Oxidation, Chapter 26, American Chemical Society, Washington, DC pp 393-409.

[61] Manoj, S. V., Mishra, C. D., Sharma, M., Rani, A., Jain, R., Bansal, S. P., & Gupta, K. S. (2000). Iron, manganese and copper concentrations in wet precipitations and kinetics of the oxidation of SO_2 in rain water at two urban sites, Jaipur and Kota, in western India. Atmospheric Environment, 34, 4479-4486. https://doi.org/10.1016/S1352-2310(00)00117-5.

[62] Misra, C. D., Khanooja, P. S., Sharma, A. K., Mudgal, P. K., Bansal, S. P., & Gupta, K. S. (2013). Studies on rainwater and dry depositions at Jaipur, India. Journal of Indian Chemical Society, 90, 1137-1146. https://www.researchgate.net/publication/287410793.

[63] Vazquez, G., Zhang, J., & Millaro, F. J. (1989). Effect of metals on the rate of the oxidation of H_2S in seawater. Geophysical Research Letters, 16, 1363-1366. https://doi.org/10.1029/GL016i012p01363.

[64] Mudgal, P. K., Sharma, A. K., Mishra, C. D., Bansal, S. P., & Gupta, K. S. (2008). Kinetics of ammonia and ammonium ion inhibition of the atmospheric oxidation of aqueous sulfur dioxide by oxygen. Journal of Atmospheric Chemistry, 61, 31-55. https://doi.org/10.1007/s10874-009-9123-8.

[65] Chen, K. Y., & Morris, J. C. (1972). Oxidation of sulfide by O_2: catalysis and inhibition. Journal of the Sanitary Engineering Division, 98, 215-227.

[66] Sun, W., Nesic, S., Young, D., & Woollam, R. C. (2008). Equilibrium expressions related to the solubility of the sour corrosion product mackinawite. Industrial and Engineering Chemistry Research, 47, 1738-1742. https://doi.org/10.1021/ie070750i.

[67] Harrup, M. K., & Hill, C. L. (1994). Polyoxometalate Catalysis of the Aerobic Oxidation of Hydrogen Sulfide to Sulfur. Inorganic Chemistry, 33, 5448-5455. https://doi.org/10.1021/ie070750i.

[68] Lewis, A. E. (2010). Review of metal sulphide precipitation. Hydrometallurgy, 104, 222-234. https://doi.org/10.1016/j.hydromet.2010.06.010.

[69] Steijns, M., Koopman, P., Nieuwenhuijse, B., & Mars, P. (1976). The mechanism of the catalytic oxidation of hydrogen sulfide III. An electron spin resonance study of the sulfur catalyzed oxidation of hydrogen sulfide. Journal of Catalysis, 42, 96-106. https://doi.org/10.1016/0021-9517(76)90095-6.

[70] Hoffmann, M. R., & Lim B. C. (1979). Kinetics and mechanism of the oxidation of sulfide by oxygen: catalysis by homogenous metal-phthalocyanine complexes. Environmental Science and Technology, 13, 1406-1414. https://doi.org/10.1021/es60159a014.

[71] Bielski, B. H. J., Cabelli, D. E., Arudi, R. L., & Ross A. B. (1985). Reactivity of HO_2/O_2^- radicals in aqueous solutions. Journal of Physical and Chemical Reference Data, 14, 1041-1100. https://doi.org/10.1063/1.555739.

[72] Hoffmann, M. R., & Hong, A. P. K. (1987). Catalytic oxidation of reduced sulfur compounds by homogeneous and heterogeneous Co(II) phthalocyanine complexes. Science of the Total Environment, 64, 99-115. https://doi.org/10.1016/0048-9697(87)90125-2.

[73] Patel, H., & Vashi, R. T. (2015). Characterization of textile wastewater. In: Characterization and treatment of textile wastewater. Butterworth Heinemann, Waltham, pp 21-71.

[74] Sander, R. (2015). Compilation of Henry's law constants (version 4.0) for water as solvent. Atmospheric Chemistry & Physics, 15, 4399-4981. https://doi.org/10.5194/acp-15-4399-2015.

[75] Jacob, D. J. (1999). Acid rain. In: Introduction to atmospheric chemistry. Princeton University Press, New Jersey, pp 247-255.

BILINGUAL PUBLISHING CO.
Pioneer of Global Academics Since 1984

Journal of Atmospheric Science Research
https://ojs.bilpublishing.com/index.php/jasr

EDITORIAL

An Exigency for Ice Core Studies to Determine Spatio-temporal Variability in Moisture Sources and Impact of Black Carbon – Mineral Aerosols on the Himalayan Glaciers

S. Nawaz Ali[1*]   Anil D. Shukla[2]

1. Birbal Sahni Institute of Palaeosciences, Lucknow, 226007, India
2. Physical Research Laboratory, Ahmedabad, 380009, India

ARTICLE INFO

Article history
Received: 13 August 2021
Accepted: 13 August 2021

Himalayan glaciers– the store house of fresh water outside the polar region contributes ~45% of the total river flow by glacial melt in the Indus, Ganga and Brahmaputra watersheds which supports the livelihood of ~500 million people [1]. The sustainability of these rivers is being questioned because of the growing evidences of accelerated glacier retreat in the recent decades, which is expected to have cascading effects on the mountainous areas and their surrounding lowlands. The rapid melting of Himalayan glaciers reveals their sensitivity to ongoing changes in climate dynamics, and if the current trend continues, rivers that rely heavily on snow/ice melt are expected to suffer hydrological disruptions to the point where some of the most populous areas may 'run out of water' during the dry season [2,3]. Therefore, efforts are being made to study the glacier mass balance trends in order to understand the patterns and causes of recent recessional trend. Despite their importance, the absence of long-term mass-balance and remote sensing data restricts our knowledge of the Himalayan glaciers' sensitivity/response to climate change. Furthermore, such studies may be insufficient unless are compared to long-term glacier fluctuations (millennial and multi-millennial time scales), which aid in better understanding the natural trends of and human impacts on climate change, as well as assessing the causes and possible future of contemporary shrinking glaciers. This will also improve our understanding of past glacier behaviour in the context of primary causes of glacier change, which is critical for water resource management and understanding climate variability in high alpine areas where alternative proxy climate archives are typically scarce. Therefore, it is pertinent to pool our scientific resources and energy (i) towards understanding the Himalayan glaciers' feeders (precipitation sources) and how they changed over time (geological and historical), as well as the causes of glaciers recession, one of which has been identified as (ii) black soot (carbon) in aerosol pollution.

**Corresponding Author:
S. Nawaz Ali,
Birbal Sahni Institute of Palaeosciences, Lucknow, 226007, India;
Email: snawazali@gmail.com*

DOI: https://doi.org/10.30564/jasr.v4i3.3556

Identifying the temporal changes in moisture sources: Glaciers in the Himalaya owe their existence to the precipitation brought by the two important weather systems viz. The Indian Summer Monsoon System (ISM) which forms a major component of the larger Asian Monsoon System and the mid-latitude westerlies. The ISM system is rooted in the larger atmospheric phenomenon with 1) the seasonal migration of seasonal migration of the Inter-tropical Convergence Zone (ITCZ), which is mainly governed by the seasonal variation of the latitude of maximum insolation [4,5], and 2) the seasonal reversal of winds, governed by the annual cycle of solar radiation interacting with different heat capacities of the Tropical Ocean and land areas (meridional pressure gradient) resulting in differential heating [6,7]. Whereas the maximum precipitation across the western Himalaya occurs in combination with westerlies, which are synoptic weather systems that propagate eastward from the Mediterranean region towards South Asia and are strengthened during periods of ice sheet expansion.

Being the most dominant weather system, the contemporary relationship between the ISM and the Himalayan snow cover has been the subject of extensive scientific research. In the recent years numerous studies investigated the relationship between ISM rainfall and snow cover over Himalaya. The results show that winter and spring snow cover over western Eurasia (eastern Eurasia) is negatively (positively) correlated to the subsequent summer monsoon [8]. Enhanced mid-latitude westerlies (westerly disturbances) that develop over the Mediterranean Sea/Black Sea/Caspian Sea as extratropical frontal systems, account for snow at the higher elevations of the NW and Central Himalaya in the winter [9]. In comparison, glaciers in the eastern Himalaya get the majority of their precipitation during the summer SW monsoon months, which also coincide with the melting season. As a result, the western and northwest glaciers are winter accumulation type, whereas their eastern counterparts are summer accumulation type. These inferences are drawn based on limited mass balance studies skewed towards summer months and scanty isotopic data obtained on snow and glacial melt. Thus, above these propositions are highly debatable and inconclusive.

Here it is worth mentioning that the Himalayan topography plays a significant role in modulating the relative influence of the ISM and westerly disturbances along and across the Himalaya. These weather systems define the magnitude and spatial extent of the glaciers in the Himalayan orogen [10-12]. The deep time inferences (millennial and multi-millennial time scales) regarding the contributory role of the ISM and westerlies in nourishing the Himalayan glaciers are largely drawn based on the chronologically constrained moraine stratigraphy and their correlation with the standard climatic curves. The study although provides a broad idea about temporal changes in moisture sources, however, because of strong chronometric dependency, the inferences about moisture sources would remain tentative and speculative. In view of this, the credible inferences about the spatial and temporal variability in the source of moisture towards the growth of Himalayan glacier should use the long (time) ice core data implying the isotopic fingerprinting of the ice core time slices.

The stable isotope ratios of oxygen (δO^{18}), hydrogen ($\delta^2 H$) and deuterium excess (d–excess) have been widely used for tracking the moisture sources and transport pathways of moisture laden air masses. The stable isotopic studies have also been used in quantifying the relative contributions of different moisture sources as well as reconstructing past climate variability [13,14]. Ice cores recovered from the northern slopes of Himalaya and Tibetan Plateau have provided some of the best high resolution records of past climate in the region. The stable isotope analyses of winter snow cover and summer rainfall along transect from the NW Himlayan (Ladakh) to the eastern Himalaya (Arunachal Pradesh) will help in establishing the spatial influence of the moisture sources. The relative contributions of the moisture source(s), their temporal variability and the corresponding growth/shrinkage (advance/retreat) of glaciers can only be addressed through long (time) ice core data implying the isotopic fingerprinting of the ice core time slices.

(ii) Impact of black soot (carbon) and mineral aerosol: Black soot in aerosol pollution can warm the troposphere, perhaps leading to surface melt [15,16]. Absorption is primarily caused by the black carbon (BC), whereas organic carbon (OC) absorbs mainly in the UV and slightly in the visible range. Black soot incorporated in snowflakes darkens snow and ice surfaces, increasing surface melt [17,18]. The extensive black soot aerosols might be lofted to the high Himalaya and incorporated in snowflakes, which when descending on the glaciers darken their surface. The presence of BC and OC in Himalayan snow and ice has inspired preliminary research on the subject, and its function in glacier melting has yet to be thoroughly assessed [19].

According to studies, soot may be the second most important component of global warming, after carbon dioxide, in terms of direct radiative forcing. Soot is anthropogenic in origin (combustion of biomass and fossil fuels); mineral aerosols, on the other hand, are naturally occurring continental dust from dryland areas carried by the winds. There are evidences to suggest that air-temperature trend over the Himalayan region has accelerated (between

0.15 and 0.3 K/decade) in recent decades. Unlike soot, the mineral aerosols are anticipated to have a negative forcing at the Earth's surface as they tend to scatter or absorb insolation and thus affect the radiation budget. Among aerosol constituents, black carbon (BC) is a key absorbing aerosol constituent formed by incomplete combustion of biomass, biofuel, and fossil fuel. The concentrations of aerosol are increasing over the Indian subcontinent and are expected to serious implications on the neighboring Himalayan glaciers through snow albedo reduction and accelerated melting of snow [20].

As such studies –till date- remain elusive from the Indian Himalaya, rational explanations for the complex and varying pattern of glacier response to climate variables across different sectors remain a source of contention. We are aware that there are logistical constraints as well as problems associated with ice core retrieval due to the less dense nature of Himalayan glacier ice, which prevents core recovery, but we must consider trying methodology so that some key glaciers located in climatically strategic locations can be drilled. Therefore, to begin with we must occupy the glaciers located in the climate sensitive transitional climatic zone in the Himalaya which are influenced by both the westerlies and the ISM.

References

[1] World Resources Institute – WRI Annual Report (2003). https://www.wri.org/wri-annual-report-2003.

[2] Bolch, T., Kulkarni, A., Kääb, A., Huggel, C., Paul, F., Cogley, J.G., Frey, H., Kargel, J.S., Fujita, K., Scheel, M. and Bajracharya, S., 2012. The state and fate of Himalayan glaciers. Science, 336(6079), pp.310-314.

[3] Maurer, J.M., Schaefer, J.M., Rupper, S. and Corley, A., 2019. Acceleration of ice loss across the Himalayas over the past 40 years. Science advances, 5(6), p.eaav7266.

[4] Riehl, H., 1979. Climate and weather in the tropics; Academic Press, San Diego.

[5] Gadgil, S., 2003. The Indian monsoon and its variability. Annual Review of Earth and Planetary Sciences, 31(1), pp.429-467.

[6] Webster, P.J., 1987, The elementary monsoon; In: Monsoons (eds) Fein, J.S. and Stephens, P.S., 3–32, (New York: Wiley).

[7] Tada, R., Zheng, H. and Clift, P.D., 2016. Evolution and variability of Asian monsoon and its potential linkage with the Himalayas-Tibetan Plateau uplift. Progress in Earth and Planetary Science, 3.

[8] Wu, Z., Li, J., Jiang, Z. and Ma, T., 2012. Modulation of the Tibetan Plateau snow cover on the ENSO teleconnections: From the East Asian summer monsoon perspective. Journal of Climate, 25(7), pp.2481-2489.

[9] Cannon, F., Carvalho, L.M., Jones, C. and Norris, J., 2016. Winter westerly disturbance dynamics and precipitation in the western Himalaya and Karakoram: a wave-tracking approach. Theoretical and Applied Climatology, 125(1), pp.27-44.

[10] Benn, D.I. and Owen, L.A., 1998. The role of the Indian summer monsoon and the mid-latitude westerlies in Himalayan glaciation: review and speculative discussion. Journal of the Geological Society, 155(2), pp.353-363.

[11] Ali, S.N. and Juyal, N., 2013. Chronology of late quaternary glaciations in Indian Himalaya: a critical review. Journal of the Geological Society of India, 82(6), pp.628-638.

[12] Sharma, S. and Shukla, A.D., 2018. Factors governing the pattern of glacier advances since the Last Glacial Maxima in the transitional climate zone of the Southern Zanskar Ranges, NW Himalaya. Quaternary Science Reviews, 201, pp.223-240.

[13] Jouzel, J., Froehlich, K. and Schotterer, U., 1997. Deuterium and oxygen-18 in present-day precipitation: data and modelling. Hydrological Sciences Journal, 42(5), pp.747-763.

[14] Ali, S.N., Sharma, A., Agrawal, S., MG, Y., RA, J., Dubey, J. and Morthekai, P., 2020. Oxygen and deuterium isotope characteri stics of Teesta river catchment from Sikkim Himalaya, India: Implications of different moisture sources. Geochemical Journal, 54(5), pp.327-336.

[15] Hansen, J., Sato, M., Ruedy, R., Lacis, A. and Oinas, V., 2000. Global warming in the twenty-first century: An alternative scenario. Proceedings of the National Academy of Sciences, 97(18), pp.9875-9880.

[16] Jacobson, M.Z., 2001. Strong radiative heating due to the mixing state of black carbon in atmospheric aerosols. Nature, 409(6821), pp.695-697.

[17] Warren, S.G. and Wiscombe, W.J., 1985. Dirty snow after nuclear war. Nature, 313(6002), pp.467-470.

[18] Clarke, A.D. and Noone, K.J., 2007. Soot in the Arctic snowpack: A cause for perturbations in radiative transfer. Atmospheric Environment, 41, pp.64-72.

[19] Xu, B., Cao, J., Hansen, J., Yao, T., Joswia, D.R., Wang, N., Wu, G., Wang, M., Zhao, H., Yang, W. and Liu, X., 2009. Black soot and the survival of Tibetan glaciers. Proceedings of the National Academy of Sciences, 106(52), pp.22114-22118.

[20] Das, S.K., Dobhal, D.P. and Juyal, N., 2010. Variability of aerosol optical depth and recent recessional trend in Dokriani Glacier, Bhagirathi Valley, Garhwal Himalaya. Current Science, pp.1816-1821.

DOI: https://doi.org/10.30564/jasr.v4i3.3556

Author Guidelines

This document provides some guidelines to authors for submission in order to work towards a seamless submission process. While complete adherence to the following guidelines is not enforced, authors should note that following through with the guidelines will be helpful in expediting the copyediting and proofreading processes, and allow for improved readability during the review process.

Ⅰ. Format

- Program: Microsoft Word (preferred)
- Font: Times New Roman
- Size: 12
- Style: Normal
- Paragraph: Justified
- Required Documents

Ⅱ. Cover Letter

All articles should include a cover letter as a separate document.

The cover letter should include:

- Names and affiliation of author(s)

The corresponding author should be identified.

Eg. Department, University, Province/City/State, Postal Code, Country

- A brief description of the novelty and importance of the findings detailed in the paper

Declaration

v Conflict of Interest

Examples of conflicts of interest include (but are not limited to):

- Research grants
- Honoria
- Employment or consultation
- Project sponsors
- Author’s position on advisory boards or board of directors/management relationships
- Multiple affiliation
- Other financial relationships/support
- Informed Consent

This section confirms that written consent was obtained from all participants prior to the study.

- Ethical Approval

Eg. The paper received the ethical approval of XXX Ethics Committee.

- Trial Registration

Eg. Name of Trial Registry: Trial Registration Number

- Contributorship

The role(s) that each author undertook should be reflected in this section. This section affirms that each credited author has had a significant contribution to the article.

1. Main Manuscript
2. Reference List
3. Supplementary Data/Information

Supplementary figures, small tables, text etc.

As supplementary data/information is not copyedited/proofread, kindly ensure that the section is free from errors, and is presented clearly.

Ⅲ. Abstract

A general introduction to the research topic of the paper should be provided, along with a brief summary of its main results and implications. Kindly ensure the abstract is self-contained and remains readable to a wider audience. The abstract should also be kept to a maximum of 200 words.

Authors should also include 5-8 keywords after the abstract, separated by a semi-colon, avoiding the words already used in the title of the article.

Abstract and keywords should be reflected as font size 14.

Ⅳ. Title

The title should not exceed 50 words. Authors are encouraged to keep their titles succinct and relevant.

Titles should be reflected as font size 26, and in bold type.

Ⅳ. Section Headings

Section headings, sub-headings, and sub-subheadings should be differentiated by font size.

Section Headings: Font size 22, bold type

Sub-Headings: Font size 16, bold type

Sub-Subheadings: Font size 14, bold type

Main Manuscript Outline

Ⅴ. Introduction

The introduction should highlight the significance of the research conducted, in particular, in relation to current state of research in the field. A clear research objective should be conveyed within a single sentence.

Ⅵ. Methodology/Methods

In this section, the methods used to obtain the results in the paper should be clearly elucidated. This allows readers to be able to replicate the study in the future. Authors should ensure that any references made to other research or experiments should be clearly cited.

Ⅶ. Results

In this section, the results of experiments conducted should be detailed. The results should not be discussed at length in this section. Alternatively, Results and Discussion can also be combined to a single section.

Ⅷ. Discussion

In this section, the results of the experiments conducted can be discussed in detail. Authors should discuss the direct and indirect implications of their findings, and also discuss if the results obtain reflect the current state of research in the field. Applications for the research should be discussed in this section. Suggestions for future research can also be discussed in this section.

Ⅸ. Conclusion

This section offers closure for the paper. An effective conclusion will need to sum up the principal findings of the papers, and its implications for further research.

Ⅹ. References

References should be included as a separate page from the main manuscript. For parts of the manuscript that have referenced a particular source, a superscript (ie. [x]) should be included next to the referenced text.
[x] refers to the allocated number of the source under the Reference List (eg. [1], [2], [3])
In the References section, the corresponding source should be referenced as:
[x] Author(s). Article Title [Publication Type]. Journal Name, Vol. No., Issue No.: Page numbers. (DOI number)

Ⅺ. Glossary of Publication Type

J = Journal/Magazine
M = Monograph/Book
C = (Article) Collection
D = Dissertation/Thesis
P = Patent
S = Standards
N = Newspapers
R = Reports
Kindly note that the order of appearance of the referenced source should follow its order of appearance in the main manuscript.
Graphs, Figures, Tables, and Equations
Graphs, figures and tables should be labelled closely below it and aligned to the center. Each data presentation type should be labelled as Graph, Figure, or Table, and its sequence should be in running order, separate from each other.
Equations should be aligned to the left, and numbered with in running order with its number in parenthesis (aligned right).

Ⅻ. Others

Conflicts of interest, acknowledgements, and publication ethics should also be declared in the final version of the manuscript. Instructions have been provided as its counterpart under Cover Letter.

Journal of Atmospheric Science Research

Aims and Scope

Journal of Atmospheric Science Research publishes original research papers that offers a rapid review and publication that freely disseminates research findings in areas of Remote Sensing, Weather Extremes, Air Pollution, Satellite Meteorology and more. The Journal focuses on innovations of research methods at all stages and is committed to providing theoretical and practical experience for all those who are involved in these fields.

Journal of Atmospheric Science Research aims to discover innovative methods, theories and studies in all aspects of Atmospheric Science by publishing original articles, case studies and comprehensive reviews.

The scope of the papers in this journal includes, but is not limited to:

- Remote Sensing
- Climate Dynamics
- Air Chemistry
- Hydrological Cycle
- Satellite Meteorology
- Ocean Dynamics
- Climate Change
- Weather Extremes
- Air Pollution
- Weather and Climate Prediction
- Climate Variability

Bilingual Publishing Co. (BPC)

Tel:+65 65881289

E-mail:contact@bilpublishing.com

Website:www.bilpublishing.com

About the Publisher

Bilingual Publishing Co. (BPC) is an international publisher of online, open access and scholarly peer-reviewed journals covering a wide range of academic disciplines including science, technology, medicine, engineering, education and social science. Reflecting the latest research from a broad sweep of subjects, our content is accessible world-wide——both in print and online.

BPC aims to provide an analytics as well as platform for information exchange and discussion that help organizations and professionals in advancing society for the betterment of mankind. BPC hopes to be indexed by well-known databases in order to expand its reach to the science community, and eventually grow to be a reputable publisher recognized by scholars and researchers around the world.

BPC adopts the Open Journal Systems, see on ojs.bilpublishing.com

Database Inclusion

Asia & Pacific Science
Citation Index

Creative Commons

China National Knowledge
Infrastructure

Google Scholar

Crossref

MyScienceWork

BILINGUAL
PUBLISHING CO.
Pioneer of Global Academics Since 1984

Tel:+65 65881289
E-mail: contact@bilpublishing.com
Website:ojs.bilpublishing.com

ISSN 2630-5119
03
9 772630 511218